EXECUTIVE SUMMARY OF THE THESIS

Analytical Model for Propagation of Debris Clouds in Geostationary orbit

LAUREA MAGISTRALE IN SPACE ENGINEERING - INGEGNERIA SPAZIALE

Author: SIMONE PIANI

Advisor: PROF. CAMILLA COLOMBO

Co-advisor: ANDREA MUCIACCIA

Academic year: 2020-2021

Nomenclature

Variable	Description	SI unit
a	Semi-major axis	km
a_{GEO}	Perfect synchronous orbit radius	km
A_c	Collision cross-section	km^2
E	Specific energy in $(\lambda, \dot\lambda)$ phase space	(rad/s)^2
E_p	Maximum potential energy of a pendulum	(rad/s)^2
$\hat{E}_0$	Specific total energy of a pendulum	(rad/s)^2
J_n	Zonal harmonic coefficient of n degree	-
$J_{n,m}$	Tesseral harmonic coefficient of n degree and m order	-
k	Square root of ratio $\hat{E}_0/E_p$	-
k_0^2	Ratio between initial potential energy and E_p	-
n	Fragment density	#s/rad^2
n_0	Initial fragment density	#s/rad^2
N_{frag}	Number of fragments	#
P_c	Collision probability	-
$R_\oplus$	Earth mean radius	km
r	Geocentric distance	km
$\hat{T}$	Time at risk	s
T_b	Band formation period	s
t	Time	s
t_0	Fragmentation instant	s
v_{rel}	Relative collision velocity	km/s
$\Delta\lambda$	Grid spacing in λ	rad
$\Delta\dot\lambda$	Grid spacing in $\dot\lambda$	rad/s
ϑ	Modified longitude: $2(\lambda - \lambda_{2,2} \pm \frac{\pi}{2})$	rad
κ	Inverse of k	-
λ	Longitude	rad
λ_0	Longitude of fragmentation event	rad
$\lambda_{1,2}$	Longitude of closest gravitational well	rad
$\lambda_{n,m}$	Gravitational coefficient of n degree and m order	rad
$\dot\lambda$	Drift longitude	rad/s
μ_f	Mean value of fragments' drift longitudes	rad/s
ρ	Spatial fragment density	#/km^3
σ_f	Variance of fragments' drift longitudes	rad/s
ϕ	Latitude	rad
Ω	Pendulum constant	rad/s
$\Omega_\oplus$	Earth rotational speed	rad/s

1. Introduction

From the beginning of the space age on 4 October 1957 to the beginning of 2020, more than 5500 rocket bodies have been launched to insert into orbits over 9300 payloads [3]. Nowadays, payloads have a fundamental role for our society: they guarantee weather forecasting, broadcasting, navigation, telecommunications, and many other services. However, the rising demand of on-orbit services together with the advent of large constellations is causing the overcrowding of Earth space region. As shown by ESA's annual space environment report [9], the U.S. Space Surveillance Network (SSN) has already tracked more than 16000 uncontrolled objects orbiting around Earth. Therefore, obtaining a reliable picture of the space debris environment and understanding its evolution is becoming a key element to analyse possible mitigation strategies and to suggest future policies to increase the sustainability of the space activities. In particular, this work studies the evolution of the debris environment inside the geostationary ring. The absence of atmospheric drag effects at GEO altitudes does not permit a natural decay of GEO objects and renders lifetimes of debris infinitely long.

2. Techniques for Debris Propagation

Current studies on space debris evolution in geosynchronous region adopt a deterministic approach and focus mainly on objects larger than 0.8-1.0 m [1]. This choice is essentially driven by a twofold reason. On the one hand, the lack of knowledge on fragmentation events causes a lack of situational awareness below 1 m. On the other hand, current computing capabilities limit number of objects that can be included inside the simulations. However, also debris smaller than 1 m represent a potential threat for operational satellites [5]. Thus, the inclusion of small fragments in debris modelling is fundamental to obtain a more complete picture of the debris environment and to avoid underestimating the collisional risk. To solve this problem, several authors have investigated analytical methods based on simplified dynamical models. For example, Letizia and Colombo [6] developed an analytical density-based model to describe debris evolution in LEO after fragmentation events.

In this work, an efficient method based on the continuum equation is developed to describe the evolution of fragment clouds generated by an explosion or a collision in space. The proposed approach consists in considering fragments population in the longitude and drift longitude phase space as a fluid with continuous properties, whose density changes under the effects of $J_{2,2}$ perturbation.

3. Dynamical Model

Geostationary region is a quite complex environment mainly affected by solar radiation pressure, luni-solar attraction and gravitational perturbations. However, to derive a long-term prediction of the longitudinal motion of large space debris clouds, a simplified dynamical model including only J_2 and $J_{2,2}$ effects is adopted. Hence, introducing the assumption of quasi-equatorial orbits and recalling that time evolution of λ is a low-frequency solution with negligible damping, the longitudinal motion of a GEO object can be described by the following equation [4]:

$$\ddot{\lambda} = 18\Omega_\oplus^2 J_{2,2} \frac{R_\oplus^2}{r^2} \sin 2\left(\lambda - \lambda_{2,2}\right) \qquad (1)$$

Moreover, assuming that objects of interest lie on quasi perfect geostationary orbits ($r \approx a_{GEO}$), the equation of motion becomes a simple non-linear pendulum like equation [4]

$$\ddot{\lambda} = 18\Omega_\oplus^2 J_{2,2} \frac{R_\oplus^2}{a_{GEO}^2} \sin 2\left(\lambda - \lambda_{2,2}\right) \qquad (2)$$

and allows the identification of the following equilibrium points:

Eq. points	Longitude	Stability
L1	75.071° E⋆	Stable
L2	104.929° W	Stable
L3	14.929° W	Unstable
L4	165.071° E	Unstable

⋆ E = East, W = West

Table 1: Equilibrium points.

By simply manipulating equation (2), the integral of motion can be derived to study GEO objects behaviour in $(\lambda,\dot{\lambda})$ phase space.

$$E = \dot{\lambda}^2 - 36\Omega_\oplus^2 J_{2,2} \left(\frac{R_\oplus}{a_{GEO}}\right)^2 \sin^2\left(\lambda - \lambda_{2,2}\right)$$

As shown in Figure 1, longitude evolution can be distinguished into circulating and librating regimes depending on the initial energy level of the object. If $E > 0$, GEO objects exhibit a drifting behaviour, moving between L3 and L4 equilibrium points. Conversely, objects with $E < 0$ are captured by one of gravitational wells, showing a circulating motion in $(\lambda,\dot{\lambda})$ phase space.
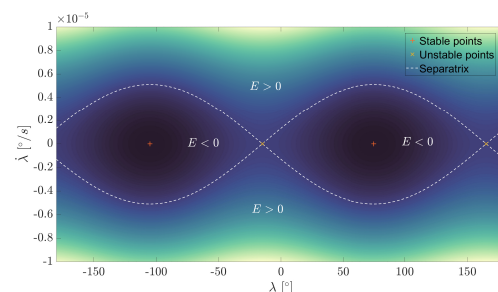

Figure 1: $(\lambda,\dot{\lambda})$ Phase space.

After analysing the dynamical behaviour in $(\lambda,\dot{\lambda})$ domain, an analytical solution for Equation (2) is researched by exploiting the analogy with a nonlinear swinging pendulum problem.

Substituting $\vartheta = 2(\lambda - \lambda_{2,2} \pm \frac{\pi}{2})$ and adopting Ochs' solution for a simple non linear pendulum [8], the analytical solution for the propagation of an object in GEO results to be:

$$\begin{cases} \theta(t) = \text{sgn}\left(\dot{\vartheta}_0\right) k\Omega\left[t - t_0\right] + \text{sn}^{-1}\left(k_0 \mid \kappa\right), \\ \lambda(t) = \arcsin(\text{sn}(\theta(t) \mid \kappa))\,\text{sgn}(\text{cn}(\theta(t) \mid \kappa)) \\ \qquad + \lambda_{1,2}, \\ \dot{\lambda}(t) = \frac{1}{2}\,\text{sgn}\left(\dot{\vartheta}_0\right)\sqrt{\hat{E}_0}\,\text{dn}(\theta(t) \mid \kappa). \end{cases}$$

with

$$\begin{cases} \Omega = 6\,\Omega_\oplus\sqrt{J_{2,2}}\,\dfrac{R_\oplus}{a_{GEO}}, \\ \hat{E}_0 = \dot{\vartheta}_0^2 + E_p\sin^2\left(\vartheta_0/2\right), \\ E_p = 4\Omega^2, \\ k = \sqrt{\hat{E}_0/E_p}, \\ \kappa = 1/k. \end{cases}$$

Analytical solution includes an *arcsin* function, which is able only to return values between $-\frac{\pi}{2}$ and $\frac{\pi}{2}$. Hence, a corrective algorithm has been developed to refer ϑ to the proper period and to correctly compute the time evolution of λ in case of drifting object.

Performing several tests, it is possible to highlight that analytical solution's accuracy tends to shrink by increasing the distance from the perfect synchronous orbit and by rising the eccentricity. Therefore, analytical method shall be used to provide, at most, a 2-year prediction of longitudinal evolution for objects orbiting in quasi-circular and quasi-equatorial orbits falling inside the GEO protected region ($|a - a_{GEO}| <$ 200 km) or a 1-year prediction for objects with $|a - a_{GEO}| <$ 500 km.

4. Cloud propagation

Once an analytical model for propagation of a single GEO object is derived, it is necessary to develop a strategy to obtain a reliable picture of GEO space debris environment evolution after a fragmentation event. In particular, the developed algorithm is essentially made by the following building blocks:

- a break up model that simulate collisions and explosions, given the energy of the fragmentation event;
- an analytical model to propagate fragments piece-wise until the cloud propagation becomes applicable;

- a method to convert orbital parameters of each single fragment into a continuous density function;
- a fully analytical cloud propagator to analyse time evolution of space debris cloud.

4.1. Break-up model

The breakup model allows to simulate fragmentation events (collisions or explosions) and to describe the distribution of the fragments in terms of characteristic length, area-to-mass ratio and velocity. The dispersion of these parameters depends on the nature of the event (collision or explosion), the energy involved in the fragmentation event and type of objects (rocket body or spacecraft). In this work, fragmentation particles are generated by adopting the NASA SBM [5]. Fragment features are derived from distribution functions and, therefore, vary at each run of the model even if initial conditions are unaltered. Different distributions are used to describe explosions and collisions. Indeed, collisions usually generate a large number of fragments with high relative velocities, while explosions produce larger fragments with lower speed. Moreover, in NASA breakup model, impactor kinetic energy per target mass is used to distinguish between catastrophic and non-catastrophic collisions. In particular, if the threshold value of $\tilde{E}_p^* = 40 J/g$ is exceeded, the model simulate the complete destruction of the target body [5].

4.2. Analytical piece-wise propagation

Analytical piece-wise propagation can be used to propagate individually the fragments until the cloud propagation becomes applicable and, also, to investigate the behaviour of a general fragment cloud in $(\lambda, \dot{\lambda})$ phase space. Indeed, once the fragments are generated with the NASA breakup model and their characteristics are defined, information on position and velocity of each fragment can be used to derive their orbital parameters. Then, the fragments can be mapped in $(\lambda, \dot{\lambda})$ phase space and evolution of the cloud can be investigated by using the analytical solution of a nonlinear pendulum. Following this procedure, three main phases can be distinguished during the evolution of a debris cloud. The first phase consists in the generation

of debris: fragments share the same longitudinal position but differ in velocity depending on the fragmentation energy distribution. In the second part, the initial dense ellipsoidal cloud is stretched due to the different orbital energy of the fragments; while, during the last phase, a fragment band is formed. In this analysis, the starting point for the band formation phase coincides with the time instant at which the hypothesis of uniform distribution in λ becomes acceptable. Therefore, band formation period is computed evaluating the time required to the faster fragment, in terms of longitudinal drift rate, to encounter the slowest one and introducing a a multiplication factor $k_b = 2$ [2]:

$$T_b = \frac{2\pi k_b}{\max\left(\dot{\lambda}_f\right) - \min\left(\dot{\lambda}_f\right)} \quad (3)$$

where $\dot{\lambda}_f$ are the longitudinal drifts of GEO object generated by the fragmentation event.

4.3.   Analytical Cloud Propagation

The continuity equation is used to derive analytically the density evolution with time under the effect of $J_{2,2}$ perturbation in $(\lambda, \dot{\lambda})$ phase space. Neglecting discontinuous events (all sink and source terms) and expanding the divergence in rectangular coordinates, continuity equation can be re-written as:

$$\frac{\partial n}{\partial t} + v_\lambda \frac{\partial n}{\partial \lambda} + v_{\dot{\lambda}} \frac{\partial n}{\partial \dot{\lambda}} = -n \left[\frac{\partial v_\lambda}{\partial \lambda} + \frac{\partial v_{\dot{\lambda}}}{\partial \dot{\lambda}} \right] \quad (4)$$

with

$$\begin{cases} v_\lambda = \dfrac{d\lambda}{dt} = \dot{\lambda}, \\ v_{\dot{\lambda}} = \dfrac{d\dot{\lambda}}{dt} = 18\Omega_\oplus^2 J_{2,2} \dfrac{R_\oplus^2}{a_{GEO}^2} \sin 2\left(\lambda - \lambda_{2,2}\right). \end{cases}$$

Then, the explicit expression of density evolution in time can be retrieved by applying the method of characteristics:

$$n\left(\lambda, \dot{\lambda}, t\right) = n_0 \left(\tilde{\lambda}, \tilde{\dot{\lambda}}, t_0\right) \quad (5)$$

where n_0 is the initial fragment distribution and $\tilde{\lambda}, \tilde{\dot{\lambda}}$ are obtained by inverting the characteristics at the initial time.

Following the approach proposed by Letizia [6], $\tilde{\lambda}$ and $\tilde{\dot{\lambda}}$ can be computed by solving the following system of equations:

$$\begin{cases} \tilde{\theta}(t) = \text{sgn}\left(\tilde{\dot{\lambda}}\right) \tilde{k}\Omega\left[t - t_0\right] + \\ \qquad + \text{sn}^{-1}\left(\sin(\tilde{\lambda} - \lambda_{1,2}) \mid \tilde{\kappa}\right), \\ 0 = \arcsin(\text{sn}(\tilde{\theta}(t) \mid \tilde{\kappa}))\,\text{sgn}(\text{cn}(\tilde{\theta}(t) \mid \tilde{\kappa})) \\ \qquad + \lambda_{1,2} - \lambda(t), \\ 0 = \dfrac{1}{2}\,\text{sgn}\left(\tilde{\dot{\lambda}}\right) \sqrt{\tilde{\hat{E}}}\text{dn}(\tilde{\theta}(t) \mid \tilde{\kappa}) - \dot{\lambda}(t). \end{cases}$$

It is clear that last system cannot be solved analytically and, thus, an alternative approach for the computation of $\tilde{\lambda}$ and $\tilde{\dot{\lambda}}$ must be found. In this work, it a backward propagation in time is performed by using the analytical solution previously derived. Hence, setting initial conditions $\lambda_0 = \lambda$ and $\dot{\lambda}_0 = \dot{\lambda}$ and propagation time $\Delta t = t_0 - t$, $\tilde{\lambda}$ and $\tilde{\dot{\lambda}}$ can be evaluated without the need of numerical or iterative methods.

$$\begin{cases} \theta(t) = \text{sgn}\left(\dot{\vartheta}_0\right) k\Omega\left[t - t_0\right] + \text{sn}^{-1}\left(k_0 \mid \kappa\right), \\ \tilde{\lambda}(t) = \arcsin(\text{sn}(\theta(t) \mid \kappa))\,\text{sgn}(\text{cn}(\theta(t) \mid \kappa)) \\ \qquad + \lambda_{1,2}, \\ \tilde{\dot{\lambda}}(t) = \dfrac{1}{2}\,\text{sgn}\left(\dot{\vartheta}_0\right) \sqrt{\hat{E}_0}\text{dn}(\theta(t) \mid \kappa). \end{cases}$$

Similarly to the procedure adopted before, a corrective algorithm must be implemented to evaluate correctly the output of *arcsin* function during backward propagation.

It is important to highlight that probabilistic propagation of initial density using method of characteristics allows to exactly evaluate fragment density only along the characteristic lines, meaning that density cannot be estimated outside the characteristics and that backward propagation should be employed for each point of interest. Thus, if density estimation is required over the entire domain, the phase space shall be discretised with a regular grid and density shall be evaluated at each grid corner. Therefore, this approach, as all discretisation methods, leads to an exponential grow of the number of samples with the rising of the domain dimensions. Moreover, reader shall notice that performance of cloud propagator is limited by the analytical solution used to invert the characteristic lines. To grant an accurate evaluation of $\tilde{\lambda}$ and $\tilde{\dot{\lambda}}$, only fragments with $|a - a_{GEO}| < 500km$ are included inside the simulation. Furthermore, orbits of debris are considered quasi-circular and quasi-equatorial.

4.4.   Position fitting

After the derivation of the analytical cloud propagator, information about the position of each single fragment in $(\lambda, \dot{\lambda})$ phase space must be translated into a continuous density function to derive initial conditions n_0 for the cloud propagation. Specifically, in this study, three different approaches are investigated: a binning method, an approach based on mono-dimensional probability distribution function and a bi-dimensional probability distribution function.

Both binning and 1-D PDF methods depend strongly on the sampling grid used to study the cloud evolution. Therefore, a third approach is implemented. This method consists in propagating individually fragments with the analytical propagator and, then, approximating fragment density at about a quarter of the band formation period $(t_0 + T_b/4)$ with a bi-dimensional standard probability distribution function. Therefore, a Kolmorov-Smirnov test is performed to identify the PDF that best reconstruct density distribution in λ and $\dot{\lambda}$.

After several simulations, Kolmogorov-Smirnov test suggests us that the multivariate normal distribution function is able to approximate quite precisely fragments distribution at $t_0+T_b/4$ both in terms of longitude and longitudinal drift. Despite the need of an initial piece-wise propagation, this approach results to be the most reliable and is used for the following simulations.

5.   Validation process

To validate the backward propagation and, thus, the analytical cloud propagator, a procedure based on the forward piece-wise propagation of the debris is implemented. After simulating a fragmentation and fitting the debris dispersion with a bi-variate normal distribution, a random sampling of the initial fragment density is performed by exploiting the build-in MAT-LAB function *mvnrnd*. This process generates initial conditions of thousands of fictitious debris, which are propagated individually forward in time to compute the density distribution. In the end, cloud propagation is validated by simulating several fragmentation events and performing a comparison between results provided by the cloud propagator and ones derived with the sampling process. As example, a catastrophic collision of a rocket body at $\lambda_0 = 60°$ with
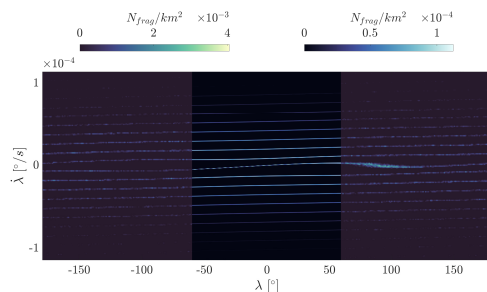
$\tilde{E}_p = 77.2 J/g$ is simulated and results obtained with the two aforementioned methods are plotted in Figure 2. Note that centre part of each plot illustrates density distribution retrieved applying the cloud propagator, while side parts present the results of the sampling approach.
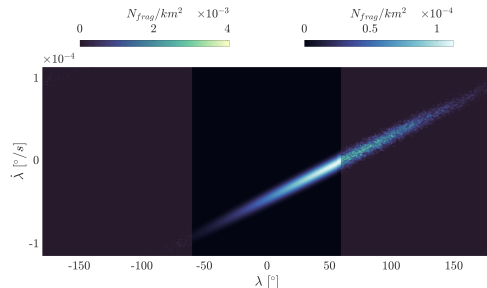
(a) Fragments distribution at $T_b/4$.
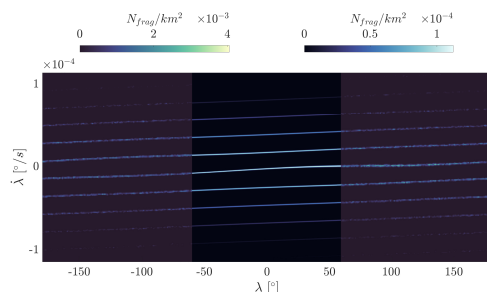
(b) Fragments distribution after 6 months.

(c) Fragments distribution after 1 year.

Figure 2: Comparison between cloud propagation and sampling strategy.

On the one hand, it is possible to observe that both approaches predict the same behaviour of the cloud and forecast peaks of density in correspondence of the same region of the phase space. On the other hand, absolute value of debris density differ significantly between methods. This fact is attributable to the number of sampled fictitious fragments and to the selection of the grid used for the binning method. Therefore, cloud propagation method results to be a fast and reliable tool for the prediction of debris density in geosynchronous region.

6. Collision probability

The main advantage of the analytical cloud propagation consists in providing a more direct connection with the statistical nature of the problem, in particular for what concerns the computation of the collision probability for a spacecraft crossing a debris cloud. Following McKnight's approach, the collision probability P_c for a target crossing a debris cloud can be computed applying the kinetic gas theory [7]:

$$P_c = 1 - e^{-\rho \cdot v_{rel} \cdot A_c \cdot \hat{T}} \qquad (6)$$

where ρ is the spatial density, v_{rel} the relative collision velocity, A_c the collision cross-section and $\hat{T}$ the time at risk.

6.1. Spatial density

Spatial density can be retrieved by simulating a fragmentation event and applying the analytical cloud propagation. Adopting this strategy, debris density can be computed only at discrete instants of time and, thus, selection of the time span used for the propagation will be crucial for the evaluation of the collision probability. Considering that fragments close to GEO protected region exhibit periods between 80 and 2000 days, it is recommended to adopt a time step of about 5 days to avoid undersampling debris density, misunderstanding fragment cloud evolution and underestimating collision probability.
To apply the kinetic theory of gases, the phase space density should be converted into a spatial one. Therefore, recalling that uncontrolled GEO objects tend naturally to arrange on orbits with inclination between $-15°$ and $15°$ [1], latitudinal dispersion of the debris can be approximated as a uniform distribution:

$$p(\phi) = \begin{cases} \frac{6}{\pi} & \text{for } |\phi| \leq 15° \\ 0 & \text{for } |\phi| > 15° \end{cases} \qquad (7)$$

and spatial density can be computed as:

$$\rho = \frac{9\Omega_\oplus}{\pi a_c^3} n(\lambda, \dot{\lambda}, t) \qquad (8)$$

6.2. Relative collision velocity

The average relative velocity is considered as function of orbital velocity of the operating GEO satellite and the mutual inclination between the debris and target mass. In this study, operational satellite at risk is assumed on a perfect geostationary orbit and, thus, mutual inclination is replaced by the average inclination of the derelict population. As suggested by McKnight [7], an average inclination of $10°$ is assumed to avoid underestimating the collision probability, resulting in a relative velocity of about 536 m/s.

6.3. Collision cross-section and time at risk

In this work, collision cross-section is considered as function of impacting and target physical cross-sections and is set equal to $100\,m^2$ [7]. Moreover, to assess the annual probability of collision, the time at risk for a station-kept satellite is set equal to one year.

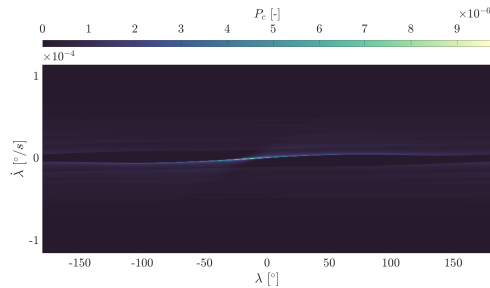## 6.4. Collision probability calculation

Several tests are performed to check the consistency between the obtained collision risk and the dynamics governing the geosynchronous region. Figure 3a and Figure 3b show that a fragmentation close to one of the gravitational wells produces a peak in collision probability in proximity of the closest stable equilibrium point. This behaviour can be justified by the fact that a large part of the debris is characterized by $E < 0$ and exhibits a librating motion around the closest gravitational well. Conversely, Figure 3c, illustrates that a fragmentation at L3 generates only drifting objects and, thus, that librating region of the phase space has a null collision risk.
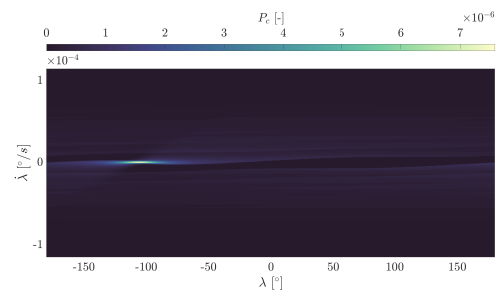
(a) Fragmentation at $\lambda_0 = -110°$.
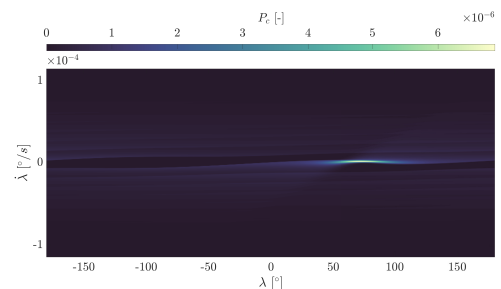
(b) Fragmentation at $\lambda_0 = 60°$.

(c) Fragmentation at $\lambda_0 = -15°$.

Figure 3: Collision probability in $(\lambda, \dot{\lambda})$ phase space.

7. Conclusions

This work proposes a probabilistic approach based on the continuity equation, enabling the inclusion of small fragments in the debris modeling for the GEO region. In particular, the developed method considers debris population as a fluid with continuous properties, whose density changes under the effect of $J_{2,2}$ gravitational perturbation. Once the information on the position of the fragments is converted into a continuous density function, time evolution of debris density close to the GEO protected region is obtained by solving analytically the continuity equation with the assumption of quasi-equatorial and quasi-circular orbits. The explicit expression for the density allows the method to provide a very fast estimation of longitude slots most susceptible to rising debris fluxes and to evaluate the resulting collision probability for an operative spacecraft in that region. The proposed method has been extensively validated through a comparison with a numerical/analytical piece-wise propagator. The current version of the method includes only the $J_{2,2}$ effect limiting its applicability to objects orbiting on quasi-circular and quasi-equatorial orbits with $|a - a_{GEO}| < 500$km. Future works will further develop the proposed method. The present results suggest that the proposed method can be applied to efficiently analyse the impact of different breakups on various target spacecrafts and, thus, to create influence matrices. Moreover, the developed approach results to be a fast and precise tool for the generation of collision probability maps that could be exploited for the definition of a space debris index for the geostationary region.

References

[1] P. V. Anderson and Hanspeter Schaub. *Characterising Longitude-Dependent Orbital Debris Congestion in the Geosynchronous Orbit Regime.* PhD thesis, University of Colorado at Boulder, January 2015.

[2] Joshua Ashenberg. Formulas for the phase characteristics in the problem of low-earth-orbital debris. *Journal of Spacecraft and Rockets*, 31(6):1044–1049, 1994.

[3] S. Frey. *Evolution and hazard analysis of orbital fragmentation continua.* PhD thesis, Politecnico di Milano, http://hdl.handle.net/10589/165144, July 2020.

[4] R.H. Frick and T.B. Garber. Perturbations of a synchronous satellite due to triaxiality of the earth. *Journal of the Aerospace Sciences*, 29(9):1105–1111, 1962.

[5] H. Klinkrad. *Space Debris: Models and Risk Analysis.* Springer Praxis Books. Springer Berlin Heidelberg, 2006.

[6] F. Letizia and C. Colombo. *Space debris cloud evolution in Low Earth Orbit.* PhD thesis, University of Southampton, http://eprints.soton.ac.uk/id/eprint/387121, November 2015.

[7] Darren S. McKnight and Frank R. Di Pentino. New insights on the orbital debris collision hazard at geo. *Acta Astronautica*, 85:73–82, 2013.

[8] Karlheinz Ochs. A comprehensive analytical solution of the nonlinear pendulum. *European Journal of Physics*, 32(2):479–490, feb 2011.

[9] ESA Space Debris Office, editor. *ESA'S ANNUAL SPACE ENVIRONMENT REPORT.* European Space Agency, 2021.

POLITECNICO
MILANO 1863

Analytical Model for Propagation of Debris Clouds in Geostationary orbit

TESI DI LAUREA MAGISTRALE IN
SPACE ENGINEERING - INGEGNERIA SPAZIALE

Author: **Simone Piani**

Student ID: 944583
Advisor: Prof. Camilla Colombo
Co-advisors: Andrea Muciaccia
Academic Year: 2020-21

Abstract

Geostationary ring is an important resource for terrestrial satellite industry that is threatened by a rising number of space debris. As absence of atmospheric drag effects at Geosynchronous Earth Orbits (GEO) altitudes does not allow a natural decay of Geostationary objects and makes lifetimes of debris infinitely long, upper launch vehicle stages together with decommissioned satellites and fragmentation particles represent a growing hazard for operating satellites. Therefore, on the one hand, continuous conjunction assessments and collision avoidance manoeuvres are performed to safeguard functional GEO satellites. But, on the other hand, obtaining a reliable picture of the evolution of space debris environment is a key element to identify the longitude slots most susceptible to rising debris fluxes, to analyse possible mitigation strategies and to suggest future policies to increase the sustainability of the space sector.

Therefore, in this work, an analytical approach is developed to describe the evolution of space debris clouds generated by fragmentations in GEO. In contrast to traditional approaches, which imply the propagation of individual fragments, the proposed method allows considering debris population as a fluid with continuous properties and to study globally the cloud evolution, significantly reducing the computational effort. A standard breakup model is adopted to simulate fragmentation events and to describe the dispersion of the fragments in terms of characteristic length, area-to-mass ratio and velocity. Velocity distribution is used to derive the initial conditions of the cloud density and fragment cloud evolution is derived solving the continuity equation, which describes the variation of debris density under $J_{2,2}$ effect. The proposed approach is completely analytical and enables to study the collision risk simulating several breakup events and to evaluate the vulnerability of different operational satellites with a very limited computational cost. This approach lays the foundations for the definition of a space debris index for the geostationary region.

This thesis is part of the COMPASS project: "Control for orbit manoeuvring by surfing through orbit perturbations" (Grant agreement No 679086). This project is European Research Council (ERC) funded project under the European Union's Horizon 2020 research (www.compass.polimi.it).

Sommario in lingua italiana

Le orbite geostazionarie sono un'importante risorsa per l'industria spaziale, tuttavia, questa regione orbitale è minacciata da un crescente numero di detriti. L'assenza di atmosfera in questa regione, infatti, non permette il decadimento naturale di questi e rende la loro vita infinitamente lunga. Per questo motivo, gli stadi alti dei lanciatori, i satelliti inattivi e i frammenti generati da collisioni o esplosioni rappresentano un potenziale pericolo per i satelliti operativi. Dunque, da una parte, continue manovre devono essere effettuate per salvaguardare i satelliti operativi; dall'altra, analisi sull'evoluzione dei detriti sono richieste per identificare le longitudini con rischio di collisioni più elevato, per selezionare potenziali candidati per missioni dedicate alla rimozione attiva di detriti e, infine, per definire l'affidabilità richiesta per le manovre di disposal.

In questa tesi, dunque, viene sviluppato un approccio analitico per descrivere l'evoluzione di intere nuvole di detriti generate da frammentazioni (esplosioni o collisioni). Al contrario degli approcci tradizionali, che propagano i frammenti individualmente, il metodo proposto permette di studiare l'evoluzione globale della nuvola riducendo in modo significativo il costo computazionale e rimuovendo la dipendenza tra il tempo richiesto dalla simulazione e il numero di frammenti generati. Il NASA Breakup Model viene utilizzato per simulare la frammentazione e descrivere la distribuzione dei detriti in termini di dimensione caratteristica, area, massa e velocità. Le velocità vengono quindi utilizzate per derivare le condizioni iniziali della nuvola e la sua evoluzione viene investigata risolvendo l'equazione del continuo, la quale permette di descrivere la variazione della densità sotto l'influenza di $J_{2,2}$. L'approccio proposto è completamente analitico, permette di studiare la probabilità di collisione e di valutare la vulnerabilità di differenti satelliti con un limitato costo computazionale. Questo metodo getta dunque le fondamenta per la definizione di un indice (space debris index) per la regione geostazionaria.

Keywords: detriti spaziali, frammentazione, $J_{2,2}$, propagazione analitica, probabilità di collisione.

Contents

List of Figures

List of Tables

List of Symbols

Variable	Description	SI unit
a	Semi-major axis	km
a_{GEO}	Perfect synchronous orbit radius	km
A_c	Collision cross-section	km^2
A_p	Projectile cross-section	km^2
A_t	Target cross-section	km^2
$C_{n,m}$	Gravitational coefficient of n degree and m order	-
E	Specific energy in $(\lambda, \dot{\lambda})$ phase space	(rad/s)^2
E_p	Maximum potential energy of a pendulum	(rad/s)^2
$\tilde{E}_p$	Specific impact energy	J/g
$\tilde{E}_p^*$	Catastrophic specific impact energy	J/g
$\hat{E}_0$	Specific total energy of a pendulum	(rad/s)^2
J_n	Zonal harmonic coefficient of n degree	-
$J_{n,m}$	Tesseral harmonic coefficient of n degree and m order	-
k	Square root of ratio $\hat{E}_0/E_p$	-
k_0^2	Ratio between initial potential energy and E_p	-
L_c	Fragment characteristic length	m
M_c	Fragmentation mass	kg
n	Fragment density	#s/rad^2
$\hat{n}$	Fragment density	#/km^2
N_{frag}	Number of fragments	#
$P_{n,m}[x]$	Associated Legendre Function of n degree and m order	-
P_c	Collision probability	-
$R_\oplus$	Earth mean radius	km
r	Geocentric distance	km

Variable	Description	SI unit
$S_{n,m}$	Gravitational coefficient of n degree and m order	-
T	Drifting/Librating period	s
$\hat{T}$	Time at risk	s
T_b	Band formation period	s
t	Time	s
t_0	Fragmentation instant	s
U	Gravitational potential	MJ
$V_{\lambda,\dot{\lambda}}$	Fragments covariance between λ and $\dot{\lambda}$	-
v_{GEO}	Velocity on perfect synchronous orbit	km/s
v_{rel}	Relative collision velocity	km/s
α_G	Right Ascension of Greenwich meridian	rad
Δa	Difference between a and a_{GEO}	km
Δa_{spx}	Expression separatrix in $(\lambda, \Delta a)$ phase space	km
Δi	Mutual inclination between projectile and target orbits	rad
$\Delta \lambda$	Grid spacing in λ	rad
$\Delta \dot{\lambda}$	Grid spacing in $\dot{\lambda}$	rad/s
θ	Longitude relative to vernal equinox	rad
ϑ	Modified longitude	rad
$\varkappa$	Inverse of k	-
λ	Longitude	rad
λ_0	Longitude of fragmentation event	rad
$\lambda_{1,2}$	Longitude of closest gravitational well	rad
$\lambda_{n,m}$	Gravitational coefficient of n degree and m order	rad
$\dot{\lambda}$	Drift longitude	rad/s
$\dot{\lambda}_{spx}$	Expression separatrix in $(\lambda, \dot{\lambda})$ phase space	rad/s
μ	Earth gravitational parameter	km³/s²
μ_i	Mean value of quantity i	-
ρ	Spatial fragment density	#/km³
σ_i	Variance of quantity i	-
ϕ	Latitude	rad
Ω	Pendulum constant	rad/s
$\Omega_\oplus$	Earth rotational speed	rad/s

List of Acronyms

Acronym	Description
ECI	Earth Centered Inertial frame
ECEF	Earth-Centered Earth-Fixed frame
ESA	European Space Agency
GEO	Geosynchronous Earth Orbit
KS	Kolmogorov-Smirnov Statistic
LEO	Low Earth Orbit
ODE	Ordinary Differential Equation
PDE	Partial Differential Equation
PDF	Probability Distribution Function
SBM	Standard Breakup Model
SRP	Solar Radiation Pressure

Acknowledgements

First and foremost, I would like to express my gratitude to my parents, Patrizia and Gianluca, for the continuous and immense motivation. Your support and encouragement have granted me the opportunity to boldly pursue my dreams, one of which is achieving the master's degree in Space Engineering. I write with the knowledge that I would not be where I am so joyfully today without your selfless investments in me. I would also like to acknowledge my brother Marco and my friends that supported me during all the difficult moments faced in the last years. Moreover, I will always be grateful to my girlfriend Martina for her many encouragements and her endless patience. In the end, I would like to thank Camilla Colombo and Andrea Muciaccia for the extremely valuable guidance they have given me in the last months.

1 | Introduction

1.1. Background

From the beginning of the space age on 4 October 1957 (with the launch of Sputnik 1) to the beginning of 2020, more than 5500 rocket bodies have been launched to insert into orbits over 9300 payloads [12]. Nowadays, payloads have a fundamental role for our society: they guarantee weather forecasting, broadcasting, navigation, telecommunications, and many other services. However, the rising demand of on-orbit services together with the advent of large constellations and the technological advance is causing the overcrowding of Earth space region. Specifically, ESA's annual space environment report [34] shows that the number of geosynchronous satellites has been doubled in the last 20 years and that number of satellites orbiting in Low Earth Orbits (LEO) is three time larger than the one in 2000. As postulated by Donald Kessler in 1978 [17], the rising number of activities in space will result in the generation of growing clouds of space debris, leading to a potential threat for future space sustainability. With the term space debris, the scientific community indicates the collection of all man-made non-operative objects orbiting around Earth, including decommissioned satellites, spent rocket bodies, objects generated by fragmentation events (such as collisions and explosions) and, also, mission-related objects.

Space debris are regularly tracked with optical and radar observations and their orbital parameters are collected in space catalogues. Actually, as shown by ESA's annual space environment report [34], the U.S. Strategic Command's (STRATCOM) Space Surveillance Network (SSN) has tracked more than 16000 uncontrolled objects orbiting around Earth. Catalogued debris includes approximately 6676 payload fragmentation debris, 1957 rocket bodies, 6197 rocket body fragmentation debris and 881 mission-related debris. The relatively small number of catalogued fragmentation and mission-related debris is associated to cataloguing capabilities, which are limited to objects of approximately 10 cm in diameter in Low Earth Orbit (LEO) and only about 1 meter in Geosynchronous Earth Orbit (GEO) [31]. It is important to highlight that dominant source of debris population since the 1960s is represented by disruptive disintegration of satellites. In 2011, IADC assessed

that fragmentation debris constitute more than 60 % of the total number of catalogued debris population. For the sake of clarity, it could be useful to highlight that two of the most dramatic breakup events registered in last years, the intentional destruction of Fengyun 1C in 2007 and the collision between Cosmos 2251 and Iridium 33 spacecrafts, were able to generate more than 5000 debris fragments in the near-Earth region [15].

Actually, LEO results to be the most highly congested region in near-Earth space: it is estimated that several hundred thousand debris between 1 and 10 cm are orbiting around Earth and that the number of fragments between 1 mm and 1 cm exceeds the 100 million. While GEO region is characterised by a lower debris density. It is assessed that about 3000 fragments as small as 10 cm are orbiting close to the Geosynchronous region [15].

Even if millimetre and centimetre sized fragments are not trackable and catalogued, they represent a huge hazard for operational satellites. Objects larger than 1 cm could destroy a satellite in case of collision, while millimetre sized objects are supposed to cause relevant anomalies on spacecraft operations, leading potentially to the failure of the mission [18]. Any collision with a single debris generates new fragments that may collide with other objects, leading to a chain effect. This mechanism may produce an uncontrolled growth of the space debris density, defined as Kessler syndrome [17], that may interfere with the future exploitation and sustainability of the near-Earth space. To mitigate this effect, several standards have been defined to minimise the possibility of potential or accidental breakups [15]. For example, these guidelines imply the adoption of passivation measures devoted to the reduction of explosions likelihood, the use of active avoidance manoeuvres to limit the probability of collisions during the operational lifetime of the satellite and the adoption of disposal manoeuvres to reduce the collision risk between uncooperative satellite and operative spacecrafts and to allow the natural decay of satellite within 25 years from the end of the mission. Despite the introduction of the aforementioned guide-lines, a risk of accidental breakups remains. Therefore, obtaining a reliable picture of the evolution of space debris environment is becoming a key element to reduce collision prob-ability, to identify possible mitigation strategies, to plan active debris removal missions and to suggest future policies to increase the sustainability of the space activities.

1.2. Literature review

Many methods and algorithms have been developed to propagate the space debris and to estimate the collision probability and the resulting vulnerability of different operational satellites. This section introduces a brief overview of these methods together with their advantages and disadvantages. The debris evolutionary models can be subdivided into

two main categories: probabilistic and deterministic methods. Deterministic methods imply the piece-wise propagation of all the fragments and are discussed in Section 1.2.1. While probabilistic models allow to propagate globally the debris cloud and are reviewed in Section 1.2.2. Moreover, Section 1.2.3 introduces a brief review of the main techniques used to estimate the impact hazard.

In addition to these methods, more literature review was needed to derive the method proposed in this thesis. Section 1.2.4 is devoted to briefly review the main techniques suitable for solving a general Partial Differential Equation (PDE).

1.2.1. Deterministic evolutionary models

Deterministic approaches allow to propagate fragments individually and, in general, are characterized by high-fidelity dynamical models and a very accurate prediction of the motion of each fragment. For example, Anderson and Schaub [3] developed a deterministic method based on the numerical integration of two-body equations of motion including 4x4 gravitational model, luni-solar perturbations and solar radiation pressure (SRP) to analyse the effects of on-orbit fragmentation events in the geosynchronous orbit regime. However, these techniques exhibit a huge drawback: the required computational time is strongly dependent on the number of fragments included inside the simulations and, thus, number of fragments must be limited to guarantee that computational effort is compliant with current computing capabilities. To overcome this issue, several authors decided to focus mainly only on objects larger than 0.8-1.0 m [3]. But, the inclusion of small fragments in debris modelling could be useful to obtain a more complete picture of the debris environment and to avoid underestimating the collision risk or misinterpreting the effect of mitigation and remediation measures.

Another strategy adopted to reduce the number of samples for each run consists in defining some representative objects, grouping together several fragments. However, this technique could potentially lead to the underestimation of the likelihood of a close encounter and to the overestimation of the collision probability. Therefore, to include centimetre sized objects in the model and to avoid the adoption of representative objects, fully analytical approaches have been developed for the propagation of uncontrolled objects in GEO.

Valk et al. [37] provided a Hamiltonian formulation of the equations of motion of a single space debris orbiting the geostationary ring. This theory was formulated using canonical and non-singular elements for eccentricity and inclination and included the luni-solar perturbation together with the influence of the Earth gravity field expanded in spherical harmonics, paying a particular attention to the resonance occurring for geosynchronous

objects. Lately, Casanova et al. [9] proposed an improvement of Valk's approach by developing an analytical model able to propagate space debris in the geostationary ring under the effects of Earth oblateness, solar radiation pressure, and the luni-solar perturbation.

Anderson and Schaub [3] derived a harmonic oscillator model to study the longitudinal evolution of the space debris captured by one of the stable gravitational wells. The adopted dynamical model was simplified by assuming the $J_{2,2}$ term only. Thus, solar radiation pressure, luni-solar perturbation and higher-order harmonics appearing in a full expansion of the Earth gravitational potential were neglected and the longitudinal motion of a librating object could be expressed as [3]:

$$\lambda(t) = \psi_m \cos\left(\frac{2\pi t}{T_l} - \phi\, \text{sgn}\left(\dot{\psi}_0\right)\right) + \lambda_{1,2} \tag{1.1}$$

where the libration amplitude ψ_m, the phase shift ϕ, the period of libration T_l, and angular-velocity-like parameter were computed as [3]:

$$\begin{cases} \sin\psi_m = \sqrt{\sin^2\psi_0 + \dfrac{\dot{\psi}_0^2}{k^2}}, \\[3mm] \phi = \arccos\left(\dfrac{\psi_0}{\psi_m}\right), \\[3mm] T_l = \dfrac{4}{k}K\left(\sin\psi_m\right), \\[3mm] k = \dfrac{6 n_{GEO} R_\oplus \sqrt{J_{2,2}}}{r_{GEO}}. \end{cases} \tag{1.2}$$

Here, $K\left(\sin\psi_m\right)$ is the complete elliptic integral of the first kind, $\lambda_{1,2}$ denotes the closest gravitational well, $\psi = \lambda - \lambda_{1,2}$ and the initial longitudinal drift rate is equal to $\dot{\psi}_0 = n_0 - n_{GEO}$. Another weak point associated to deterministic methods is related to the procedure needed for the computation of the debris density and, thus, the collision probability. Spatial density distribution n must be calculated by applying a binning strategy and discretizing the entire domain; however, these methods show a high sensitivity to the selected grid spacing.

$$n = N_{frag}/V_{cell} \tag{1.3}$$

1.2.2. Probabilistic evolutionary models

Instead of propagating fragments individually, probabilistic methods allow to estimate fragments density evolution by considering the entire debris clouds as a continuum. These models have been historically used to describe the evolution of various systems in different

physical spaces and phase spaces. For example, Nikolai N. Gorïkavyi adopted a probabilistic approach to study the dynamical evolution of interplanetary dust, while McInnes [29] exploited the continuity equation to model the evolution of a swarm of self-propelled 'smart dust' devices in heliocentric orbit driven by solar radiation pressure. Nazarenko [32] was one of the first authors that decided to adopt a statistical method to describe space debris density evolution. In particular, he developed a probabilistic approach based on the continuity equation to analyse space debris evolution in the region of low orbits under the effect of atmospheric disturbances.

In last years, several authors improved Nazarenko's method. Kebschull et al. [16] implemented a model based on source and sink mechanisms to study the collision probability and the environmental criticality in the Low Earth Orbit region. The proposed approach predicted the evolution of intact bodies and fragments taking into account natural decay, post mission disposal measures and yearly launches. The modification of the environment was expressed through a simple differential equation and was integrated by applying a Euler method.

Letizia and Colombo [20] further developed the method by proposing an analytical density-based model to describe debris evolution in LEO after fragmentation events. Latter approach consisted simply in considering fragments population as a fluid with continuous properties, whose density changed under the aerodynamic drag effects, and, thus, deriving the evolution of the density through the continuity equation. The algorithm developed by Letizia [20] was essentially made by a breakup model to generate fragments and their characteristics, a model to convert debris positions into a continuous density function for the derivation of the initial conditions for the continuity equation, a numerical model to propagate fragments individually until analytical method becomes applicable and an analytical formulation to describe the time evolution of cloud density. This method resulted to be particularly convenient for the space debris propagation due to its limited computational effort, its capability of including objects of any size and its flexibility. Letizia et al. [22] applied the aforementioned method to compute the collision probability in LEO regime. Thanks to its limited computational time and its good accuracy, the method has been applied to study the impact of different breakups on various target spacecrafts (influence matrix) and to build a map of collision probability by varying the inclination and the altitude of the simulated breakup. Lately, Letizia et al. [23] developed a bi-dimensional extension of the continuity equation method for the space debris collision analysis. In particular, Letizia et al. [23] proposed an analytical method to propagate fragment clouds on the phase space defined by the semi-major axis and the eccentricity under the effect of aerodynamic drag. The 2D propagation provided a more accurate description of the frag-

ment distribution with respect to the mono-dimensional approach, allowed to precisely capture the density peak location and to halve the error on its height if compared to the 1D propagation. In the end, in 2016, Letizia et al. [25] proposed a multidimensional extension of the continuity equation method for debris clouds evolution. This approach allowed to include also the effect of the Earth's oblateness inside the dynamical model and to improve the description of the drag effect considering the distribution of area-to-mass ratio and eccentricity among the fragments. The ability of this density-based model consists in analysing large debris clouds with limited computational effort (both in terms of simulation time and RAM), making this strategy suitable to simulate many breakup scenarios and to build an environmental index based on the assessment of their consequences. Indeed, Letizia et al. [26] adopted the this model to assess breakup effects on operational aspects of space debris activities, analysing variations in close conjunction alerts and collision avoidance manoeuvres. Therefore, Letizia et al. [26] defined the ECOB environmental index as function of properties (area, mass) of several active satellites and their probability of collision.

1.2.3. Collision probability estimation

Once the time evolution of the space debris is available, the local density of the fragments should be converted into a collision probability. Despite collision risk is a probabilistic measure, it can be computed applying both probabilistic and deterministic evolutionary methods. Many different techniques can be applied to provide an estimation of the collision hazard.

Kessler et al. [17] developed a statistical approach to compute the collision probability for orbiting objects. Exploiting the analogy to the kinetic gas theory, Kessler estimated the number of impacts per unit cross-sectional area F as:

$$F = S\Delta v \tag{1.4}$$

where S is the debris spatial density and Δv is the velocity of the fragments relative to the target. The average number of collisions N was considered as function of number of impacts F, collisional cross-sectional area A_c and time t [17]:

$$N = FA_c t \tag{1.5}$$

To finally compute the collision probability between two orbiting objects, Kessler et al. [17] calculated the spatial density of a single object as:

$$S_i = \frac{t_i}{T_i}\frac{1}{\Delta V} \tag{1.6}$$

where T denotes the orbital period and ΔV is the selected control volume. Therefore, Kessler computes the collision rate between two objects as:

$$\eta_{i,j}(\Delta V) = S_i S_j \Delta v A_c \Delta V \tag{1.7}$$

In the end, the collision probability was estimated by applying the Poisson function:

$$P_c = 1 - exp^{-\eta} \tag{1.8}$$

Liou [28] developed the "Cube" algorithm to extend Kessler method to large set of objects. This approach is based on the uniform sampling of the system in time and collision risk is evaluated trough Equation (1.7). The main advantage of this method consists in the fact that computational time increases linearly with the number of objects, not quadratically.

In the end, a statistical approach, analogous to Kessler's one, has been proposed by McKnight and Di Pentino [31] to compute the collision probability in GEO between an operative satellite and a debris cloud. McKnight highlighted that the dynamics of the derelict objects relative to the station-kept operational satellites is distinctly different than in LEO and, thus, proposed an alternative collision hazard methodology applying a satellite-centered and longitude-dependent reference frame. The developed collision probability calculation is based on the kinetic theory of gases and is driven by the following expression [31]:

$$P_c = 1 - exp^{-S\Delta v A_c t} \tag{1.9}$$

The evaluation of local spatial debris density S is performed counting the debris falling inside a rectangular volume centred on the GEO arc with a length along the GEO arc of 736 km (equivalent to 1° in longitude), depth of 400 km in the altitude dimension (i.e. ± 200 km), and a height of 736 km (equivalent to 1° in latitude). McKnight concluded that the probability of collision at in the geostationary regime is not uniform by longitude: collision hazard is seven time higher I correspondence of gravitational wells (L1) and (L2).

1.2.4.   Resolution methods for Partial Differential Equations

This subsection is devoted to the discussion of methods suitable for solving the continuity equation. The solution will be exploited to recover the analytical formulation of the cloud propagation.

Method of characteristics

The method consists in reducing a Partial Differential Equation (PDE) to a set of Ordinary Differential Equations (ODE). For a first order PDE, this technique allows to recover the characteristic curves, along which the PDE becomes a simple ODE. The latter can be solved along the characteristic curves and transformed into a solution of the original PDE. Given a general quasi-linear partial differential equation [12]:

$$a(x,t,n)\frac{\partial n}{\partial t} + b(x,t,n)\frac{\partial n}{\partial x} = c(x,t,n). \tag{1.10}$$

where t represents time, x a generic time dependent variable, n the density and $a(x,t,n)$, $a(x,t,n)$, $a(x,t,n)$ are generic functions of t, x and n. Suppose that a solution $n(x,t)$ is known, and consider the surface graph $S \equiv \{(x,t,n(x,t))\}$, the normal vector to this surface is given by [12]:

$$N(x,t) = \left(\frac{\partial n}{\partial t}, \frac{\partial n}{\partial x}, -1\right) \tag{1.11}$$

Inserting Equation (1.11) intoEquation (1.10), the following relation is found [12]:

$$(a(x,t,n), b(x,t,n), (x,t,n)) \cdot N(x,t) = 0 \tag{1.12}$$

This implies that the vector field (a, b, c) is tangent to the surface S at every point. In other words, characteristics curves result to be tangent at each point to the characteristic direction, defined by (a, b, c) and, thus, can be defined by the following ordinary differential equations:

$$\begin{cases} \dfrac{\mathrm{d}t}{\mathrm{d}\tau} = a(x,t,n) \\[2mm] \dfrac{\mathrm{d}x}{\mathrm{d}\tau} = b(x,t,n) \\[2mm] \dfrac{\mathrm{d}n}{\mathrm{d}\tau} = c(x,t,n) \end{cases} \tag{1.13}$$

where τ expresses a parametrisation of the characteristic lines.

Density Mapping

Density mapping relies on the assumption that no source or sink terms are present inside the domain and, thus, that density is conserved locally. Given the solution of the dynamics in Equation (3.2), as:

$$x = \varphi\left(x_0\right) \tag{1.14}$$

the mapping of the density can be obtained as in [36]:

$$n(\boldsymbol{x}, t) = \frac{n\left(\boldsymbol{\varphi}^{-1}(\boldsymbol{x}), t_0\right)}{|\det \boldsymbol{J}|} \tag{1.15}$$

with the Jacobian, $\boldsymbol{J} \in \mathbb{R}^{D \times D}$, defined as:

$$J_{ij} = \frac{\partial \varphi_i}{\partial x_{0,j}} \quad i, j = 1, 2, \ldots, D \tag{1.16}$$

It is important to highlight that, in the absence of sources and sinks, method of characteristics and density mapping provide equal solutions.

1.3.   Scope of the Thesis

This thesis aims to answer several fundamental questions of interest to the GEO operator community. Firstly, this work presents a density-based model for the propagation of single debris clouds inside the geosynchronous region. In particular, this study fills a void in the literature by developing a fully analytical model to study the evolution of debris clouds generated by fragmentation events under the $J_{2,2}$ effect. The proposed approach is, therefore, based on the continuity equation and cloud evolution is analysed in longitude and drift longitude $(\lambda, \dot{\lambda})$ phase space to identify the longitude slots most susceptible to rising debris fluxes and to evaluate the correspondent longitude-dependent collision probability. Secondly, this work provides a fast and reliable tool to evaluate the effects of critical debris growth mechanisms, such as fragmentation events, on longitude-dependent congestion at GEO. In the end, it illustrates the effects of fragmentation events on long-term GEO sustainability providing a map of the collision probability in longitude and drift longitude phase space.

1.4.   Structure of the Thesis

This thesis is organized into four main chapters. The first one discusses the derivation of an analytical expression able to propagate a single object in GEO regime (Chapter 2). Chapter 2 presents the adopted simplified dynamical model, derives the equations of motion and exploits the analogy of the problem with the non-linear pendulum dynamics to obtain an analytical solution for the prediction of the longitudinal motion of a GEO object. The second one focuses on the derivation of the density-based model starting from the continuity equation (Chapter 3). Chapter 3 presents the derivation of the analytical cloud propagator by applying the method of characteristics to the continuity equation and introducing the analytical solution derived in Chapter 2. Third chapter shows the validation process of the cloud propagator and provides the expression for the computation of the collision probability (Chapter 4). In this chapter, the validation technique consists in a numerical and graphical comparison with results provided by a piece-wise propagator; while collision probability is computed by exploiting the kinetic gas theory and using results obtained with the analytical cloud propagator. In the end, Chapter 5 illustrates limitations of the developed algorithm together with future possible developments.

2 | Dynamics in GEO

The geostationary ring is an important resource for terrestrial satellite industry that is threatened by a rising number of space debris. As absence of atmospheric drag effects at Geosynchronous Earth Orbits (GEO) altitudes does not allow a natural decay of Geostationary objects and makes lifetimes of debris infinitely long, continuous conjunction assessments and collision avoidance manoeuvres must be performed to safeguard functional GEO satellites [1]. GEO satellites, however, must maintain a specific longitude slot during their whole operational lifetime and, thus, cannot simply phase shift to avoid the debris. Therefore, the analysis of the geostationary debris evolution is required to identify the longitude slots most susceptible to rising debris fluxes and forecast how frequently the operative satellites in these regions must potentially perform manoeuvres to mitigate conjunction scenarios. To predict the space debris longitudinal motion, numerical methods are avoided due to the large number of space objects to be propagated; therefore, in this chapter, an analytical model will be derived by using a simplified dynamical model including only the gravitational perturbations caused by both J_2 effect due to Earth oblateness and the tesseral $J_{2,2}$ effect. This chapter is divided into five main parts. Section 2.1 will introduce a brief overview on adopted reference frames and coordinate systems. Section 2.2 will review main perturbations acting on geostationary ring. Section 2.3 will focus on the derivation of the equation of motion starting from the simplified dynamical problem. In Section 2.4, the analogy between the derived equation of motion and the nonlinear pendulum dynamics will be exploited to develop an analytical model for space debris propagation and to compute period of libration. In the end, Section 2.5 investigates performances of the developed analytical model.

2.1. Reference frames and coordinate systems

Before deriving the equations of motion describing the longitudinal evolution of GEO objects, it could be useful to introduce a brief overview on reference frames and coordinate systems adopted for this study.

2.1.1.   Reference frames

The Earth centered inertial frame (ECI) and Earth-centered Earth-Fixed Frame (ECEF) are a suitable choice to study the geostationary environment. The ECI is an inertial reference frame, whose origin is the Earth's centre of mass and its fundamental plane coincides with the mean Equator plane at epoch J2000. The X-axis is oriented as vernal equinox at J2000, Z-axis is aligned with Earth axis of rotation (direction of north) at J2000 (01/01/2000 at noon GMT), while Y-axis completes the right-handed orthonormal reference frame. ECEF is a non-inertial reference frame whose origin is located at Earth's centre of mass. The X-axis passes through the Equator and Prime Meridian intersection, Z-axis is aligned with the North Pole, while Y-axis completes the right-handed orthonormal reference frame. This reference frame rotates around Z-axis with angular velocity equal to Earth rotational speed.

2.1.2.   Cartesian and spherical coordinates

Regarding the coordinate systems, both spherical coordinates and Cartesian ones seems to be a suitable choice to study geostationary ring dynamics. Cartesian coordinates describe a position with three orthogonal basis vectors, aligned with the three orthogonal axes of the coordinate frame. Position and its rates of change are then specified by a linear combination of these unit vectors. While, spherical coordinates are curvilinear coordinates commonly used to describe positions on a sphere or spheroid. In this coordinate system, a position is specified by the radial distance from a fixed origin, a polar angle measured from a fixed zenith direction and an azimuthal angle. To achieve a simpler expression of the gravitational field, in this work, spherical coordinates are preferred to Cartesian ones.

2.1.3.   Coordinates transformation

Given a position vector $\boldsymbol{r} = (r, \lambda, \phi)$ in a spherical coordinate system, the corresponding position vector in Cartesian coordinates $\boldsymbol{p} = (x, y, z)$, can be obtained as:

$$
\begin{cases}
x = r \cos \lambda \, \cos \phi, \\
y = r \sin \lambda \, \cos \phi, \\
z = r \sin \phi.
\end{cases}
$$

Furthermore, representing both Cartesian and spherical coordinate systems (Figure 2.1), it is possible to notice that unit vectors associated to the spherical coordinate system ($\hat{\boldsymbol{r}}$, $\hat{\boldsymbol{\lambda}}$, $\hat{\boldsymbol{\phi}}$) can be retrieved applying a simple rotation matrix to Cartesian coordinates versors

$(\hat{\boldsymbol{I}}, \hat{\boldsymbol{J}}, \hat{\boldsymbol{K}})$ [10]:
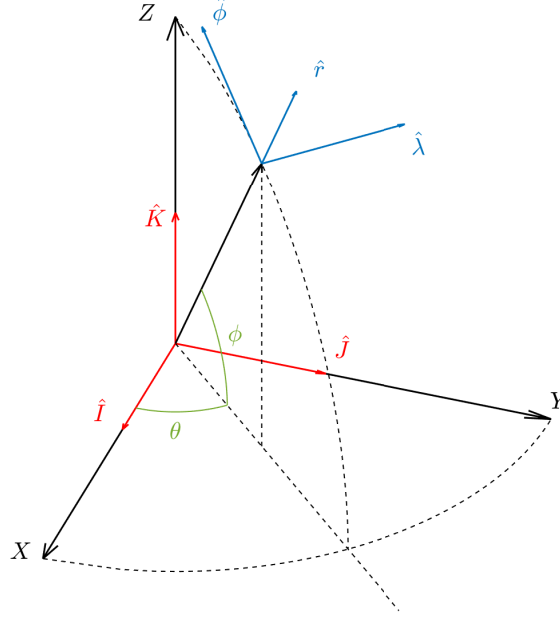

Figure 2.1: Geometry of Cartesian and spherical coordinate systems. The unit vectors for Cartesian frame $(\hat{\boldsymbol{I}}, \hat{\boldsymbol{J}}, \hat{\boldsymbol{K}})$ can be seen with their spherical counterparts $(\hat{\boldsymbol{r}}, \hat{\boldsymbol{\lambda}}, \hat{\boldsymbol{\phi}})$.

$$R = \begin{bmatrix} \cos\phi & 0 & \sin\phi \\ 0 & 1 & 0 \\ -\sin\phi & 0 & \cos\phi \end{bmatrix} \begin{bmatrix} \cos\theta & \sin\theta & 0 \\ -\sin\theta & \cos\theta & 0 \\ 0 & 0 & 1 \end{bmatrix} = \begin{bmatrix} \cos\phi\cos\theta & \cos\phi\sin\theta & \sin\phi \\ -\sin\theta & \cos\theta & 0 \\ -\sin\phi\cos\theta & -\sin\phi\sin\theta & \cos\phi \end{bmatrix}$$

In this study, an ECI reference frame is adopted and both ϕ and θ are considered as time dependent variables. ϕ coincides with GEO object latitude, while θ represents GEO object's longitude relative to the vernal equinox and is defined as sum between right ascension of Greenwich meridian, local longitude and Earth rotation contribution:

$$\theta = \alpha_G + \Omega_\oplus \cdot t + \lambda(t)$$

Thus, the expressions of rotating frame unit vectors can be obtained by substituting last expression inside the rotation matrix:

$$\begin{cases} \hat{\boldsymbol{r}} = \cos\phi\cos\theta\hat{\boldsymbol{I}} + \cos\phi\sin\theta\hat{\boldsymbol{J}} + \sin\phi\hat{\boldsymbol{K}}, \\ \hat{\boldsymbol{\lambda}} = -\sin\theta\hat{\boldsymbol{I}} + \cos\theta\hat{\boldsymbol{K}}, \\ \hat{\boldsymbol{\phi}} = -\sin\phi\cos\theta\hat{\boldsymbol{I}} - \sin\phi\sin\theta\hat{\boldsymbol{J}} + \cos\phi\hat{\boldsymbol{K}} \end{cases}$$

Moreover, time derivatives of rotating frame unit vectors can be computed in few passages [10]:

$$\begin{cases} \dfrac{d\hat{r}}{dt} = \dot{\theta}\cos\phi\,\hat{\boldsymbol{\lambda}} + \dot{\phi}\,\hat{\boldsymbol{\phi}}, \\[2mm] \dfrac{d\hat{\boldsymbol{\lambda}}}{dt} = -\dot{\theta}\cos\phi\,\hat{r} + \dot{\theta}\sin\phi\,\hat{\boldsymbol{\phi}}, \\[2mm] \dfrac{d\hat{\boldsymbol{\phi}}}{dt} = -\dot{\phi}\,\hat{r} - \dot{\theta}\sin\phi\,\hat{\boldsymbol{\lambda}}, \\[2mm] \dfrac{d^2\hat{r}}{dt^2} = \left(-\dot{\theta}\cos^2\phi - \dot{\phi}^2\right)\hat{r} + \left(\dfrac{1}{\cos\phi}\dfrac{d}{dt}\left(\dot{\theta}^2\cos^2\phi\right)\right)\hat{\boldsymbol{\lambda}} + \left(\dot{\theta}^2\cos\phi\sin\phi + \ddot{\phi}\right)\hat{\boldsymbol{\phi}}. \end{cases}$$

and, finally, the generic expression of acceleration in spherical coordinates can be derived recalling that a position vector can be defined as $\boldsymbol{r} = r\,\hat{r}$:

$$\ddot{\boldsymbol{r}} = \ddot{r}\,\hat{r} + r\,\dfrac{d^2\hat{r}}{dt^2} = \begin{Bmatrix} \ddot{r} - r\dot{\theta}^2\cos^2\phi - r\dot{\phi}^2 \\[2mm] \dfrac{1}{r\cos\phi}\dfrac{d}{dt}\left(r^2\dot{\theta}\cos^2\phi\right) \\[2mm] \dfrac{1}{r}\dfrac{d}{dt}\left(r^2\dot{\phi}\right) + r\dot{\theta}^2\cos\phi\sin\phi \end{Bmatrix} \tag{2.1}$$

2.2. GEO region main perturbations

After introducing reference frames and coordinate systems, a brief review of major perturbations acting in the geostationary ring should be performed. First, the **third body forces** that are resulting disturbances caused by the presence of gravitating objects in addition to the primary attractor. Sun and Moon are the main perturbative sources for satellites orbiting around Earth. Particularly, in GEO, luni-solar perturbation will induce a 53-year cyclical precession of the orbit plane [6]. The **solar radiation pressure** is caused by direct electromagnetic radiation coming from Sun. Magnitude and direction of the resultant acceleration depends on illumination area-to-mass ratio, surface reflectivity and orientation of the orbiting object. In GEO, this produces a significant drift in the eccentricity vector of the orbit [39]. The **Earth's non-spherical perturbation** is caused by the non-spherical mass distribution of Earth. Earth's non-spherical gravitational field is modelled using the spherical harmonics approach, which consists in superimposing successive orders of non-spherical contributions to a main spherical gravitational field. The disturbing potential, therefore, can be expressed as a function of radius r, longitude λ

and latitude ϕ [10]:

$$U(r, \phi, \lambda) = \left(\frac{\mu}{r}\right) \left(\sum_{n=2}^{\infty} \left(\frac{R_\oplus}{r}\right)^n \left\{ J_n P_{n,0}[\sin(\phi)] + \sum_{m=0}^{n} J_{n,m} P_{n,m}[\sin(\phi)] \cos m\left(\lambda - \lambda_{n,m}\right) \right\} \right)$$

$$(2.2)$$

where n and m are respectively degree and order of the harmonics, $R_\oplus$ is Earth's equatorial mean radius, $P_{n,m}[\sin(\phi)]$ is the Associated Legendre Function of degree n, m, J_n is a n degree zonal harmonic potential and $J_{n,m}$ is a general tesseral harmonic potential. The terms $J_{n,m}$ and $\lambda_{n,m}$ are derived from coefficients of the Earth's gravity model as [27]:

$$J_{n,m} = \sqrt{C_{n,m}^2 + S_{n,m}^2}, \quad \lambda_{n,m} = \frac{1}{m} \arctan \frac{S_{n,m}}{C_{n,m}} \quad (2.3)$$

It could be useful to highlight that $n = m = 0$ corresponds to the spherical contribution, while $n = 2$ and $m = 0$ is associated to J_2 effect caused by Earth oblateness, which is the dominant term among zonal harmonics and is able to induce secular nodal regression and perigee precession. The $n = m = 2$ case corresponds to the resonant tesseral harmonics $J_{2,2}$, which is responsible of east-west perturbations on geostationary objects [27].

2.3. Simplified dynamical model in GEO

Once reviewed the main effects of GEO perturbing sources, a comparison on disturbing accelerations at geostationary altitude should be introduced. Figure 2.2 shows that the
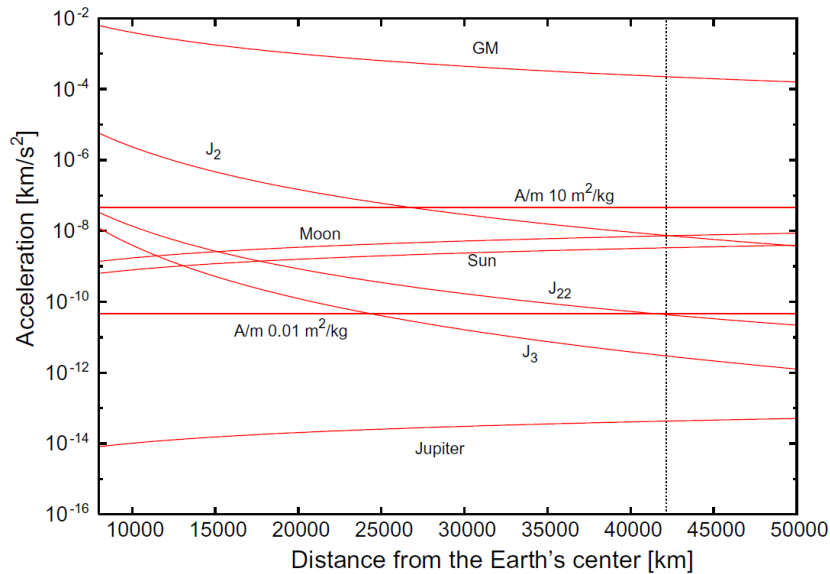

Figure 2.2: Order of magnitude of main perturbations in GEO. Credit to Valk et al. [38]

order of magnitude of luni-solar perturbation and SRP (in case of large area-to-mass ratios) are comparable in size to the one associated to Earth oblateness and that resonant tesseral harmonics will induce a slightly lower acceleration. However, the average variation of the semi-major axis caused by the lunisolar attraction and average value of the perturbation of mean longitude drift rate due to the solar radiation pressure equal zero in a day, meaning that both luni-solar perturbation and SRP have no long periodical effects on the semi-major axis of geostationary orbit [27]. Therefore, to achieve a long-term prediction of the longitudinal motion of large space debris clouds, a dynamical model including only the gravitational perturbation is adopted. In particular, as contributions of non-aspheric perturbation terms on the geostationary orbit tend to shrink by increasing the order of the model, a simplified dynamical model including only J_2 and $J_{2,2}$ effects is selected allowing the derivation of a fully analytical propagation. It is important to highlight that Anderson and Schaub [3] had already tested the accuracy of this simplified dynamical model against a high-fidelity propagator. As illustrated by Figure 2.3, Anderson concluded that this model is able to precisely predict the longitudinal motion of GEO objects within 2 years reducing significantly the computational effort.
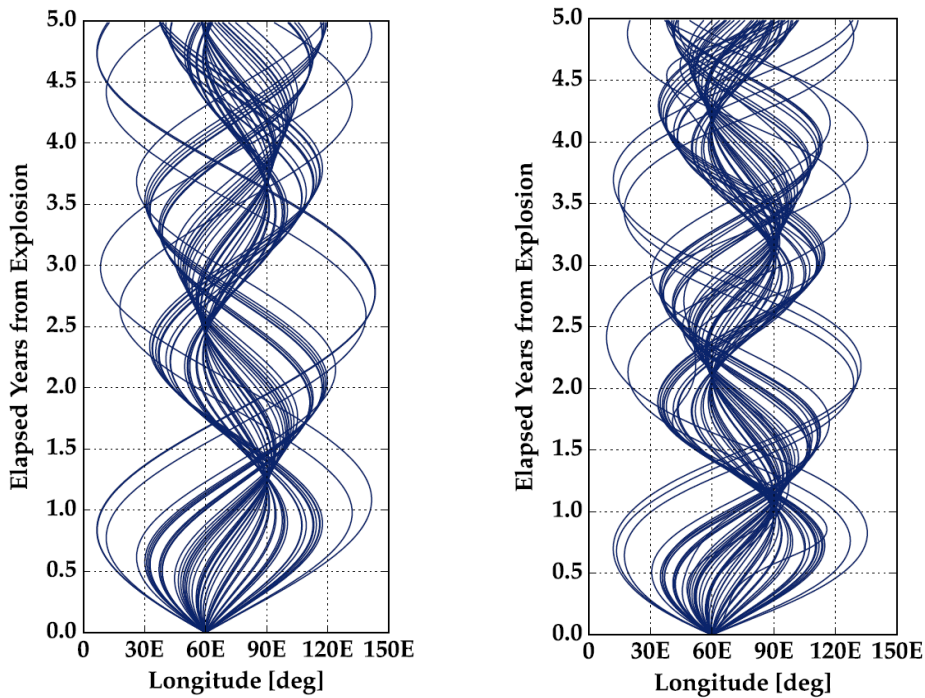
(a) Anderson's harmonic oscillator model (J_2 and $J_{2,2}$).

(b) Longitude histories(4x4 gravitation, luni-solar perturbations and SRP).

Figure 2.3: Accuracy of Anderson's harmonic oscillator model for predicting longitudes of librating fragments. Credit to Anderson and Schaub [3].

Therefore, under the assumptions previously introduced, the potential function describing GEO dynamics can be written as:

$$U(r, \phi, \lambda) = \left(\frac{\mu}{r}\right) \left[1 + J_2 \left(\frac{R_\oplus}{r}\right)^2 \left(\frac{3\sin^2\phi - 1}{2}\right) + 3\, J_{2,2} \left(\frac{R_\oplus}{r}\right)^2 \cos^2\phi \cos 2\left(\lambda - \lambda_{2,2}\right) \right]$$

(2.4)

where J_2 and $J_{2,2}$ are retrieved applying equation (2.3) to JGM-3 gravitational model [27], resulting in $J_2 = -1082.627 \cdot 10^{-6}$ and $J_{2,2} = 1.815528 \cdot 10^{-6}$.

Accordingly, acceleration components can be retrieved by differentiating gravitational potential in spherical coordinates (r, ϕ, λ):

$$\begin{cases} a_r = \dfrac{\partial U}{\partial r} = -\dfrac{\mu}{r^2} - \dfrac{3J_2\mu R_\oplus^2}{2r^4}\left(3\sin^2\phi - 1\right) - \dfrac{9J_{2,2}\mu R_\oplus^2}{r^4}\cos^2\phi \cos 2\left(\lambda - \lambda_{2,2}\right), \\[2mm] a_\lambda = \dfrac{1}{r\cos\phi}\dfrac{\partial U}{\partial \lambda} = -\dfrac{6J_{2,2}\mu R_\oplus^2}{r^4}\cos\phi \sin 2\left(\lambda - \lambda_{2,2}\right), \\[2mm] a_\phi = \dfrac{1}{r}\dfrac{\partial U}{\partial \phi} = \dfrac{3J_2\mu R_\oplus^2}{r^4}\sin\phi\cos\phi - \dfrac{6J_{2,2}\mu R_\oplus^2}{r^4}\cos\phi\sin\phi\cos 2\left(\lambda - \lambda_{2,2}\right). \end{cases}$$

(2.5)

Finally, the general form of the equations of motion is obtained by using equations (2.5) and (2.1).

$$\begin{cases} \ddot{r} - r\dot{\theta}^2\cos^2\phi - r\dot{\phi}^2 = a_r, \\[2mm] \dfrac{1}{r\cos\phi}\dfrac{d}{dt}\left(r^2\dot{\theta}\cos^2\phi\right) = a_\lambda, \\[2mm] \dfrac{1}{r}\dfrac{d}{dt}\left(r^2\dot{\phi}\right) + r\dot{\theta}^2\cos\phi\sin\phi = a_\phi. \end{cases}$$

(2.6)

Equation of motion can be further simplified to describe the longitudinal evolution of GEO space debris. Indeed, since uncontrolled GEO objects tend naturally to arrange on orbits with inclination between $-15°$ and $15°$ [6], space debris can be considered on quasi-equatorial orbits. Therefore, recalling that $\dot{\theta} = \Omega_\oplus + \dot{\lambda}$ and introducing the assumption that ϕ is a small angle ($\phi \approx 0$), previous system becomes:

$$\begin{cases} \ddot{r} = r(\Omega_\oplus + \dot{\lambda})^2 - \dfrac{\mu}{r^2} + \dfrac{3J_2\mu R_\oplus^2}{2r^4} - \dfrac{9J_{2,2}\mu R_\oplus^2}{r^4}\cos 2\left(\lambda - \lambda_{2,2}\right), \\[2mm] \ddot{\lambda} = \dfrac{1}{r}\left(-\dfrac{6J_{2,2}\mu R_\oplus^2}{r^4}\sin 2\left(\lambda - \lambda_{2,2}\right) - 2\dot{r}(\Omega_\oplus + \dot{\lambda})\right). \end{cases}$$

(2.7)

Then, by differentiating twice these two equations, a fourth-order equation in λ can be

retrieved:

$$\dddot{\lambda} + \Omega_\oplus^2 \ddot{\lambda} - 24\Omega_\oplus^3 J_{2,2} \frac{R_\oplus^2}{r^2} \sin 2\,(\lambda - \lambda_{2,2})\dot{\lambda} - 18\Omega_\oplus^4 J_{2,2} \frac{R_\oplus^2}{r^2} \sin 2\,(\lambda - \lambda_{2,2}) = 0 \qquad (2.8)$$

Since it has already been proven that time evolution of λ is a low-frequency solution with negligible damping [13], first and fourth derivative terms of equation (2.8) can be dropped obtaining the following non-linear differential equation:

$$\ddot{\lambda} = 18\Omega_\oplus^2 J_{2,2} \frac{R_\oplus^2}{r^2} \sin 2\,(\lambda - \lambda_{2,2}) \qquad (2.9)$$

It is important to highlight that only $J_{2,2}$ coefficient appears in last equation and, thus, that J_2 effect is completely dropped in this simplified dynamical model. Moreover, the assumption of quasi perfect geostationary orbit can be introduced to drop the dependence on time of the term $18\Omega_\oplus^2 J_{2,2} \frac{R_\oplus^2}{r^2}$ and to obtain a non-linear pendulum like equation:

$$\ddot{\lambda} = 18\Omega_\oplus^2 J_{2,2} \frac{R_\oplus^2}{a_{GEO}^2} \sin 2\,(\lambda - \lambda_{2,2}) \qquad (2.10)$$

Once derived the equation of motion, an analysis on equilibrium points, stability and integrals of motion is performed. Equilibrium points are found by re-writing equation (2.10) into a set of first-order differential equations and setting equal to zero time derivatives of λ and $\dot{\lambda}$.

$$\begin{cases} \dfrac{d\lambda}{dt} = \dot{\lambda}, \\ \dfrac{d\dot{\lambda}}{dt} = 18\Omega_\oplus^2 J_{2,2} \dfrac{R_\oplus^2}{a_{GEO}^2} \sin 2\,(\lambda - \lambda_{2,2})\,. \end{cases} \qquad (2.11)$$

Then, stability of equilibrium points is investigated by linearizing the equation of motion around those points and computing the roots of the corresponding characteristic equations. This analysis results in the identification of two stable gravitational wells (L1 and L2) among the four equilibrium points:

Equilibrium point	Longitude	Stability
L1	75.071° E*	Stable
L2	104.929° W	Stable
L3	14.929° W	Unstable
L4	165.071° E	Unstable

* E = East, W = West

Table 2.1: Equilibrium points.

In the end, the integral of motion is derived by manipulating equation (2.10). Firstly,

equation of motion is multiplied by $2\dot{\lambda}$ and $\sin 2(\lambda - \lambda_{2,2})$ is substituted with $2\sin(\lambda - \lambda_{2,2})\cos(\lambda - \lambda_{2,2})$:

$$2\dot{\lambda}\ddot{\lambda} - 36 \cdot 2\Omega_{\oplus}^2 J_{2,2} \left(\frac{R_{\oplus}}{a_{GEO}}\right)^2 \sin(\lambda - \lambda_{2,2}) \cdot \cos(\lambda - \lambda_{2,2})\dot{\lambda} = 0$$

Secondly, noticing that $2\dot{\lambda}\ddot{\lambda} = \frac{d\left(2\dot{\lambda}^2\right)}{dt}$ and $2\sin(\lambda - \lambda_{2,2})\cos(\lambda - \lambda_{2,2})\dot{\lambda} = \frac{d\left(\sin^2(\lambda - \lambda_{2,2})\right)}{dt}$, previous expression is re-written as:

$$\frac{d\left(\dot{\lambda}^2 - 36\Omega_{\oplus}^2 J_{2,2} \left(\frac{R_{\oplus}}{a_{GEO}}\right)^2 \sin^2(\lambda - \lambda_{2,2})\right)}{dt} = 0$$

Finally, integral of motion is derived by integrating previous expression:

$$E = \dot{\lambda}^2 - 36\Omega_{\oplus}^2 J_{2,2} \left(\frac{R_{\oplus}}{a_{GEO}}\right)^2 \sin^2\left(\lambda - \lambda_{2,2}\right) \tag{2.12}$$

Equation (2.12) is therefore used to investigate GEO objects behaviour in $(\lambda, \dot{\lambda})$ phase space. After recalling that this study focus on a lossless system since no dissipative forces are considered inside the dynamical model, it is important to highlight that a GEO object will preserve its initial energy E_0 and, thus, that its motion in the phase space will be energetically constrained. Indeed, given an initial energy E_0, future states must satisfy the following relation:

$$E_0 = \dot{\lambda}^2 - 36\Omega_{\oplus}^2 J_{2,2} \left(\frac{R_{\oplus}}{a_{GEO}}\right)^2 \sin^2\left(\lambda - \lambda_{2,2}\right) \tag{2.13}$$

Figure 2.4 provides a graphical representation of energy distribution in longitude and drift longitude phase space. This figure shows that longitude evolution can be distinguished into circulating and librating regimes depending on the initial energy level of the object. If $E > 0$, GEO objects exhibit a drifting behaviour, moving between L3 and L4 equilibrium points. Conversely, objects with $E < 0$ are captured by one of gravitational wells, showing a circulating motion in $(\lambda, \dot{\lambda})$ phase space. Aforementioned regimes are energetically divided by a separatrix ($E = 0$), which is defined by the following expression:

$$\dot{\lambda}_{spx} = \pm \Omega \sin(\lambda - \lambda_{2,2}) \tag{2.14}$$

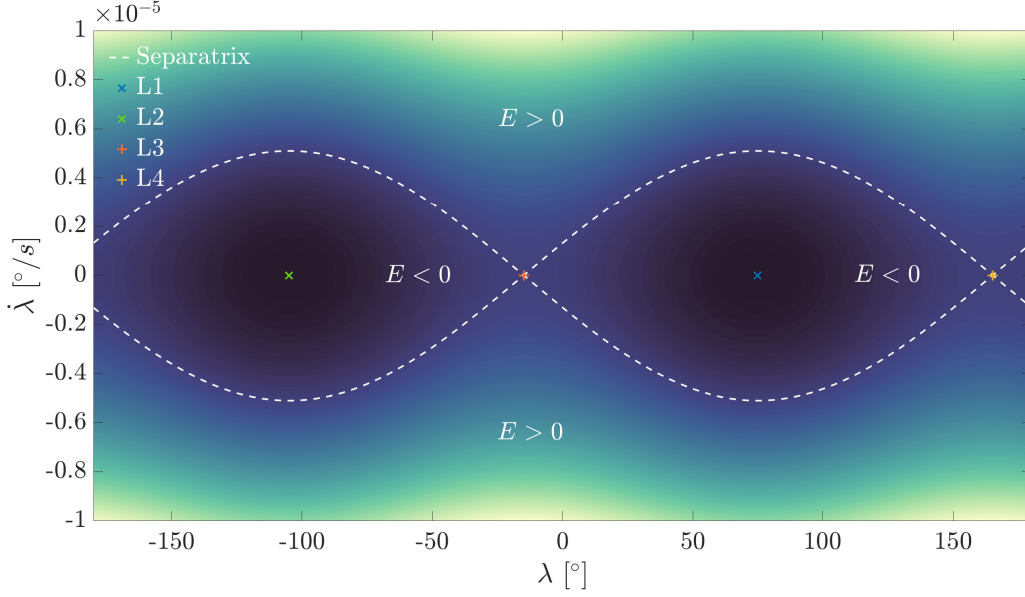where $\Omega = 6\,\Omega_{\oplus}\sqrt{J_{2,2}}\frac{R_{\oplus}}{a_{GEO}}$.
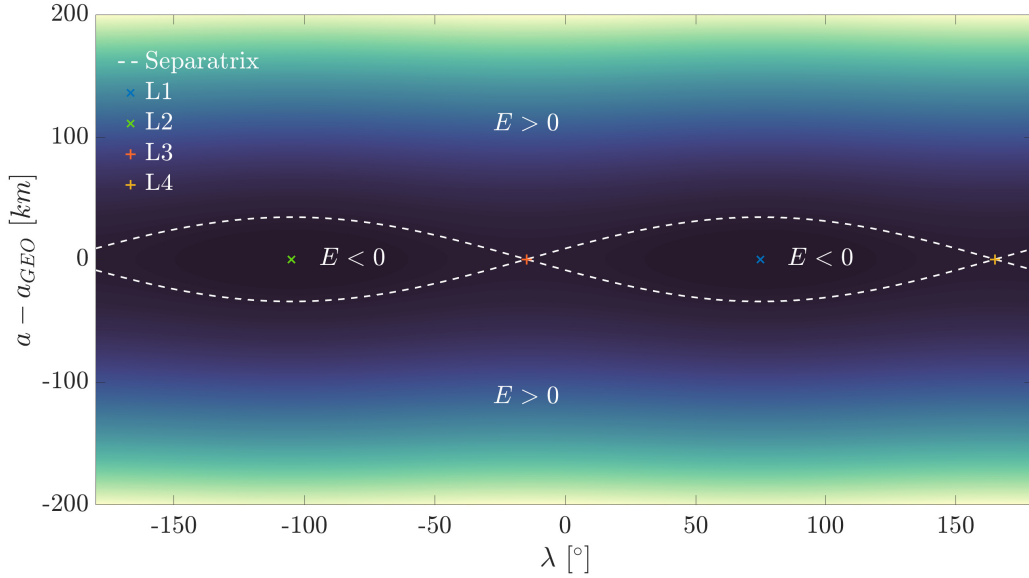
Figure 2.4: $(\lambda,\dot{\lambda})$ Phase space.

The same analysis can be performed in $(\lambda,\Delta a)$ phase space (Figure 2.5) exploiting equation Equation (2.12) and the following relation between longitudinal drift and semi-major axis:

$$\dot{\lambda} = -\frac{3\Omega_\oplus}{2a_{GEO}}\Delta a = -\frac{3\Omega_\oplus}{2a_{GEO}}(a - a_{GEO}) \tag{2.15}$$

As depicted in Figure 2.5, GEO objects with semi-major axis lower than ideal geosynchronous orbit radius are characterised by an eastward longitudinal drift, while objects with higher orbital energy reveal a westward longitudinal drift. As for the $(\lambda,\dot{\lambda})$ phase space, the $(\lambda,\Delta a)$ phase space presents circulating and drifting regimes, separated by the separatrix:

$$\Delta a_{spx} = \pm\frac{2a_{GEO}\,\Omega}{3\,\Omega_\oplus}\sin(\lambda - \lambda_{2,2}) \tag{2.16}$$

It is fundamental to notice that the circulating motion occurs in proximity to the gravitational well closest to the initial longitude λ_0. For example, despite the circulating regions close to L1 and L2 share the same energy levels, an L1 object would be energetically bounded around the correspondent gravitational well and would not not be able to reach L2 librating region.

Figure 2.5: $(\lambda, \Delta a)$ Phase space.

2.4.   Analytical solution

This section is dedicated to the study carried out to identify the analytical solution of Equation (2.10). The first step consists in performing a change of variable, substituting λ with the modified longitude ϑ:

$$\vartheta = 2(\lambda - \lambda_{2,2} \pm \frac{\pi}{2}) \tag{2.17}$$

where ϑ represents twice the distance from a stable equilibrium point. Its introduction allows to re-write the equation of motion as a simple nonlinear pendulum equation:

$$\ddot{\vartheta} + \Omega^2 \sin \vartheta = 0 \tag{2.18}$$

Before deriving the analytical solution of Equation (2.18), some energy considerations must be introduced. As the considered pendulum is a lossless system, the total energy of the system will be preserved for all instances. The latter can be obtained as the sum between kinetic and potential energy evaluated at time zero:

$$\hat{E}_0 = \dot{\vartheta}_0^2 + E_p \sin^2 (\vartheta_0/2) \qquad \text{with} \qquad E_p = 4\Omega^2$$

Figure 2.6 shows that pendulum is able to swing over if its initial energy $\hat{E}_0$ is greater than the maximum potential energy E_p, while if $\hat{E}_0 < E_p$ pendulum swings only back and

forth. It is important to notice that, due to the similarity between the pendulum and the Equation (2.10) formulations, the swinging case corresponds to a drifting object in $(\lambda, \dot{\lambda})$ phase space, while the circulating motion is represented by a nonlinear pendulum with insufficient energy for swinging over.
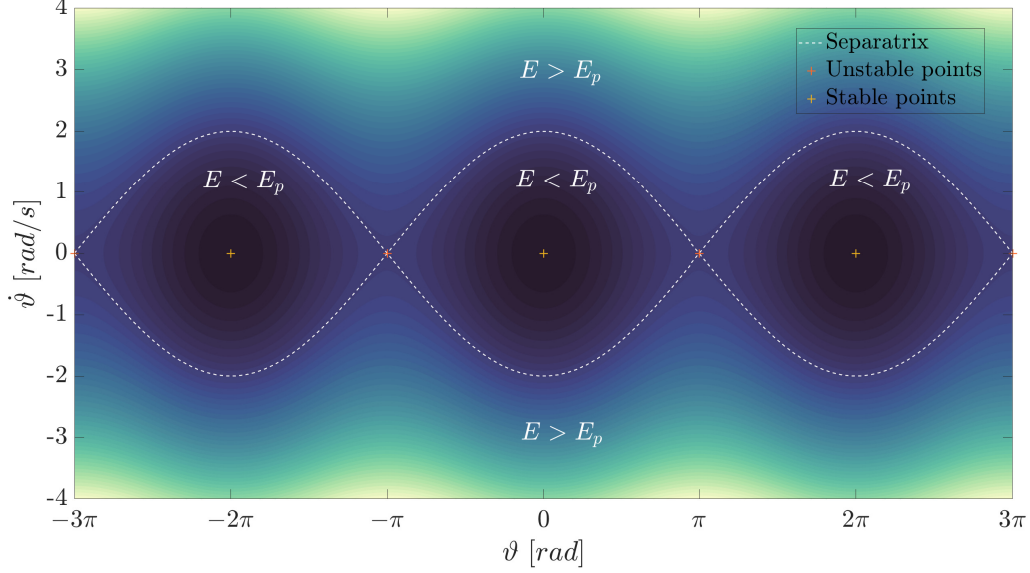

Figure 2.6: Nonlinear pendulum energy in $(\vartheta, \dot{\vartheta})$ phase space. Plot is generated with $\Omega = 1$.

Starting from the analysis of the swinging case, the conservation of energy is exploited to calculate the angular velocity of the pendulum $\dot{\vartheta}$:

$$\dot{\vartheta}^2 = \hat{E}_0 - E_p \sin^2 \vartheta / 2 \geq \hat{E}_0 - E_p \geq 0 \tag{2.19}$$

Hence, noticing that the angular velocity of a swinging pendulum maintains unaltered its sign, the square root of previous expression is obtained by substituting the absolute value with initial sign of the angular velocity:

$$\dot{\vartheta} = \text{sgn}(\dot{\vartheta}_0)\sqrt{\hat{E}_0 - E_p \sin^2 \vartheta / 2} \tag{2.20}$$

Defining k as the square root of the ratio $\hat{E}_0 / E_p$, $\varkappa$ as the inverse of k and substituting $\vartheta = 2\,\theta$, Equation (2.20) can be rewritten as follows:

$$\frac{d\theta}{dt} = \text{sgn}(\dot{\theta}_0)k\Omega\sqrt{1 - \varkappa^2 \sin^2 \theta} \tag{2.21}$$

Then, separation of variable is performed to obtain a more suitable form:

$$\frac{d\theta}{\sqrt{1 - \varkappa^2 \sin^2 \theta}} = \text{sgn}(\dot{\theta}_0) k \Omega dt \tag{2.22}$$

For the sake of clarity, before integrating Equation (2.22), the definitions of incomplete and complete integrals of the first kind are recalled.

$$F(\Phi \mid k) = \int_0^\Phi \frac{d\theta}{\sqrt{1 - k^2 \sin^2(\theta)}} \qquad F(\pi/2 \mid k) = K(k) = \int_0^{\pi/2} \frac{d\theta}{\sqrt{1 - k^2 \sin^2(\theta)}}$$

Observing carefully elliptic integral expressions, it is possible to notice that integration from t_0 to t of Equation (2.22) will lead to the following solution:

$$F(\vartheta/2 \mid \varkappa) - F(\vartheta_0/2 \mid \varkappa) = \text{sgn}\left(\dot{\vartheta}_0\right) k \Omega [t - t_0] \tag{2.23}$$

Moreover, highlighting that the absolute value of the initial angle is bounded by π, the formulation of $F(\vartheta_0/2 \mid \varkappa)$ can be rewritten as:

$$F(\vartheta_0/2 \mid \varkappa) = F(\arcsin(k_0) \mid \varkappa) = \text{sn}^{-1}(k_0 \mid \varkappa) \tag{2.24}$$

where sn is a JACOBI elliptic function and k_0^2 is the ratio between the initial potential energy and E_p [33]. Therefore, following Ochs' approach [33], Equation (2.23) takes the form

$$F(\vartheta/2 \mid \varkappa) = \theta(t) \tag{2.25}$$

in which the linear function $\theta(t)$ is expressed as:

$$\theta(t) = \text{sgn}\left(\dot{\vartheta}_0\right) k \Omega [t - t_0] + \text{sn}^{-1}(k_0 \mid \varkappa) \tag{2.26}$$

To retrieve an analytical solution, sn Jacobi elliptic function must be applied to Equation (2.25). Special diligence is required for this mathematical passage because $\text{sn}(\theta(t) \mid \varkappa)$ function is capable of delivering $\sin(\vartheta/2)$ only if the sign on the right-hand side is corrected. Thus, the solution becomes:

$$\sin(\vartheta/2) = \text{sn}(\theta(t) \mid \varkappa) \, \text{sgn}(\text{cn}(\theta(t) \mid \varkappa)). \tag{2.27}$$

In the end, angular velocity can be found by inserting Equation (2.27) in Equation (2.20)

and final solution becomes:

$$\begin{cases} \theta(t) = \mathrm{sgn}\left(\dot{\vartheta}_0\right) k\Omega\left[t - t_0\right] + \mathrm{sn}^{-1}\left(k_0 \mid \varkappa\right), \\ \vartheta(t) = 2\arcsin(\mathrm{sn}(\theta(t) \mid \varkappa))\,\mathrm{sgn}(\mathrm{cn}(\theta(t) \mid \varkappa)), \\ \dot{\vartheta}(t) = \mathrm{sgn}\left(\dot{\vartheta}_0\right)\sqrt{\hat{E}_0}\mathrm{dn}(\theta(t) \mid \varkappa). \end{cases} \tag{2.28}$$

where $\mathrm{cn}, \mathrm{sn}, \mathrm{dn}$ are JACOBI elliptic functions. Theoretically, analytical solution should be derived also for $\hat{E}_0 < E_p$ case because Equation (2.19) is no longer valid and, also, sign of angular velocity of the pendulum can change during the motion. However, Ochs [33] demonstrated the research of a new analytical solution is not necessary, because Equation (2.28) holds also for a pendulum with insufficient energy for swinging over. Moreover, a simpler solution can be derived in case of null initial angular velocity. Indeed, for this peculiar initial condition, k result to be equal to k_0 and the analytical solution becomes:

$$\begin{cases} \theta(t) = \Omega\left[t - t_0\right] + \mathrm{K}(k), \\ \vartheta(t) = 2\arcsin(k\,\mathrm{sn}(\theta(t) \mid k)), \\ \dot{\vartheta}(t) = \sqrt{\hat{E}_0}\mathrm{cn}(\theta(t) \mid k). \end{cases} \tag{2.29}$$

Finally, the analytical expressions for longitude and drift longitude propagation can be directly obtained exploiting the analytical solution for a swinging pendulum and Equation (2.17):

$$\begin{cases} \theta(t) = \mathrm{sgn}\left(\dot{\vartheta}_0\right) k\Omega\left[t - t_0\right] + \mathrm{sn}^{-1}\left(k_0 \mid \varkappa\right), \\ \lambda(t) = \dfrac{1}{2}\vartheta(t) + \lambda_{1,2} = \arcsin(\mathrm{sn}(\theta(t) \mid \varkappa))\,\mathrm{sgn}(\mathrm{cn}(\theta(t) \mid \varkappa)) + \lambda_{1,2}, \\ \dot{\lambda}(t) = \dfrac{1}{2}\dot{\vartheta}(t) = \dfrac{1}{2}\,\mathrm{sgn}\left(\dot{\vartheta}_0\right)\sqrt{\hat{E}_0}\mathrm{dn}(\theta(t) \mid \varkappa). \end{cases} \tag{2.30}$$

where $\lambda_{1,2}$ is the longitude of the closest gravity well and is defined as $\left(\lambda_{2,2} \pm \frac{\pi}{2}\right)$.

Following Ochs' approach [33], drifting period T can be evaluated as twice of the period of a swinging pendulum:

$$T = 4\varkappa\mathrm{K}(\varkappa)/\Omega \tag{2.31}$$

The amplitude and the period of librating objects can be approximated using the following

formulas derived by Anderson and Schaub [3]:

$$
\begin{cases}
\sin \vartheta_m = \sqrt{\sin^2 \left(\dfrac{\vartheta_0}{2} \right) + \dfrac{\dot{\vartheta_0}^2}{4k^2}}, \\
T = \dfrac{4}{k} \mathrm{K}(\sin \vartheta_m).
\end{cases}
\tag{2.32}
$$

where K is the complete elliptic integral of the first kind and ϑ_m denotes the libration amplitude.

A corrective algorithm is needed to properly retrieve the evolution over time of λ in case of drifting objects. Indeed, Equation (2.30) includes an *arcsin* function which returns values between $-\frac{\pi}{2}$ and $\frac{\pi}{2}$. This implies that modified longitude ϑ must be referred the proper period by comparing time instants with the corresponding drifting period and by checking consistency between sign of initial drift longitude $\dot{\vartheta}_0$ and the variation of the modified longitude.

Algorithm 1 Analytical solution for swinging pendulum

1: $m_{old} = 0$ ▷ Initializing ratio between instant of time and period T
2: $flag = 0$ ▷ Initializing flag variable for period change
3: **for** $i = 1 : N_{instants}$ **do**
4:     $m = floor(t_i/T)$
5:     $\hat{t}_i = mod(t_i/T)$ ▷ Referring to first period
6:     $\vartheta(t_i), \dot{\vartheta}(t_i) \leftarrow$ Eq. (2.28)
7:     **if** $m_{old} \neq m$ **then**
8:        $flag = 0$
9:     **end if**
10:     **if** $\hat{t}_i == 0$ **then**   ▷ t_i is a multiple of period T
11:        $flag = 0$
12:        $\vartheta(t_i) = \vartheta(t_0) + 2\pi \, \mathrm{sgn}(\dot{\vartheta}(t_0)) \cdot m$
13:     **else**   ▷ Checking consistency between sign of initial $\dot{\vartheta}$ and variation of ϑ
14:        **if** $flag == 1$ **or** $\mathrm{sgn}(\dot{\vartheta}(t_0) \neq \mathrm{sgn}(\vartheta(t_i) - \vartheta(t_0))$ **then**
15:           $flag = 1$
16:           $m = m + 1$
17:        **end if**
18:        $\vartheta(t_i) = \vartheta(t_0) + 2\pi \, \mathrm{sgn}(\dot{\vartheta}(t_0)) \cdot m$
19:     **end if**
20:     $m_{old} = floor(t_i/T)$
21: **end for**

2.5.   Performance analytical propagation

To complete the chapter, performances of analytical model are investigated. Comparisons in terms of CPU time and accuracy are therefore performed between analytic approach, numerical model affected by only $J_{2,2}$ harmonic, numerical propagation under $J_{2,2}$ and J_2 effects, and a numerical 3×3 gravitational model. Following simulations are performed with a CPU Intel i7-6700HQ (2.60Ghz) and RAM at 2133 MHz (32Gb).

The solution affected by $J_{2,2}$ harmonic is derived integrating numerically the pendulum-like equation, while the longitudinal evolution under $J_{2,2}$ and J_2 effects is evaluated by applying an integration scheme to Equation (2.7).

Regarding the 3×3 model, the gravitational potential function is retrieved through the spherical harmonics approach introducing the assumption of quasi equatorial orbits [27]:

$$
\begin{aligned}
U(r, \phi, \lambda) = \left(\frac{\mu}{r}\right) & \left[1 - \frac{1}{2}J_2 \left(\frac{R_\oplus}{r}\right)^2 + 3J_{2,2} \left(\frac{R_\oplus}{r}\right)^2 \cos 2\left(\lambda - \lambda_{2,2}\right) \right. \\
& \left. -\frac{3}{2}J_{3,1} \left(\frac{R_\oplus}{r}\right)^3 \cos\left(\lambda - \lambda_{3,1}\right) + 15J_{3,3} \left(\frac{R_\oplus}{r}\right)^3 \cos 3\left(\lambda - \lambda_{3,3}\right) + \frac{3}{8}J_4 \left(\frac{R_\oplus}{r}\right)^4 \right]
\end{aligned}
$$

$$(2.33)$$

where μ is Earth gravitational parameter, r is the geocentric distance from Earth, n and m are respectively degree and order of the harmonics, $R_\oplus$ is Earth's equatorial mean radius, J_n is a n degree zonal harmonic potential, $J_{n,m}$ is a general tesseral harmonic potential and the gravitational coefficients $J_{n,m}$ and $\lambda_{n,m}$ are retrieved from JGM-3 Earth gravitational model (Table 2.2)[27]:

n	m	$J_n \times 10^{-6}$	n	m	$C_{nm} \times 10^{-6}$	$S_{nm} \times 10^{-6}$	$J_{nm} \times 10^{-6}$	$\lambda_{nm}\,(°)$
2	0	-1082.627	2	2	1.574536	-0.903868	1.815528	-14.929
3	0	2.532435	3	1	2.192799	0.2680119	2.2091169	6.968
4	0	1.619331	3	3	0.100559	0.197201	0.2213602	20.994

Table 2.2: JGM-3 Earth gravity model (3×3).

The equations of motion are obtained differentiating Equation (2.33) using spherical co-

ordinates and equating acceleration components to Equation (2.1) [10].

$$
\begin{cases}
\ddot{r} = r\left(\Omega_\oplus + \dot{\lambda}\right)^2 - \dfrac{\mu}{r^2} + \dfrac{3}{2}\mu J_2 \dfrac{R_\oplus^2}{r^4} - 9\mu J_{2,2}\dfrac{R_\oplus^2}{r^4}\cdot\cos 2\left(\lambda - \lambda_{2,2}\right) + \\[2ex]
\quad + 6\mu J_{3,1}\dfrac{R_\oplus^3}{r^5}\cdot\cos\left(\lambda - \lambda_{3,1}\right) - 60\mu J_{3,3}\dfrac{R_\oplus^3}{r^5}\cos 3\left(\lambda - \lambda_{3,3}\right) - \dfrac{15}{8}\mu J_4 \dfrac{R_\oplus^4}{r^6}, \\[2ex]
\ddot{\lambda} = \dfrac{1}{r}\left[-2\dot{r}\left(\Omega_\oplus + \dot{\lambda}\right) - 6\mu J_{2,2}\dfrac{R_\oplus^2}{r^4}\sin 2\left(\lambda - \lambda_{2,2}\right) + \dfrac{3}{2}\mu J_{3,1}\dfrac{R_\oplus^3}{r^5}\sin\left(\lambda - \lambda_{3,1}\right) + \\[2ex]
\quad -45\mu J_{3,3}\dfrac{R_\oplus^3}{r^5}\cdot\sin 3\left(\lambda - \lambda_{3,3}\right)\right].
\end{cases}
\tag{2.34}
$$

Hence, 3×3 solution is computed by integrating numerically Equation (2.34).

Figure 2.7 provides a graphical comparison between the analytical solution and the afore-mentioned numerical methods by setting different energy levels. Figure 2.7a represents the longitudinal evolution of a circulating object (L1) with initial $\Delta a = 20$ km. Conversely, Figure 2.7b and Figure 2.7c predict the longitudinal motion of a drifting object imposing respectively $\Delta a = 200$ km and $\Delta a = 500$ km. Figure 2.7 shows that analytical solution's accuracy tends to shrink by increasing the distance from the perfect geosynchronous orbit and by rising the orbit eccentricity. As the orbit gets away from perfect synchronous one, it is possible to appreciate a growing time delay in the reconstruction of longitudinal behaviour. Therefore, it is possible to conclude that analytical method shall be used to provide, at most, a 2-year prediction of longitudinal evolution for objects orbiting in quasi-circular and quasi-equatorial orbits falling inside the GEO protected region ($|a - a_{GEO}| < 200$ km) or a 1-year prediction for objects with $|a - a_{GEO}| < 500$ km.

In the end, an investigation on computational times is conducted by performing 20 tests for both drifting and librating conditions. ODE113 is adopted as integration scheme to numerically integrate equations of motion of $J_{2,2}$, $J_{2,2}$ and J_2, and 3×3 models. Following results are provided by setting $AbsTol = 1e-6$ and $RelTol = 1e-8$ trading-off between accuracy and the number integration steps. For the sake of completeness, it should be recalled that $AbsTol$ represents an absolute tolerance below which the value of the numerical solution becomes unimportant. If the absolute value of the solution is lower than $AbsTol$, then the solver does not need to provide any correct digits inside the solution. While $RelTol$ computes the error relative to the absolute value of each solution component. Therefore, $RelTol$ allows to modify the number of correct digits inside all solution components, except those smaller than $AbsTol$.
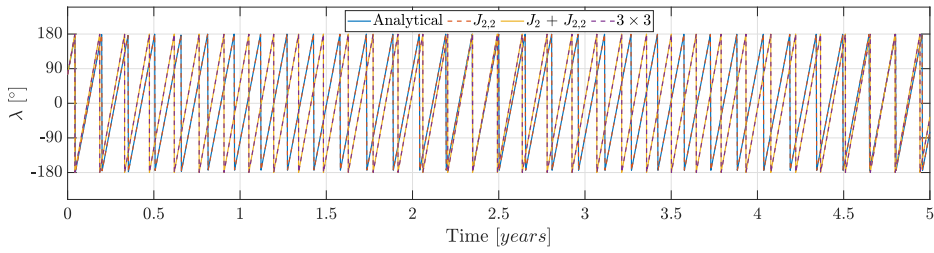
Figure 2.8 highlights that analytical solution enables to reduce significantly the computational time. Indeed, the analytical model is approximately 350 times faster than 3×3 model and 2 times faster than the $J_{2,2}$ numerical model.
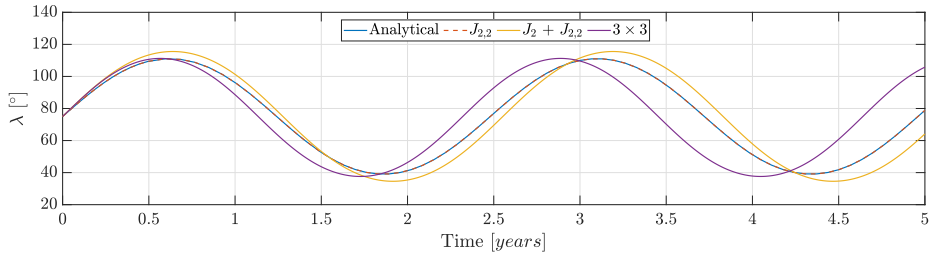
(a) $|a - a_{GEO}| = 20km$.
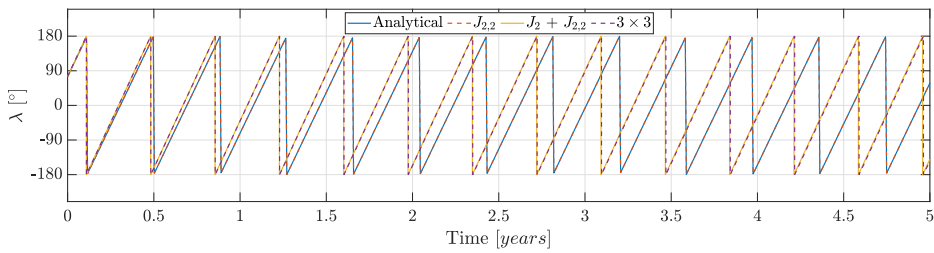
(b) $|a - a_{GEO}| = 200km$.

(c) $|a - a_{GEO}| = 500km$.

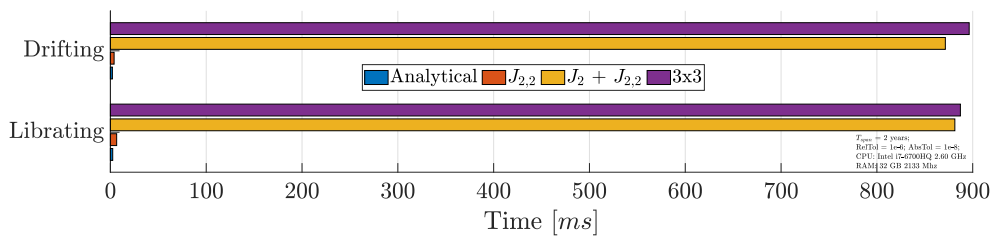Figure 2.7: Longitudinal evolution: comparison between analytical and numerical models.

Figure 2.8: CPU time: comparison between analytical method and numerical models.

3 | Cloud propagation

Once an analytical model for propagation of a single GEO object is derived, it is necessary to develop a strategy to obtain a reliable picture of GEO space debris environment evolution after a fragmentation event.

Current studies on the effects of fragmentations in the geosynchronous regime usually adopt a deterministic approach, propagating individually fragments. Anderson and Schaub [4], for example, implements a piece-wise propagation integrating numerically the two-body equations of motion including 4x4 EGM-96 gravitational model, luni-solar perturbations, and solar radiation pressure (SRP) effects. The adopted 4x4 EGM-96 gravitational model includes aspherical contributions until the fourth order and brings gravitational coefficients form the EGM-96 spherical harmonic model developed by the National Imagery and Mapping Agency (NIMA), the NASA Goddard Space Flight Center (GSFC), and the Ohio State University. The main advantage of this approach consists in implementing a high-fidelity dynamical model and, therefore, obtaining a very accurate prediction of the motion of each fragment. However, as all deterministic methods, this technique is affected by a huge drawback. Computational effort, indeed, is strongly influenced by the number of fragments included inside the simulation. For this reason, Anderson decided to focus its analysis only on objects larger than 0.8 - 1.0 m.

However, as anticipated before, also debris smaller than 1 m represent a potential threat for operational satellites. Thus, the inclusion of small fragments in debris modelling is fundamental to obtain a more complete picture of the debris environment and to avoid underestimating the collisional risk. Hence, deterministic methods are not suitable for modelling the motion of large debris clouds. In this chapter, an efficient method based on the continuum equation is developed to describe the evolution of fragment clouds generated by an explosion or a collision in space. The proposed approach, analogous to the one adopted by Letizia and Colombo [21] for the modeling of debris clouds in the LEO region, consists in considering fragments population as a fluid with continuous properties, whose density changes under the effects of relevant perturbations. Thus, the evolution of fragment density $n(\boldsymbol{x}, t)$ in time t and phase space $\boldsymbol{x}$ can be described by the continuity

equation [21]:

$$\frac{\partial n}{\partial t} + \boldsymbol{\nabla} \cdot (n\boldsymbol{F}) = n^+ - n^- \tag{3.1}$$

with the divergence operator $\boldsymbol{\nabla}\cdot$, source terms n^+, sink terms n^- and the flow defined by the dynamics $\boldsymbol{F}$

$$\frac{\mathrm{d}\boldsymbol{x}}{\mathrm{d}t} = \boldsymbol{F} \tag{3.2}$$

As, in this analysis, all fast and discontinuous events (for example injection of new fragments due to launches and active removal missions,) are neglected, continuity equation becomes [21]:

$$\frac{\partial n}{\partial t} + \boldsymbol{\nabla} \cdot (n\boldsymbol{F}) = 0 \tag{3.3}$$

In particular, Figure 3.1 illustrates the main building blocks characterizing the developed algorithm:

- a break up model that simulate collisions and explosions, given the energy of the fragmentation event;

- an analytical model to propagate fragments piece-wise until the cloud propagation becomes applicable;

- a method to convert orbital parameters of each single fragment into a continuous density function;

- a fully analytical cloud propagator to analyse time evolution of space debris cloud.
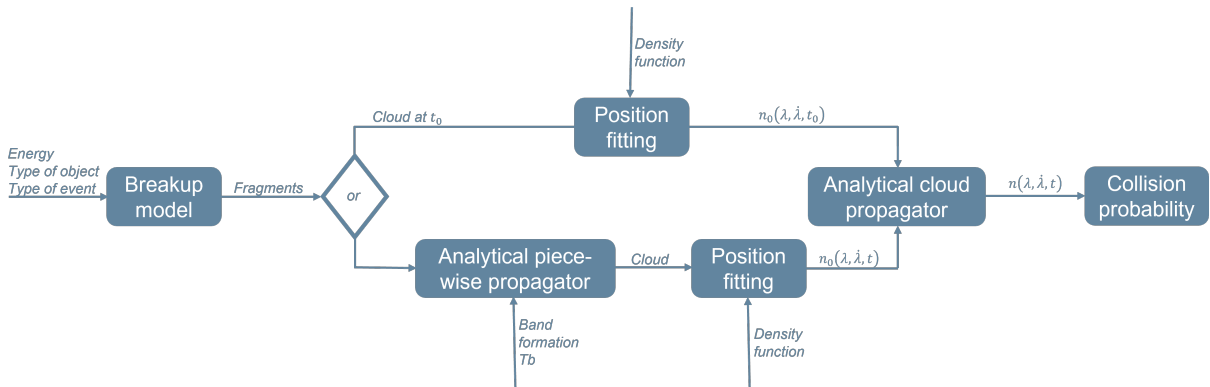
Figure 3.1: Analytical propagator building blocks.

Therefore, this chapter is divided into five main parts. Section 3.1 describes the standard breakup model adopted to simulate fragmentation events. Section 3.2 focuses on the analytical piece-wise propagator and the identification of the main evolutionary phases of a debris cloud. Then, Section 3.3 discusses the derivation of the fully analytical cloud

propagator, while Section 3.4 introduces a method to translate the information about orbital parameters of each single fragment into a continuous density function. In the end, Section 3.5 illustrates an example of application of the cloud propagation.

3.1. Break-up modelling

A breakup model allows to simulate fragmentation events (collisions or explosions) and to describe the distribution of the fragments in terms of characteristic length, area-to-mass ratio and velocity. The dispersion of these parameters depends on the nature of the event (i.e., collision or explosion), type of objects (i.e., rocket body or spacecraft) and the energy involved in the fragmentation event. In this work, fragmentation particles are generated by adopting the NASA Standard Breakup Model, which is an empirical method that adopts the characteristic length L_c of the fragment as independent variable to retrieve main properties of the cloud. Fragment features (i.e., mass, area and velocity) are derived from distribution functions and, therefore, vary at each run of the model even if initial conditions are unaltered. Different distribution functions are used to describe explosions and collisions. Indeed, collisions usually generate a large number of fragments with high relative velocities, while explosions produce larger fragments with lower speed. Moreover, in the NASA SBM, impactor kinetic energy per target mass is used to distinguish between catastrophic and non-catastrophic collisions. In particular, if the threshold value of $\tilde{E}_p^* = 40\,J/g$ is exceeded, the model simulate the complete destruction of the target body [18]. In case of explosions, the cumulative number of fragments N_{frag} does not depend on the mass of the parent body and is computed through the following power law [18]:

$$N_{frag}(d \geq L_c) = 6s \cdot L_c^{-1.6} \tag{3.4}$$

where L_c is the characteristic dimension of the fragments and s is an event-specific calibration constant for historic events and, in this work, is set equal to 1. For collision events, N_{frag} is function of both the fragmentation mass M_c and the relative impact velocity v_c [18]:

$$N_{frag}(d \geq L_c) = 0.1 M_c^{0.75} \cdot L_c^{-1.71} \tag{3.5}$$

where [18]

$$M_c = \begin{cases} m_t + m_p \,[\text{kg}] & \text{for } \tilde{E}_p \geq \tilde{E}_p^* \quad [\text{ catastrophic }] \\ (m_p v_c)\,/1000\,[\text{kg m/s}] & \text{for } \tilde{E}_p < \tilde{E}_p^* \quad [\text{ non-catastrophic }] \end{cases} \tag{3.6}$$

Here, m_t and m_p are respectively the target and impactor masses, while $\tilde{E}_p = \frac{1}{2}\left(\frac{m_p}{m_t}\right)v_c^2$ denotes the specific impact energy.

Fragments area-to-mass ratio are sampled from a bi-modal probability density function [18]:

$$p(\chi, \beta) = \xi(\beta)p_1(\chi) + (1 - \xi(\beta))p_2(\chi), \qquad p_i(\chi) = \frac{1}{\sigma_i\sqrt{2\pi}}\exp\left(-\frac{(\chi - \mu_i)^2}{2\sigma_i^2}\right) \qquad (3.7)$$

where means μ_i, standard deviations σ_i and weighting functions $\xi(\beta)$ depends on effective diameter and type of object. For objects with characteristic dimension $d > 11$cm the NASA model discriminates between fragments from spacecraft and rocket stages, with calibrated quantities $\xi(\beta), \mu_{1,2}(\beta)$, and $\sigma_{1,2}(\beta)$. For spacecraft one gets $\xi \in [0.5, 1.0], \mu_1 \in [-0.9, -0.45], \mu_2 = -0.9, \sigma_1 = 0.55$, and $\sigma_2 \in [0.1, 0.28]$. For orbital stages one finds $\xi \in [0.0, 1.0], \mu_1 \in [-0.95, -0.6], \mu_2 \in [-2.0, -1.2], \sigma_1 \in [0.1, 0.3]$, and $\sigma_2 \in [0.3, 0.5]$. For smaller fragments of $d < 8.0$ cm for spacecraft, and of $d < 1.7$ cm for upper stages, the second term in Equation (3.7) is dropped ($\xi = 1.0$) to generate a single-mode, normal distribution with parameters $\mu_1 \in [-1.0, -0.3]$ and $\sigma_1 \in [0.2, 0.2 + 0.1333(\beta + 3.5)]$. Then, the effective cross sectional area A of each fragment is obtained applying an explicit function of the effective diameter [18]:

$$A\,[\text{m}^2] = \begin{cases} 0.540424(d/[\text{m}])^2 & \text{for } d < 1.67\text{mm} \\ 0.556945(d/[\text{m}])^{2.0047077} & \text{for } d \geq 1.67\text{mm} \end{cases} \qquad (3.8)$$

Fragment mass can be determined from

$$m = \frac{A}{A/m} \qquad (3.9)$$

where A is derived from Equation (3.8), and A/m is statistically sampled via Equation (3.7). While imparted fragmentation velocities Δv_i can be sampled from a normal distribution function. More details regarding the implementation and input parameters of the NASA breakup model can be found in [18].

As proposed by Anderson [3], an upper limit of 1 m and a lower limit of 5 cm are set in the following analysis for the implementation of the NASA break up model.

3.2. Analytical piece-wise propagation

Piece-wise propagation can be used to study individually the time evolution of fragments until the cloud propagation becomes applicable and, also, to investigate the behaviour of a general fragment cloud in the $(\lambda, \dot{\lambda})$ phase space. Specifically, in this work, an analytical piece-wise propagation is adopted by using the analytical solution derived for the nonlinear pendulum like equation. Despite the lower accuracy, the analytical method is preferred to the numerical ones for its reduced computational effort Figure 2.8 and, therefore, its capability of including small fragments inside the simulations.

Once the fragments are generated with the NASA breakup model and their characteristics are defined (i.e., area and mass), position and velocity of each fragment can be derived. At time of fragmentation, all debris are supposed to share the same position on the parent orbit, which corresponds to the location of the fragmentation event. While velocities are computed by summing the corresponding imparted fragmentation velocity Δv_i with the velocity of the parent object at the fragmentation instant. By performing a conversion from Cartesian to Keplerian coordinates, orbital parameters of all the fragments can be determined. In particular, semi-major axis can be evaluated as:

$$a_i = \frac{1}{\frac{2}{r_i} - \frac{v_i^2}{\mu}} \tag{3.10}$$

Then, the fragments can be mapped in $(\lambda, \dot{\lambda})$ phase space and evolution of the cloud can be investigated by propagating individually the debris with Equation (2.30). As shown by Figure 3.3, three main phases can be distinguished during the evolution of a debris cloud. The first phase consists in the generation of debris: fragments share the same longitudinal position but differ in ejection velocity depending on the fragmentation energy distribution (Figure 3.3a). In the second part, the initial dense ellipsoidal cloud is stretched due to the different orbital energy of the fragments (Figure 3.3b). Last phase is characterized by the formation of the fragments band (Figure 3.3c and Figure 3.3d).

In literature some analytical expressions have been proposed to estimate the time required for the band formation in Low-Earth Orbits [30]. All these formulations rely on the hypothesis that apsidal and nodal dispersion is complete when the faster fragment, in terms of apsidal/nodal rate, encounters the slowest one. Analogously, in this analysis, the starting point for the band formation phase is considered to coincide with the time instant at which the faster fragment, in terms of longitudinal drift rate, encounters the slowest one.

Actually, when the fastest particle meets the slowest one, fragments are not still uniformly distributed in λ, meaning that their state cannot be described only as a function of the drift longitude $\dot{\lambda}$ and that this procedure tends to underestimate the required time. Therefore, ad done by Letizia and Colombo [21], a multiplication factor is introduced by applying Kolmogorov-Smirnov test and comparing the debris distribution in λ with a uniform distribution between $-\pi$ and π (Figure 3.2). The band is considered formed at the time when the hypothesis of uniform distribution becomes acceptable. Hence, a multiplication factor $k_b = 2$ is adopted and band formation period can be computed as [8] [20]:

$$T_b = \frac{2\pi \cdot k_b}{\max\left(\dot{\lambda}_f\right) - \min\left(\dot{\lambda}_f\right)} \tag{3.11}$$

where $\dot{\lambda}_f$ are the longitudinal drifts of GEO object generated by the fragmentation event.
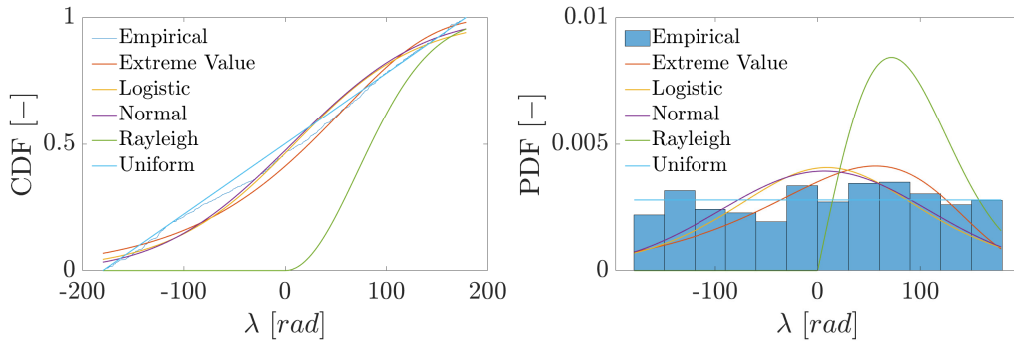
Figure 3.2: Results of Kolmogorov-Smirnov test at band formation T_b.
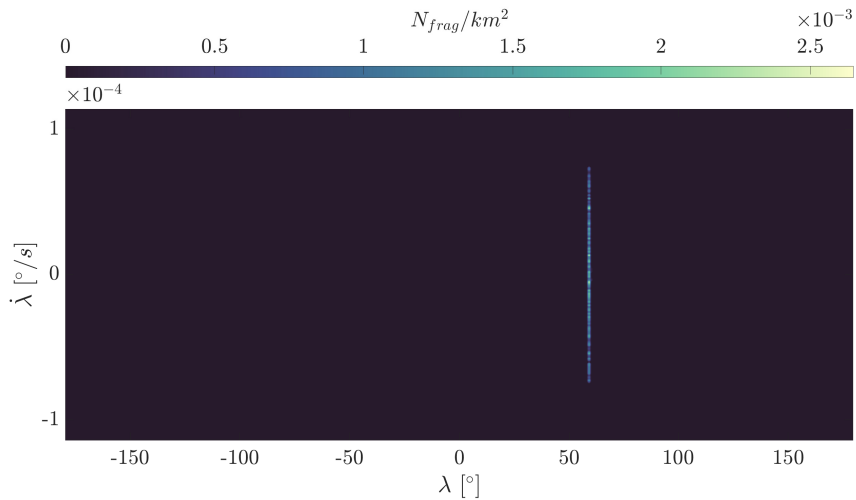
(a) Fragments distribution at instant of fragmentation t_0.

(b) Fragments distribution after $T_b/2$.

(c) Fragments distribution after T_b.

(d) Fragments distribution after $3T_b$.
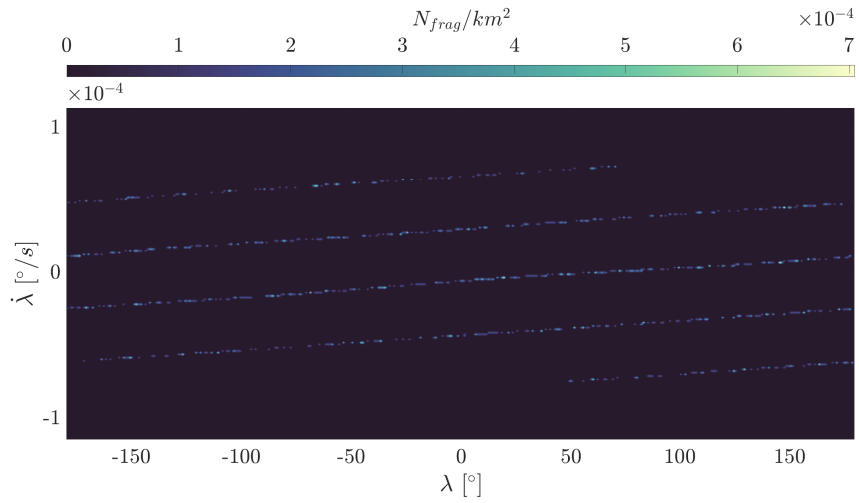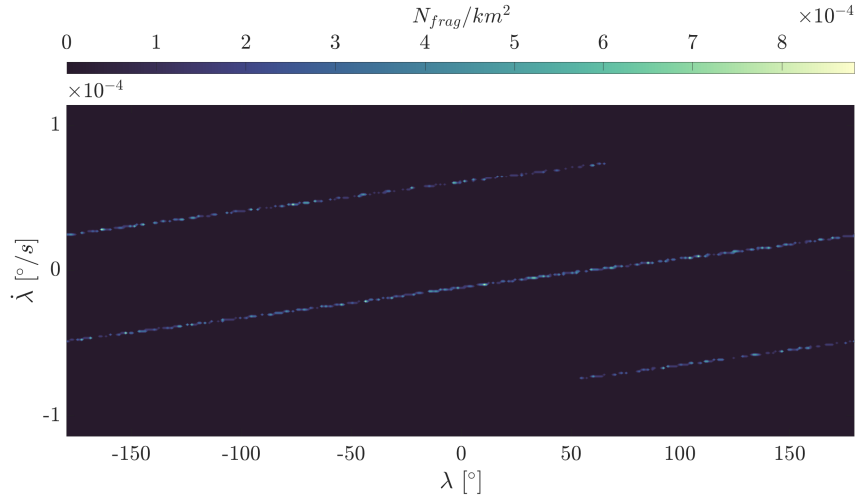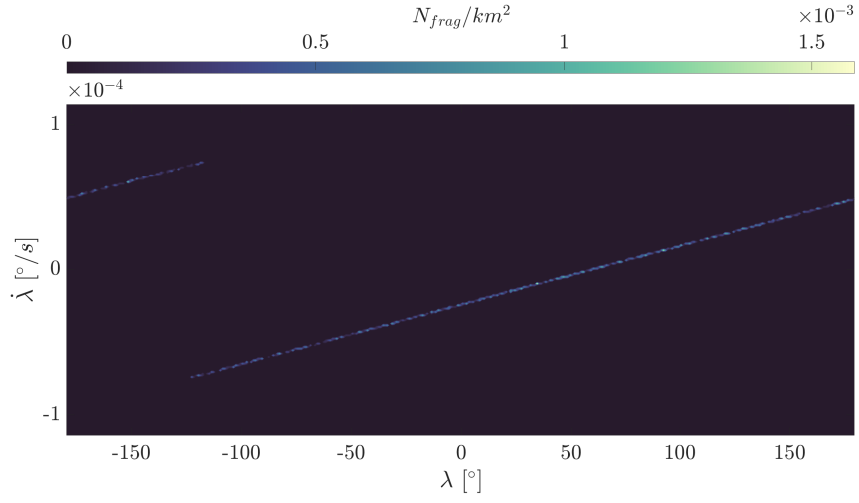
Figure 3.3: Evolutionary phases of debris clouds. Plots obtained simulating a catastrophic collision of a rocket body at $\lambda_0 = 60°$ with $\tilde{E}_p = 77.2 J/g$.

3.3.   Analytical cloud propagation

This section is dedicated to the study carried out to derive the analytical cloud propagator by solving the continuity equation. In particular, this part describes the derivation of the analytical solution of the continuity equation by applying the method of characteristics.

3.3.1.   Solution of continuity equation

The continuity equation is used to derive analytically the density evolution with time under the effect of $J_{2,2}$ perturbation in $(\lambda, \dot{\lambda})$ phase space. Neglecting discontinuous events (all sink and source terms) and expanding the divergence in rectangular coordinates, Equation (3.3) becomes:

$$\frac{\partial n}{\partial t} + v_\lambda \frac{\partial n}{\partial \lambda} + v_{\dot{\lambda}} \frac{\partial n}{\partial \dot{\lambda}} = -n \left[\frac{\partial v_\lambda}{\partial \lambda} + \frac{\partial v_{\dot{\lambda}}}{\partial \dot{\lambda}} \right] \tag{3.12}$$

with

$$\begin{cases} v_\lambda = \dfrac{d\lambda}{dt} = \dot{\lambda}, \\[2mm] v_{\dot{\lambda}} = \dfrac{d\dot{\lambda}}{dt} = 18\Omega_\oplus^2 J_{2,2} \dfrac{R_\oplus^2}{a_{GEO}^2} \sin 2\left(\lambda - \lambda_{2,2} \right). \end{cases} \tag{3.13}$$

Applying the method of characteristics, the partial differential equation in (3.12) can be transformed in the following system of ordinary differential equations:

$$\begin{cases} \dfrac{\mathrm{d}t}{\mathrm{d}\tau} = 1 & \text{(3.14)} \\[3mm] \dfrac{\mathrm{d}\lambda}{\mathrm{d}\tau} = \dot{\lambda} & \text{(3.15)} \\[3mm] \dfrac{\mathrm{d}\dot{\lambda}}{\mathrm{d}\tau} = 18\Omega_\oplus^2 J_{2,2} \dfrac{R_\oplus^2}{a_{GEO}^2} \sin 2\left(\lambda - \lambda_{2,2} \right) & \text{(3.16)} \\[3mm] \dfrac{\mathrm{d}n}{\mathrm{d}\tau} = -n \left[\dfrac{\partial v_\lambda}{\partial \lambda} + \dfrac{\partial v_{\dot{\lambda}}}{\partial \dot{\lambda}} \right] & \text{(3.17)} \end{cases}$$

The expressions of the characteristic lines are retrieved by integrating equations (3.14), (3.15) and (3.16). Exploiting the analytical solution found in Chapter 2, the characteristics equations are described by the following relations:

$$\begin{cases} \theta(t) = \mathrm{sgn}\left(\dot{\lambda}_0\right) k\Omega\left[t - t_0\right] + \mathrm{sn}^{-1}\left(k_0 \mid \varkappa\right), \\ G_\lambda(\lambda, t) = \lambda(t) - \arcsin(\mathrm{sn}(\theta(t) \mid \varkappa))\,\mathrm{sgn}(\mathrm{cn}(\theta(t) \mid \varkappa)) - \lambda_{1,2}, \\ G_{\dot{\lambda}}(\dot{\lambda}, t) = \dot{\lambda}(t) - \dfrac{1}{2}\,\mathrm{sgn}\left(\dot{\lambda}_0\right)\sqrt{\hat{E}_0}\,\mathrm{dn}(\theta(t) \mid \varkappa). \end{cases} \quad (3.18)$$

where

$$\begin{cases} \Omega = 6\,\Omega_\oplus\sqrt{J_{2,2}}\dfrac{R_\oplus}{a_{GEO}}, \\ \hat{E}_0 = \dot{\vartheta}_0^2 + E_p\sin^2\left(\vartheta_0/2\right), \\ E_p = 4\Omega^2, \\ k = \sqrt{\hat{E}_0/E_p}, \\ \varkappa = 1/k. \end{cases} \quad (3.19)$$

and k_0^2 is the ratio between initial potential energy and E_p.

From Equation (3.13), it is possible to observe that

$$\frac{\partial v_\lambda}{\partial \lambda} = \frac{\partial v_{\dot{\lambda}}}{\partial \dot{\lambda}} = 0 \quad (3.20)$$

and, thus, that Equation (3.17) describes a simple translation of the domain of the initial conditions. This means that λ and $\dot{\lambda}$ are canonical variables of the problem and that the explicit expression for the density evolution in time results to be:

$$n\left(\lambda, \dot{\lambda}, t\right) = n_0\left(\tilde{\lambda}, \tilde{\dot{\lambda}}, t_0\right) \quad (3.21)$$

where n_0 is the initial fragment distribution and $\tilde{\lambda}, \tilde{\dot{\lambda}}$ are obtained by inverting the characteristics at the initial time. Methods for determining n_0 will be presented in the following section, while expressions of $\tilde{\lambda}, \tilde{\dot{\lambda}}$ are computed below.

Following the approach proposed by Letizia [25], characteristic curves can be re-written as:

$$\begin{cases} G_\lambda(\lambda, t) = f_\lambda(\lambda) + g_\lambda(t) \\ G_{\dot{\lambda}}(\dot{\lambda}, t) = f_{\dot{\lambda}}(\dot{\lambda}) + g_{\dot{\lambda}}(t). \end{cases} \quad (3.22)$$

with functions $f_\lambda(\lambda)$ and $f_{\dot{\lambda}}(\dot{\lambda})$ equal to:

$$\begin{cases} f_\lambda(\lambda) = G_\lambda(\lambda, t = 0) - g_\lambda(t = 0) = \lambda - \lambda_0 \\ f_{\dot\lambda}(\dot\lambda) = G_{\dot\lambda}(\dot\lambda, t = 0) - g_{\dot\lambda}(t = 0) = \dot\lambda - \dot\lambda_0. \end{cases} \tag{3.23}$$

Therefore, $\tilde\lambda, \tilde{\dot\lambda}$ can be evaluated as:

$$\begin{cases} \tilde\lambda = f_\lambda^{-1}\left(G_\lambda(\lambda, t)\right) = G_\lambda(\lambda, t) + \lambda_0 \\ \tilde{\dot\lambda} = f_{\dot\lambda}^{-1}\left(G_{\dot\lambda}(\dot\lambda, t)\right) = G_{\dot\lambda} + \dot\lambda_0. \end{cases} \tag{3.24}$$

Recalling Equation (3.18) and that $\tilde\lambda = \lambda_0$ and $\tilde{\dot\lambda} = \dot\lambda_0$, the following system of equations should be solved:

$$\begin{cases} \tilde\theta(t) = \mathrm{sgn}\left(\tilde{\dot\lambda}\right) \tilde k \Omega\left[t - t_0\right] + \mathrm{sn}^{-1}\left(\sin(\tilde\lambda - \lambda_{1,2}) \mid \tilde\varkappa\right), \\ \lambda(t) - \arcsin(\mathrm{sn}(\tilde\theta \mid \tilde\varkappa))\,\mathrm{sgn}(\mathrm{cn}(\tilde\theta \mid \tilde\varkappa)) - \lambda_{1,2} = 0, \\ \dot\lambda(t) - \dfrac{1}{2}\,\mathrm{sgn}\left(\tilde{\dot\lambda}\right)\sqrt{\tilde{\hat E}}\,\mathrm{dn}(\tilde\theta \mid \tilde\varkappa) = 0. \end{cases} \tag{3.25}$$

The system (3.25) cannot be solved analytically and, thus, an alternative approach for the computation of $\tilde\lambda$ and $\tilde{\dot\lambda}$ must be found. A solution could be provided by an iterative zero-finding method; however, this solution would result in a huge rise of the computational effort, strongly affecting one of the main advantages of this analytical procedure. Therefore, instead solving a zero-finding problem, it is decided to perform a backward propagation in time in order to retrieve $\tilde\lambda$ and $\tilde{\dot\lambda}$ by using the analytical solution derived in previous chapter (2.30). Hence, setting the initial conditions $\lambda_0 = \lambda$ and $\dot\lambda_0 = \dot\lambda$ and propagation time $\Delta t = t_0 - t$, $\tilde\lambda$ and $\tilde{\dot\lambda}$ can be evaluated without the need of numerical or iterative methods.

$$\begin{cases} \theta(t) = \mathrm{sgn}\left(\dot\vartheta_0\right) k\Omega\left[t_0 - t\right] + \mathrm{sn}^{-1}\left(k_0 \mid \varkappa\right), \\ \tilde\lambda(t) = \dfrac{1}{2}\vartheta(t) + \lambda_{1,2} = \arcsin(\mathrm{sn}(\theta(t) \mid \varkappa))\,\mathrm{sgn}(\mathrm{cn}(\theta(t) \mid \varkappa)) + \lambda_{1,2}, \\ \tilde{\dot\lambda}(t) = \dfrac{1}{2}\dot\vartheta(t) = \dfrac{1}{2}\,\mathrm{sgn}\left(\dot\vartheta_0\right)\sqrt{\hat E_0}\,\mathrm{dn}(\theta(t) \mid \varkappa). \end{cases} \tag{3.26}$$

Similarly to the procedure adopted in Section 2.4, a corrective algorithm must be implemented to evaluate correctly the output of *arcsin* function during backward propagation. Thus, the following algorithm is developed to solve the pendulum-like equation.

Algorithm 2 Analytical solution for swinging pendulum for backward propagation

1:   $m_{old} = 0$ ▷ Initializing ratio between instant of time and period T
2:   $flag = 0$ ▷ Initializing flag variable for period change
3:   **for** $i = 1 : N_{instants}$ **do**
4:      $m = ceil(t_i/T)$
5:      $\hat{t}_i = -mod(|t_i|/T)$ ▷ Referring to first period
6:      $\vartheta(t_i), \dot{\vartheta}(t_i) \leftarrow$ Eq. (2.28)
7:      **if** $m_{old} \neq m$ **then**
8:        $flag = 0$
9:      **end if**
10:     **if** $\hat{t}_i == 0$ **then**   ▷ t_i is a multiple of period T
11:        $flag = 0$
12:        $\vartheta(t_i) = \vartheta(t_0) + 2\pi \, \text{sgn}(\dot{\vartheta}(t_0)) \cdot m$
13:     **else**   ▷ Checking consistency between sign of initial $\dot{\vartheta}$ and variation of ϑ
14:        **if** $flag == 1$ **or** $\text{sgn}(\dot{\vartheta}(t_0) == \text{sgn}(\vartheta(t_i) - \vartheta(t_0))$ **then**
15:          $flag = 1$
16:          $m = m - 1$
17:        **end if**
18:        $\vartheta(t_i) = \vartheta(t_0) + 2\pi \, \text{sgn}(\dot{\vartheta}(t_0)) \cdot m$
19:     **end if**
20:     $m_{old} = ceil(t_i/T)$
21: **end for**

It is important to highlight that probabilistic propagation of initial density using the method of characteristics allows to exactly evaluate fragment density along the characteristic lines. However, density cannot be estimated outside the characteristic curves, meaning that backward propagation should be employed for each point of interest. Equations (3.18) shows that the trajectory of the characteristic lines does not depend on density. Hence, a single backward propagation would suffice to evaluate debris density at a specific location and a fixed epoch.

However, if the density estimation is needed over the entire domain, many backward propagations have to be performed. The selected grid should be denser in correspondence of phase space regions that exhibit the highest density gradients; but these regions cannot be foreseen easily due to the complexity of the dynamical problem. Hence, in this work, a quite dense regular grid is adopted.

The limit in the performance of the developed cloud propagator is in the the analytical

solution used to invert the characteristic lines. To grant an accurate evaluation of $\tilde{\lambda}$ and $\dot{\tilde{\lambda}}$, only fragments with $|a - a_{GEO}| < 500km$ are included inside the simulations. Moreover, during the derivation of the analytical solution in Chapter 2, both $(\phi \approx 0)$ and $(r \approx a_{GEO})$ approximations have been introduced, meaning that orbits of debris are considered quasi-circular and quasi-equatorial.

3.4. Position fitting

The NASA breakup model gives as output information about each single fragment in the $(\lambda, \dot{\lambda})$ phase space. That information are used to define the continuous density function (especially at the initial condition n_0), with which to study the evolution over time using the cloud propagation. This section presents three different approaches for the sampling of the initial conditions.

3.4.1. Binning method

The first method consists in discretising the domain by applying a regular grid in λ and $\dot{\lambda}$ and estimating initial density by counting fragments falling inside each grid cell at t_0:

$$n_0^{(i,j)} = \frac{N_{frag}^{(i,j)}}{A_{cell}} = \frac{N_{frag}^{(i,j)}}{\Delta\lambda \cdot \Delta\dot{\lambda}} \qquad [\#s/rad^2] \qquad (3.27)$$

A two-dimensional spatial density $\hat{n}_0$ can be evaluated by converting $\Delta\lambda$ and $\Delta\dot{\lambda}$ into spatial distances. Recalling Equation (2.15) $\Delta\dot{\lambda}$ can be transformed into:

$$\Delta a = \frac{2a_{GEO}}{3\Omega_\oplus}\Delta\dot{\lambda} \qquad (3.28)$$

while, introducing the hypothesis of quasi perfect geosynchronous orbits ($a \approx a_{GEO}$ and circular orbits, angular distance $\Delta\lambda$ is converted into:

$$\Delta l = a_{GEO} \cdot \Delta\lambda \qquad (3.29)$$

Therefore, the two-dimensional spatial density $\hat{n}_0$ becomes:

$$\hat{n}_0^{(i,j)} = \frac{N_{frag}^{(i,j)}}{\Delta l \Delta a} = \frac{N_{frag}^{(i,j)}}{\Delta\lambda\Delta\dot{\lambda}} \cdot \frac{3\Omega_\oplus}{2a_{GEO}^2} \qquad [\#/km^2] \qquad (3.30)$$

where indexes (i, j) identify a specific cell and $\Delta\dot{\lambda}$ and $\Delta\lambda$ are the sizes of each bin.

Inside each cell, the density is considered constant and, thus, function n_0 is characterized

by multiple jump discontinuities. Therefore, a linear interpolation scheme is applied to the density distribution to obtain a continuous density function.

Several simulations have been carried out by varying the sampling grid and running multiple times the NASA Breakup Model with fixed initial conditions. These tests demonstrated that this approach is characterized by two main drawbacks. On the one hand, n_0 estimation depends strongly on dimensions of the bins. Figure 3.4 shows that density tend to increase by adopting a denser a grid. Particularly, it is possible to highlight that density can change even of an order of magnitude.
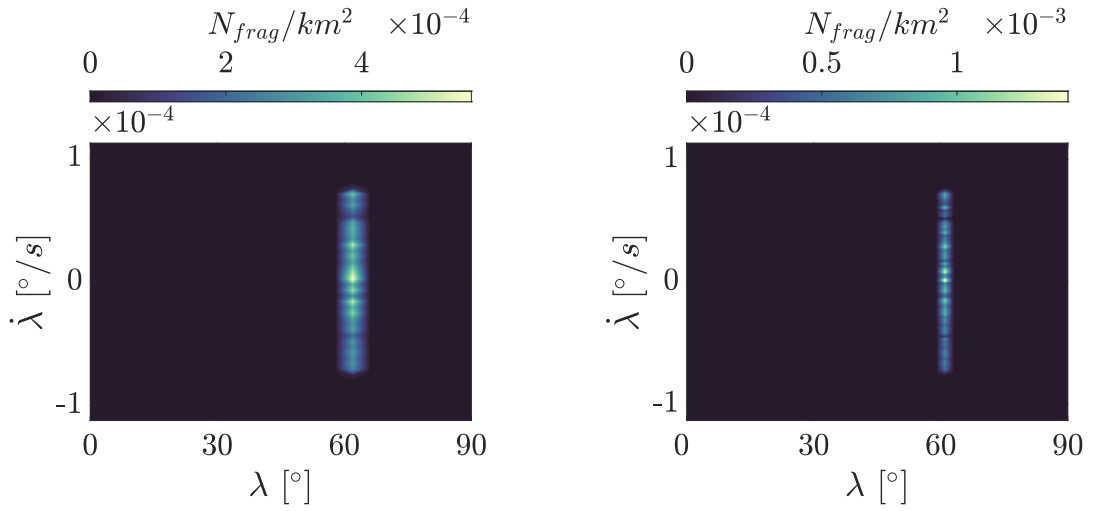
(a) Position fitting with binning method. Grid made by 4500 cells.

(b) Position fitting with binning method. Grid made by 18000 cells.
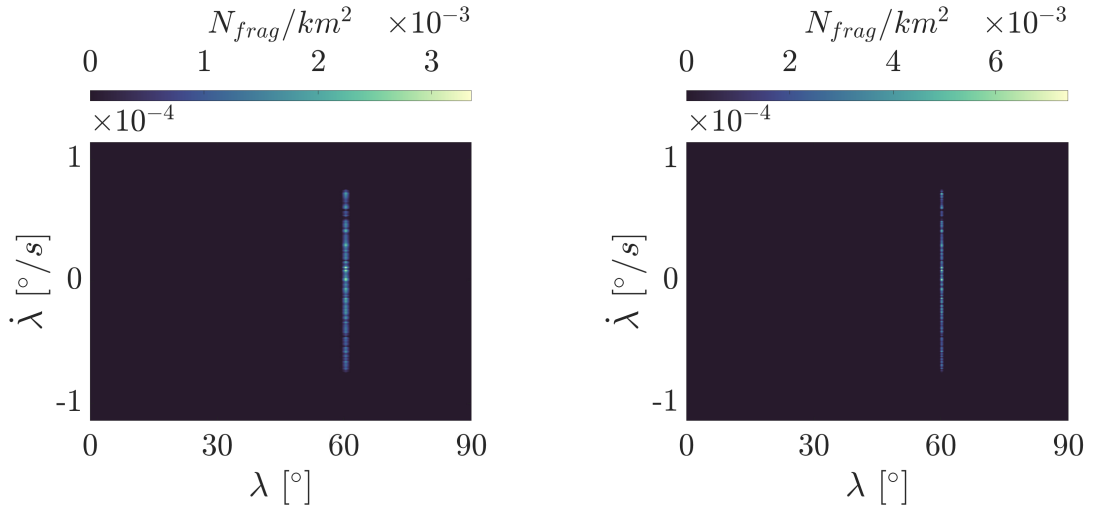
(c) Position fitting with binning method. Grid made by 72000 cells.

(d) Position fitting with binning method. Grid made by 216000 cells.

Figure 3.4: Applications of binning method. Grid comparison simulating a catastrophic collision of a rocket body at $\lambda_0 = 60°$ with $\tilde{E}_p = 77.2 J/g$.

On the other hand, results of this method can vary significantly at each run of the NASA Breakup Model. Characteristics of the fragments are obtained sampling probability distribution functions; thus, energy distribution among fragments can vary significantly at each run of the NASA breakup model. As depicted by Figure 3.5, binning method simply counts the number of fragments falling inside each bin, leading to a high sensitivity to the single run of NASA SBM. Figure 3.5 illustrates that density distribution can experiment even variations of 15% in the maximum density value.
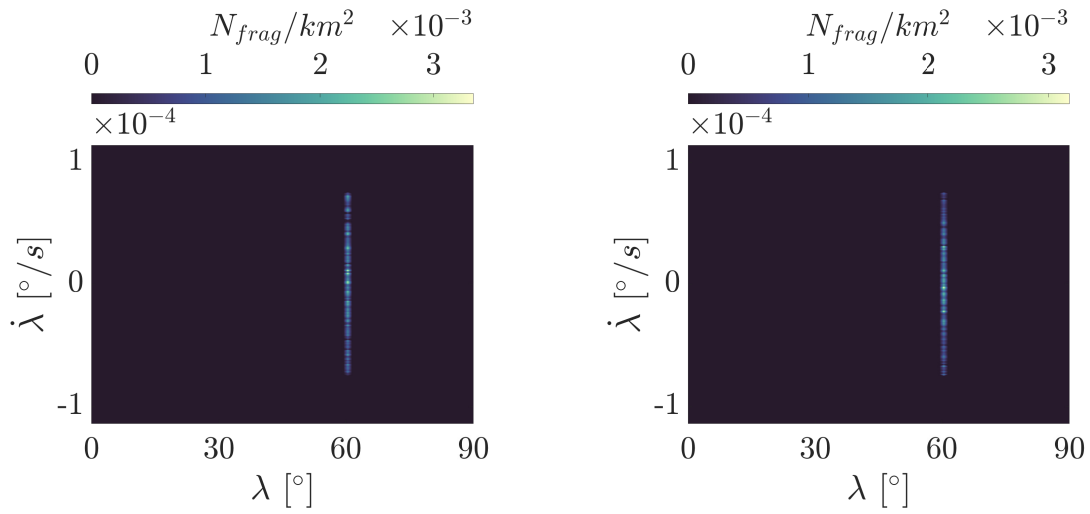
(a) Position fitting with binning method. Fist run of NASA SBM.

(b) Position fitting with binning method. Second run of NASA SBM.
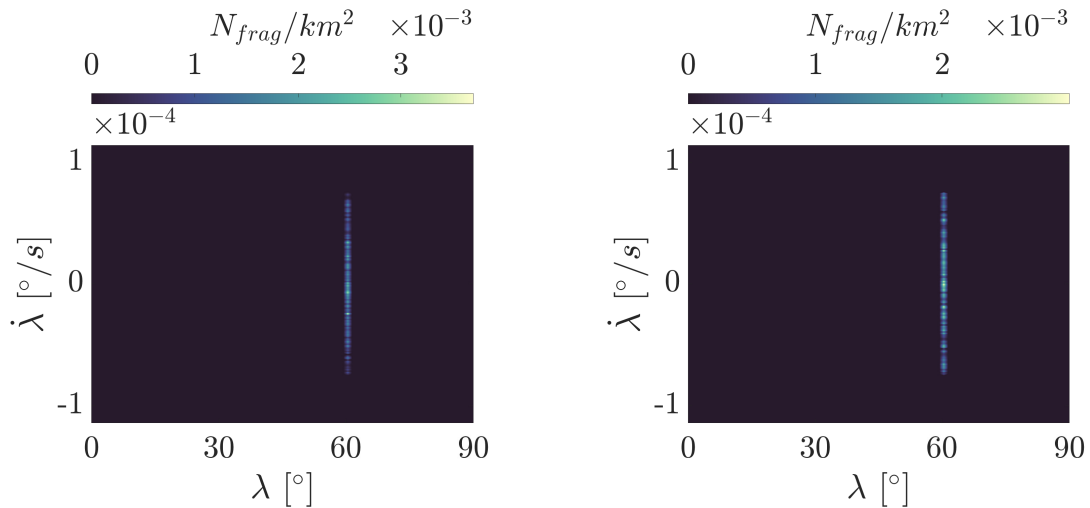
(c) Position fitting with binning method. Third run of NASA SBM.

(d) Position fitting with binning method. Fourth run of NASA SBM.

Figure 3.5: Applications of binning method. Comparison of different runs of NASA SBM simulating a catastrophic collision of a rocket body at $\lambda_0 = 60°$ with $\tilde{E}_p = 77.2 J/g$.

To overcome the first issue, the variation of fragments distribution is analysed as function of bin dimensions. The fragments are generated with the same run of the NASA breakup model and then, grids with different bin dimensions are applied to the initial debris distribution (Figure 3.6). Results of this test illustrate that fragments distribution tends to converge by rising the number of bins used to discretise the domain.

In this work, a grid of 72000 bins is selected ($\Delta\dot\lambda = 1.146 \cdot 10^{-6}\,°/s$ and $\Delta\lambda = 1°$) to grant a sufficient level of convergence, to limit computational effort and to limit the dependence on the specific run of the NASA breakup model.
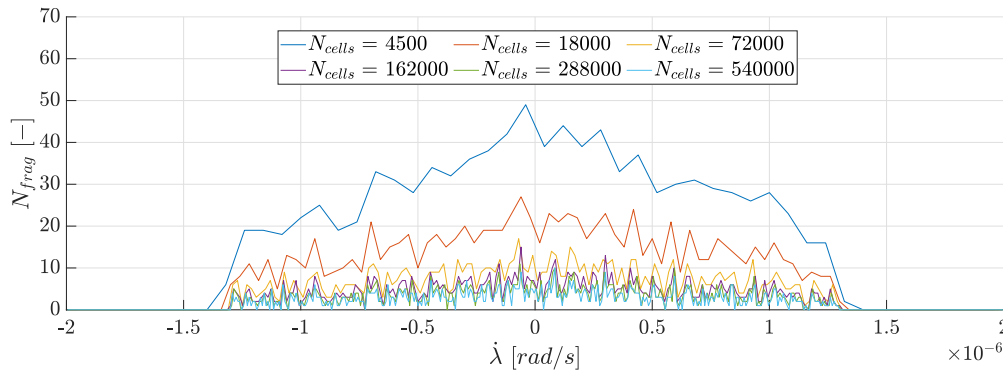
Figure 3.6: Fragments distribution as function of bin dimensions. Analysis performed simulating a catastrophic collision of a rocket body at $\lambda_0 = 60°$ with $\tilde{E}_p = 77.2\,J/g$.

3.4.2. 1-D Probability Distribution Function approach

The second method consists in approximating fragment density at fragmentation eposch t_0 with a standard probability distribution function. The distribution in λ is simply described by a Dirac delta function, while a Kolmogorov-Smirnov test is performed to identify the PDF that best reconstruct the density distribution in $\dot\lambda$. In particular, the Kolmogorov-Smirnov statistic has been used to measure the maximum distance between the empirical cumulative distribution function of the simulation data and the cumulative distribution function used to fit them.

By simulating several fragmentation events, the Kolmogorov-Smirnov test shows that normal distribution function is able to approximate quite precisely the initial fragments distribution. To prove this assumption, a catastrophic collision of a rocket body at $\lambda_0 = 60°$ with $\tilde{E}_p = 77.2\,J/g$ is simulated. The Kolmogorov-Smirnov statistics are collected in Table 3.1. For the sake of completeness, a graphical comparison between the empirical fragments distribution and some standard distribution functions (extreme value, logistic, normal, Rayleigh and uniform distributions) can be found in Figure 3.11.

Standard Distribution	$KS_{\dot{\lambda}}$
Extreme value	0.0741
Logistic	0.2143
Normal	0.0408
Rayleigh	0.5443
Uniform	0.0660

Table 3.1: Value of the Kolmogorov-Smirnov statistic for the tested distribution functions.
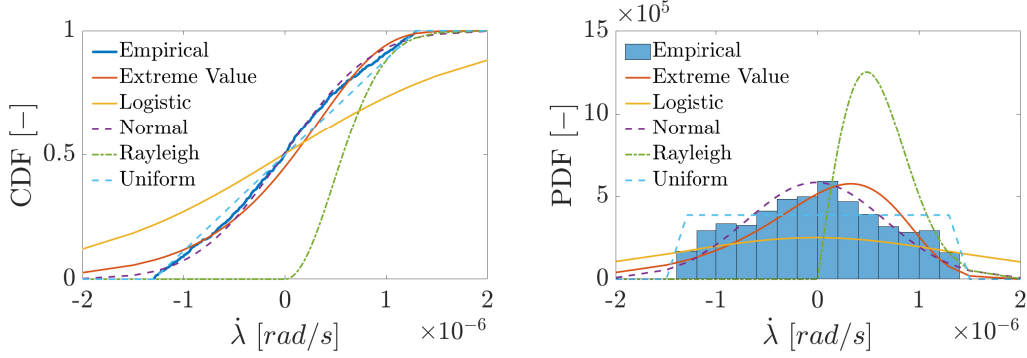

Figure 3.7: Comparison between empirical fragments distribution and some standard distribution functions.

The initial fragment density can be computed as:

$$n_0(\lambda, \dot{\lambda}, t_0) = \delta\left(\lambda - \lambda_0\right) \cdot \frac{N_{frag}}{\sigma_f \sqrt{2\pi}} \exp\left(-\frac{\left(\dot{\lambda} - \mu_f\right)^2}{2\sigma_f^2}\right) \qquad [\#s/rad^2] \quad (3.31)$$

$$\hat{n}_0(\lambda, \dot{\lambda}, t_0) = \frac{3\Omega_\oplus}{2a_{GEO}} \cdot \delta\left(\lambda - \lambda_0\right) \cdot \frac{N_{frag}}{\sigma_f \sqrt{2\pi}} \exp\left(-\frac{\left(\dot{\lambda} - \mu_f\right)^2}{2\sigma_f^2}\right) \qquad [\#/km^2] \quad (3.32)$$

Here, δ is the Dirac delta function, λ_0 represents the location of the fragmentation event, μ_f is the mean value of fragments longitudinal drift and σ_f is the standard deviation of fragments distribution in $\dot{\lambda}$. However, we should highlight that Dirac delta function cannot be implemented as:

$$\delta\left(\lambda - \lambda_0\right) = \begin{cases} 1 & \text{for } \lambda \equiv \lambda_0 \\ 0 & \text{for } \lambda \neq \lambda_0 \end{cases} \qquad (3.33)$$

otherwise, during the backward propagation, density will result always equal to zero. Therefore, in this work, Dirac delta function is replaced by the following expression:

$$\delta\left(\lambda - \lambda_0\right) = double\left(|\lambda - \lambda_0| <= \frac{\Delta\lambda}{2}\right) \qquad (3.34)$$

where $\Delta\lambda$ represents the longitudinal spacing of the grid used to estimate debris density over the entire domain during the cloud propagation.

As for the binning approach, potential advantages or disadvantages of this method are investigated for the 1-D PDF method. Thus, fitting is performed by considering different run of the NASA Break-up Model and different grid spacing. On the one hand, Figure 3.9 shows that the implemented 1-D PDF approach is less sensitive to the NASA SBM with respect to the binning approach. Indeed, density profile seems to be unaltered by varying the NASA SBM run and density peak has registered a maximum variation of 5%.
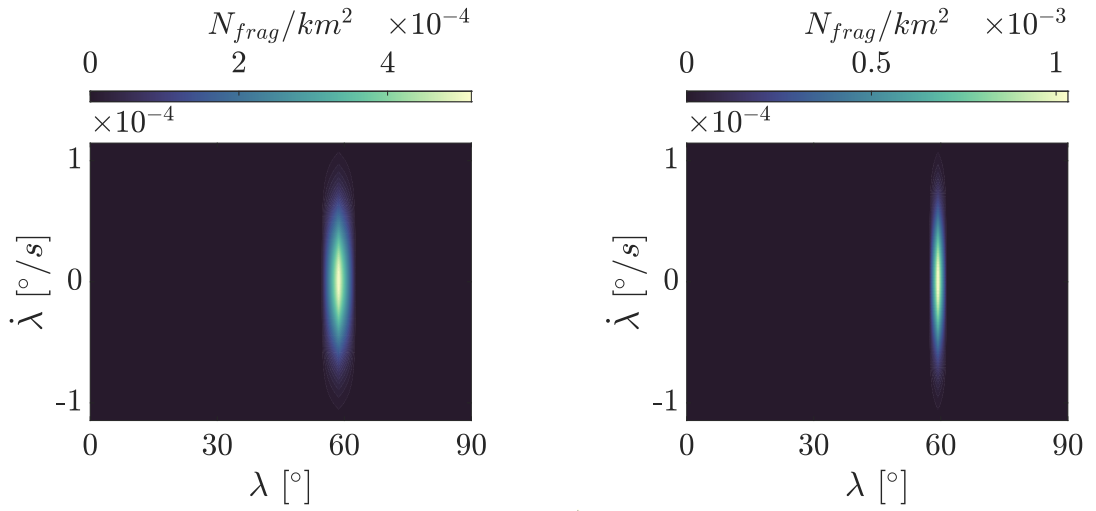
(a) Position fitting with 1-D PDF method. Grid made by 4500 cells.

(b) Position fitting with 1-D PDF method. Grid made by 18000 cells.
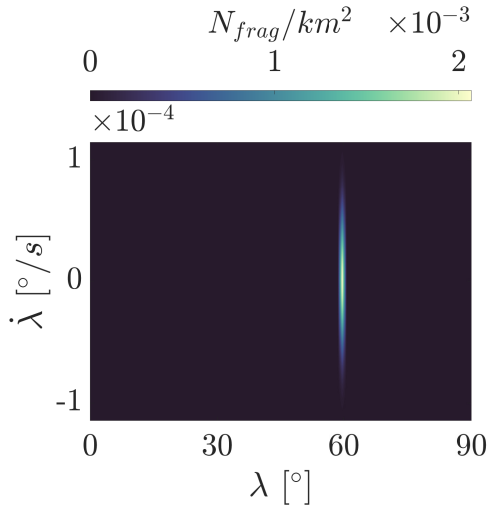
(c) Position fitting with 1-D PDF method. Grid made by 72000 cells.

(d) Position fitting with 1-D PDF method. Grid made by 216000 cells.

Figure 3.8: Applications of 1-D Probability Distribution Function method. Grid comparison simulating a catastrophic collision of a rocket body at $\lambda_0 = 60°$ with $\tilde{E}_p = 77.2 J/g$.

On the other hand, this method exhibits the same limit of the binning approach: initial density distribution depends significantly on the grid adopted to discretise the domain. Figure 3.8 shows that, even in this case, debris density tends to significantly decrease by using a coarser grid. This fact is provoked by the chosen implementation of Dirac delta function. Indeed, Equation (3.33) depends directly by the adopted longitudinal grid spacing.
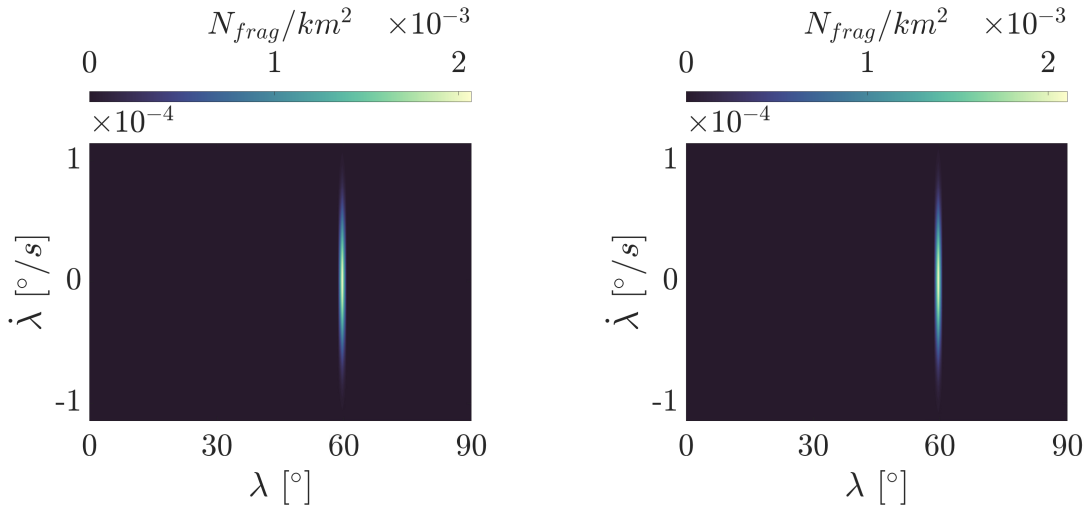
(a) Position fitting with 1-D PDF method. Fist run of NASA SBM.

(b) Position fitting with 1-D PDF method. Second run of NASA SBM.
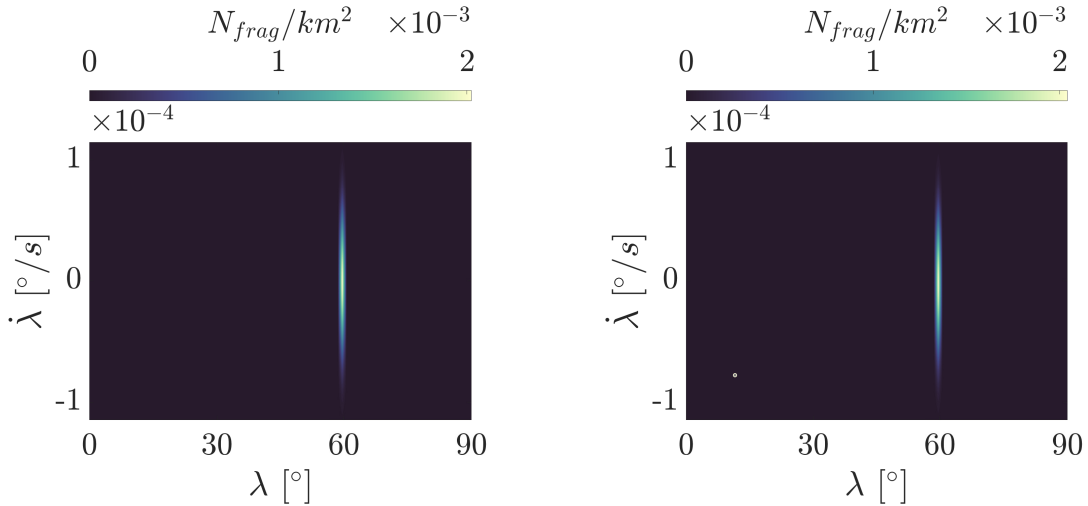
(c) Position fitting with 1-D PDF method. Third run of NASA SBM.

(d) Position fitting with 1-D PDF method. Fourth run of NASA SBM.

Figure 3.9: Applications of 1-D PDF method. Comparison of different runs of NASA SBM simulating a catastrophic collision of a rocket body at $\lambda_0 = 60°$ with $\tilde{E}_p = 77.2 J/g$.

3.4.3.   2-D Probability Distribution Function approach

The first two methods depend strongly on the sampling grid used to study the cloud evolution. Therefore, a third approach able to avoid this issue is resented here. The method consists in propagating individually each fragment with the analytical propagator and, then, approximating the fragment density with a bi-dimensional standard probability distribution function. Analogously to the procedure presented before, a Kolmorov-Smirnov test is performed to identify the PDF that best reconstruct density distribution in λ and $\dot{\lambda}$.

As proposed by Letizia and Colombo [20], the piece-wise propagation is performed once the band is considered formed and, thus, initial debris density is estimated at T_b. As explained previously in Section 3.2, band is considered formed when the hypothesis of uniform distribution in λ becomes acceptable and, thus, fragments state can be described only as a function of the drift longitude $\dot{\lambda}$. Hence, λ and $\dot{\lambda}$ are assumed to be statistically independent variables and debris density can be computed as:

$$n_0(\lambda, \dot{\lambda}, t_0) = p_\lambda \cdot p_{\dot{\lambda}} \tag{3.35}$$

where $p_{\dot{\lambda}}$ is the probability distribution function that best reconstruct the density distribution in $\dot{\lambda}$ and p_λ represents the uniform distribution in λ:

$$p_\lambda = \frac{1}{2\pi} \tag{3.36}$$

After several simulations, Kolmogorov-Smirnov test suggests us that the normal distribution function is the one that better fits the fragments distribution in $\dot{\lambda}$. Therefore, the initial fragment density can be computed as:

$$n_0(\lambda, \dot{\lambda}, t_0) = \frac{1}{2\pi} \cdot \frac{N_{frag}}{\sigma_f \sqrt{2\pi}} \exp\left(-\frac{\left(\dot{\lambda} - \mu_f\right)^2}{2\sigma_f^2}\right) \qquad [\#s/rad^2] \tag{3.37}$$

$$\hat{n}_0(\lambda, \dot{\lambda}, t_0) = \frac{3\Omega_\oplus}{2a_{GEO}} \cdot \frac{1}{2\pi} \cdot \frac{N_{frag}}{\sigma_f \sqrt{2\pi}} \exp\left(-\frac{\left(\dot{\lambda} - \mu_f\right)^2}{2\sigma_f^2}\right) \qquad [\#/km^2] \tag{3.38}$$

However, this strategy is affected by a huge issue. Comparing the density distribution derived with a binning method and one retrieved with the 2-D PDF approach at T_b, it is possible to highlight that the assumption of statistically independent variables does not hold for this problem. Indeed, simulating a catastrophic collision of a rocket body at

$\lambda_0 = 60°$ with $\tilde{E}_p = 77.2 J/g$, 2-D PDF method wrongly estimates the debris distribution predicting, also, a non-null fragment density close to (L2) gravitational well (Figure 3.10).

(a) Position fitting with binning method at T_b. Grid made by 72000 cells.
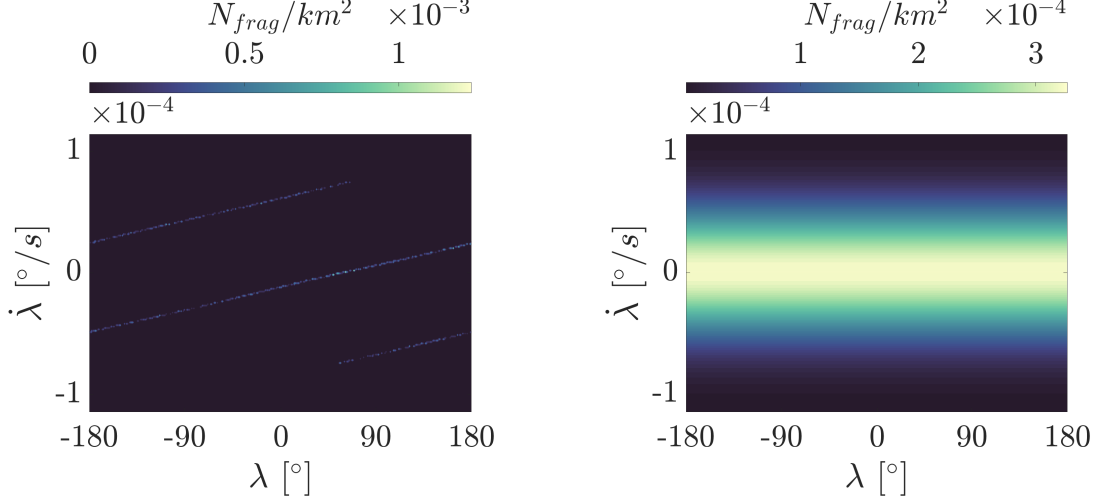
(b) Position fitting with 2-D PDF method at T_b. Grid made by 72000 cells.

Figure 3.10: Comparison between 2-D PDF and binning methods at T_b. Simulation of a catastrophic collision of a rocket body at $\lambda_0 = 60°$ with $\tilde{E}_p = 77.2 J/g$.

Hence, instead of computing the density distribution at T_b, it is decided to evaluate n_0 well before the band formation. Particularly, in this work, initial debris distribution is investigated at about a quarter of the band formation period $(t_0 + T_b/4)$. After several simulations and applications of the Kolmogorov-Smirnov test, the multivariate normal distribution function resulted to be the bi-dimensional PDF that better fits the fragments distribution at $t_0 + T_b/4$ both in terms of longitude and longitudinal drift. Hence, initial fragment density is evaluated as:

$$
\begin{cases}
n_0\left(\lambda, \dot{\lambda}\right) = \dfrac{N_{frag}}{2\pi\sigma_\lambda\sigma_{\dot{\lambda}}\sqrt{1-\rho^2}} \exp\left[-\dfrac{z}{2\left(1-\rho^2\right)}\right] & [\#s/rad^2] \\[3mm]
z \equiv \dfrac{(\lambda-\mu_\lambda)^2}{\sigma_\lambda^2} - \dfrac{2\rho\left(\lambda-\mu_\lambda\right)\left(\dot{\lambda}-\mu_{\dot{\lambda}}\right)}{\sigma_\lambda\sigma_{\dot{\lambda}}} + \dfrac{\left(\dot{\lambda}-\mu_{\dot{\lambda}}\right)^2}{\sigma_{\dot{\lambda}}^2} \\[3mm]
\rho \equiv \mathrm{cor}\left(\lambda, \dot{\lambda}\right) = \dfrac{V_{\lambda,\dot{\lambda}}}{\sigma_\lambda\sigma_{\dot{\lambda}}} \\[3mm]
\hat{n}_0 = n_0 \cdot \dfrac{3\Omega_\oplus}{2a_{GEO}^2} & [\#/km^2]
\end{cases}
\tag{3.39}
$$

where ρ is the correlation of λ and $\dot{\lambda}$, $V_{\lambda,\dot{\lambda}}$ is the covariance and σ_λ and $\sigma_{\dot{\lambda}}$ are the variance

of fragments longitudes and longitudinal drifts respectively at about a quarter of the band formation period. Again, a catastrophic collision of a rocket body at $\lambda_0 = 60°$ with $\tilde{E}_p = 77.2 J/g$ is used to perform the simulations and the results of the Kolmorov-Smirnov test are reported in Figure 3.7 and Table 3.2.

Standard Distribution	KS_λ	$KS_{\dot\lambda}$
Extreme value	0.0713	0.0714
Logistic	0.0471	0.2167
Normal	0.0465	0.0475
Rayleigh	0.1904	0.5225
Uniform	0.0522	0.0518

Table 3.2: Kolmogorov-Smirnov statistic for some standard distribution functions.

(a) Distribution in longitude.

(b) Distribution in drift longitude.
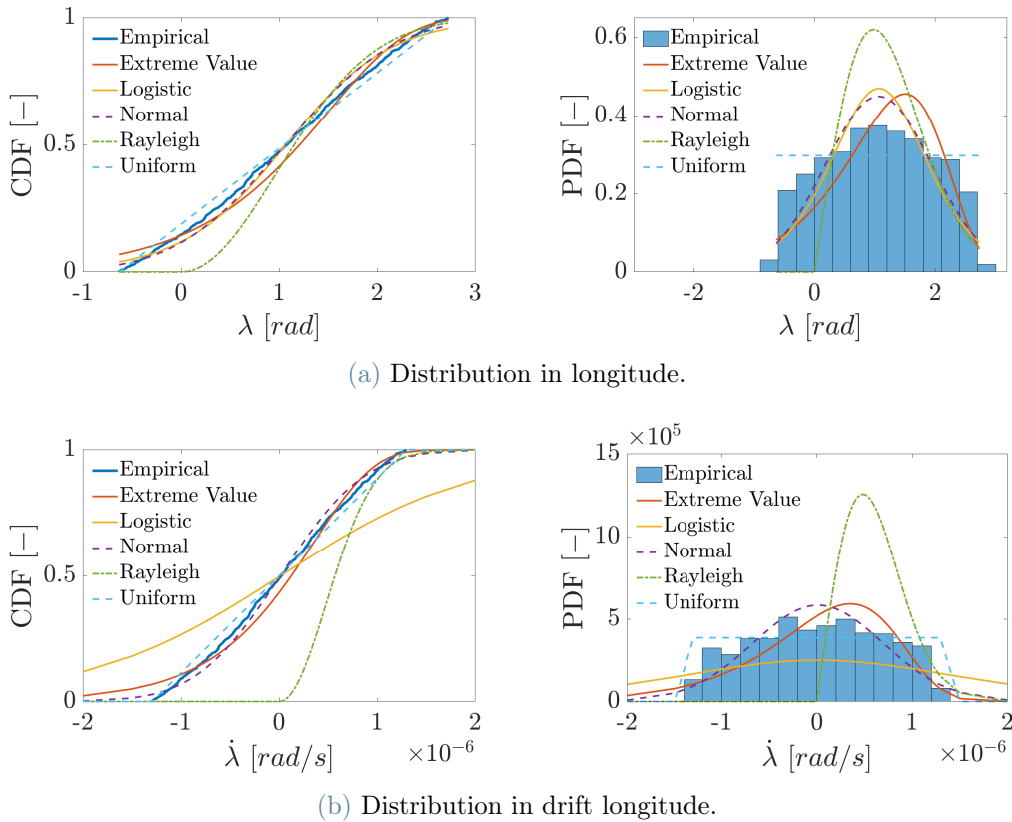
Figure 3.11: Comparison between standard distribution functions and real fragments distribution.

Again, as for the fitting at T_b, a graphical comparison of initial density distribution is provided between the binning and 2-D PDF methods. Figure 3.14 shows that the bivariate normal distribution is able to precisely approximate the distribution of fragments.

Unlike previous methods, Figure 3.12 and Figure 3.13 show that this approach is almost independent to the specific run the NASA Breakup Model and to the selected grid spacing . Therefore, this approach will be adopted for the following analysis.
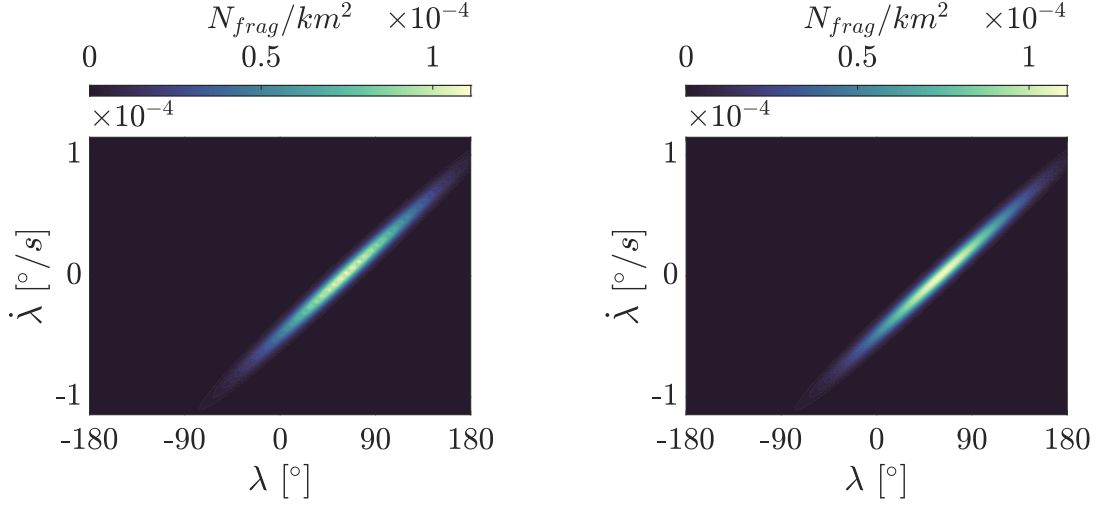
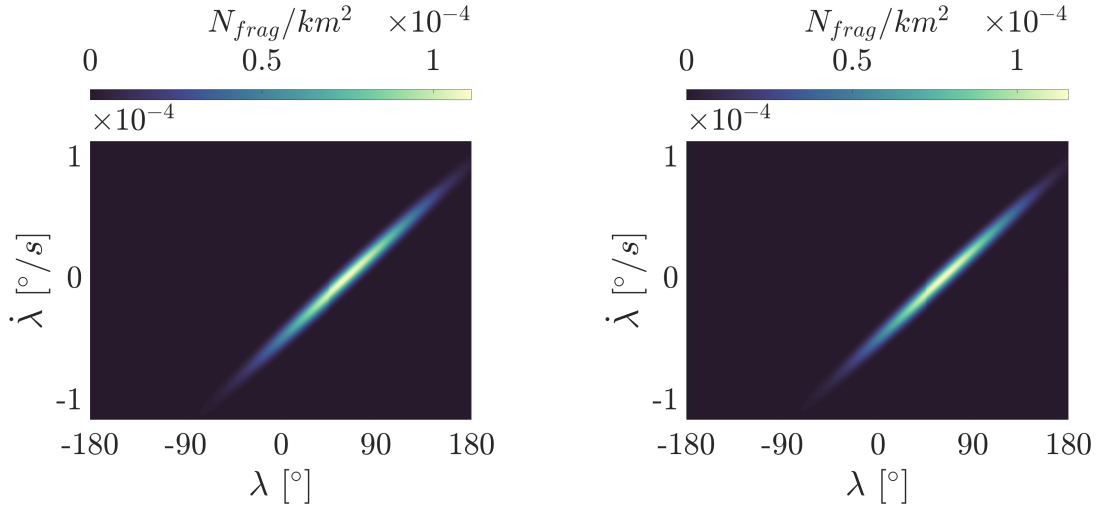(a) Position fitting with 2-D PDF method. Grid made by 4500 cells.

(b) Position fitting with 2-D PDF method. Grid made by 18000 cells.
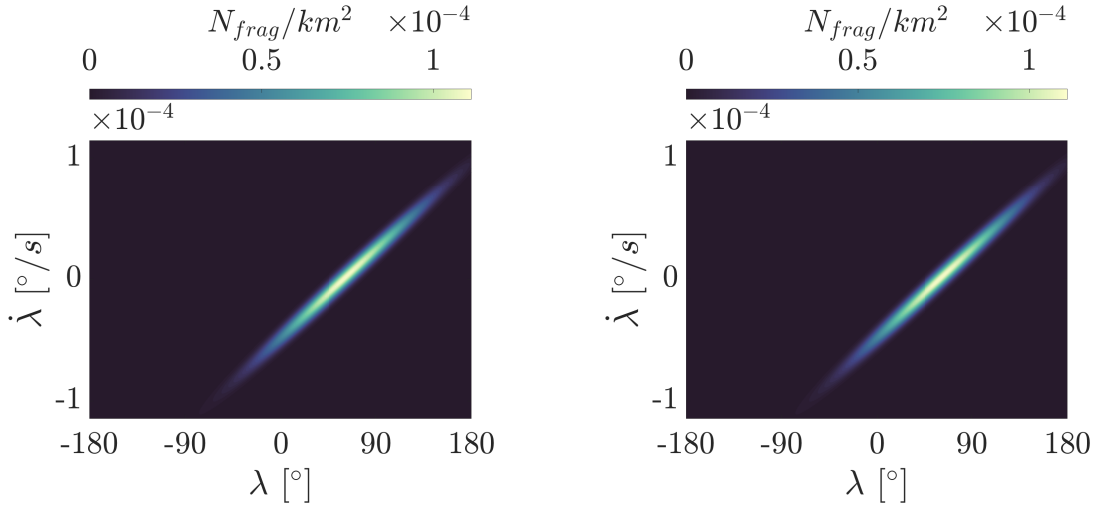
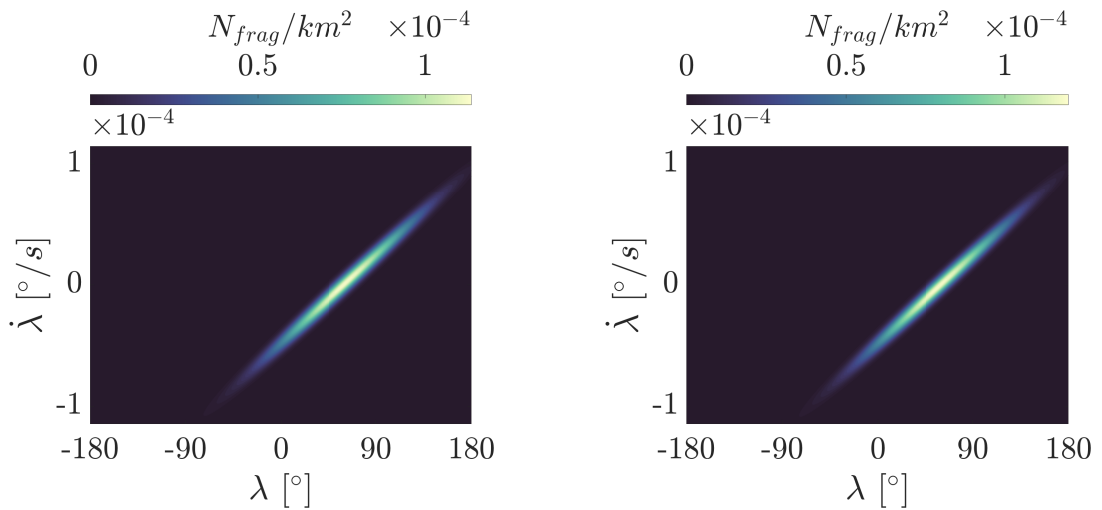(c) Position fitting with 2-D PDF method. Grid made by 72000 cells.

(d) Position fitting with 2-D PDF method. Grid made by 216000 cells.

Figure 3.12: Applications of 2-D Probability Distribution Function method. Grid comparison simulating a catastrophic collision of a rocket body at $\lambda_0 = 60°$ with $\tilde{E}_p = 77.2 J/g$.

(a) Position fitting with 2-D PDF method. Fist run of NASA SBM.
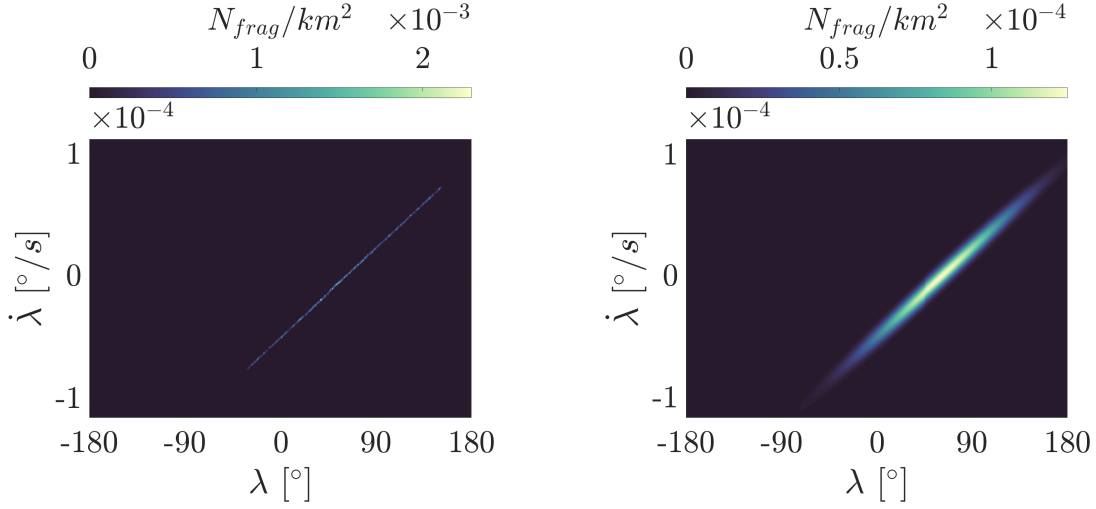

(b) Position fitting with 2-D PDF method. Second run of NASA SBM.

(c) Position fitting with 2-D PDF method. Third run of NASA SBM.

(d) Position fitting with 2-D PDF method. Fourth run of NASA SBM.

Figure 3.13: Applications of 2-D PDF method. Comparison of different runs of NASA SBM simulating a catastrophic collision of a rocket body at $\lambda_0 = 60°$ with $\tilde{E}_p = 77.2 J/g$.
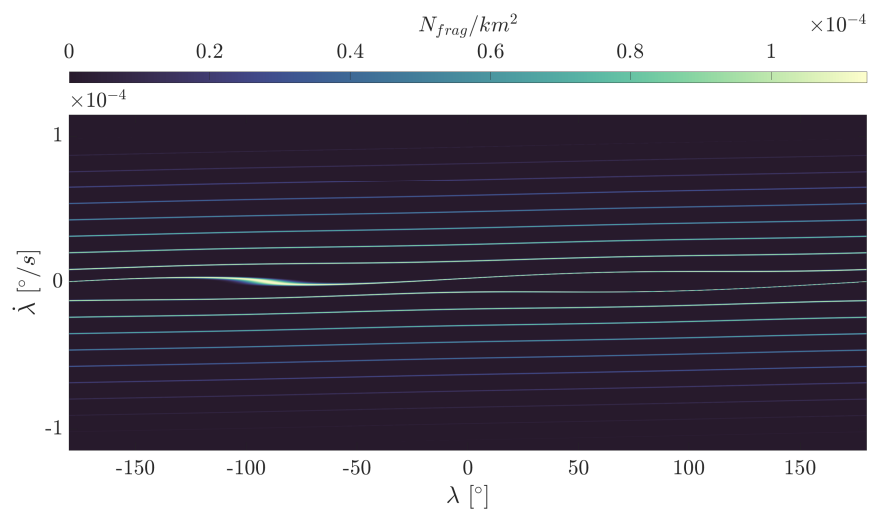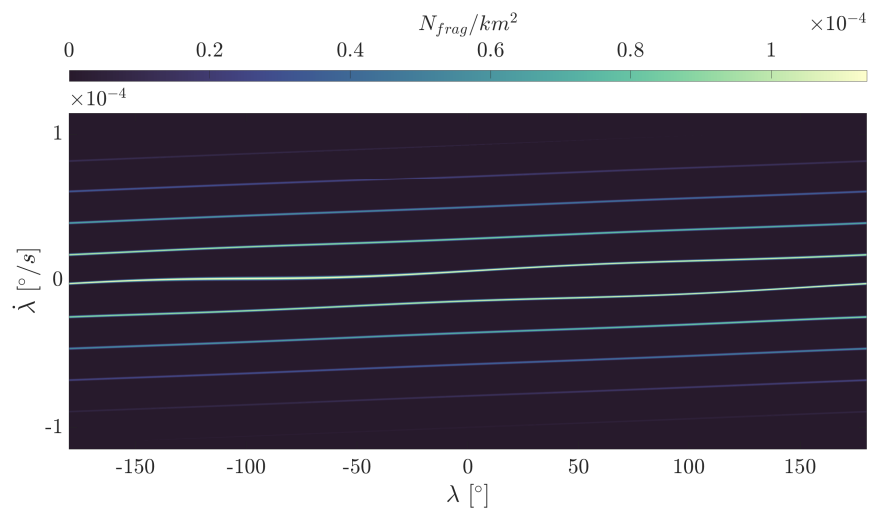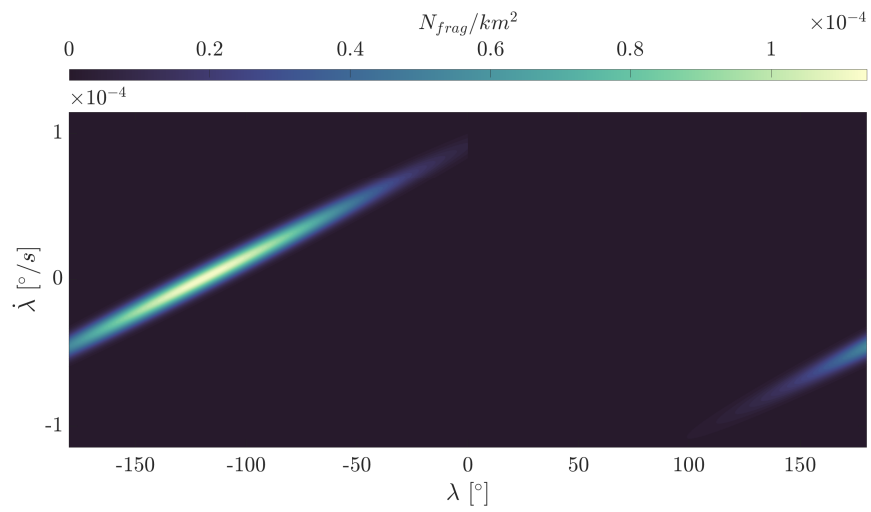
(a) Position fitting with binning method at $T_b/4$. Grid made by 72000 cells.

(b) Position fitting with bi-variate normal distribution at $T_b/4$. Grid made by 72000 cells.
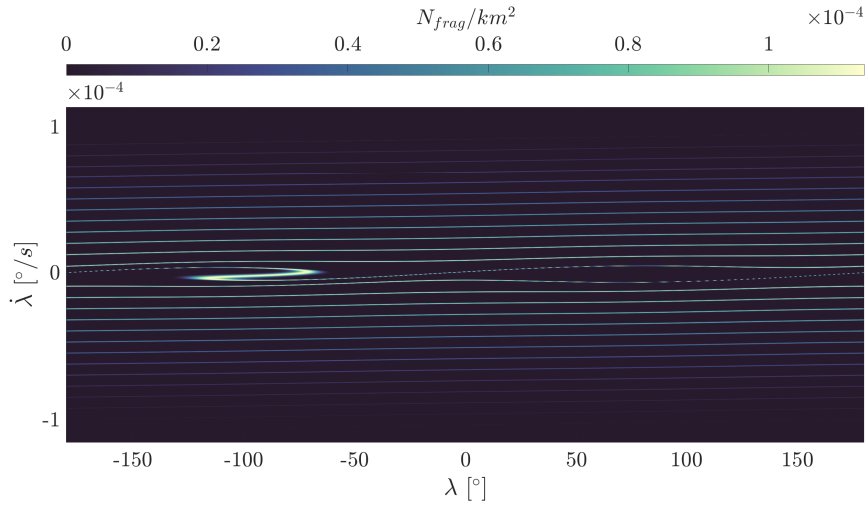
Figure 3.14: Comparison between 2-D PDF and binning methods at $T_b/4$. Simulation of a catastrophic collision of a rocket body at $\lambda_0 = 60°$ with $\tilde{E}_p = 77.2 J/g$.
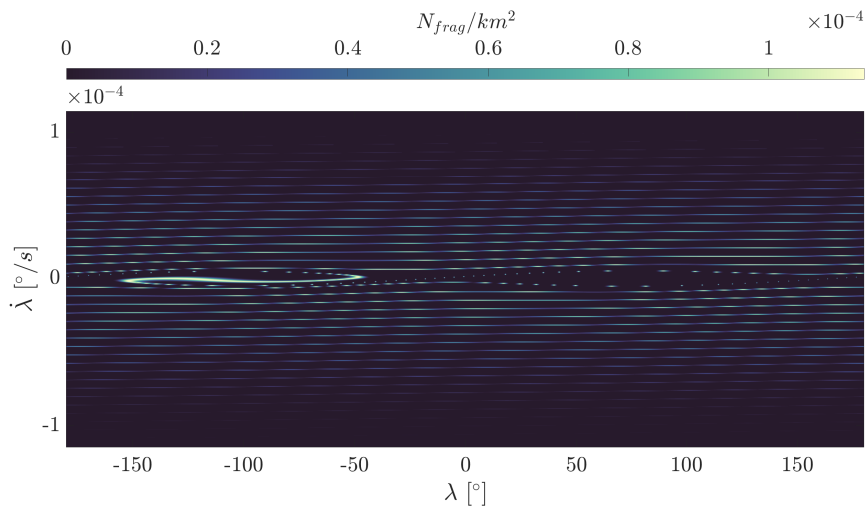
3.5. Application of cloud propagation

This section describe the application of the developed model to a test case. In the following simulation, position fitting is performed through a bi-variate normal distribution and a regular grid in λ and $\dot{\lambda}$ with $\Delta\lambda = 0.36°$ and $\Delta\dot{\lambda} = 5.7 \cdot 10^{-7} °/s$ (corresponding to 400000 cells) is adopted to predict debris distribution in the whole phase space. In particular, a catastrophic collision of a rocket body at $\lambda_0 = -120°$ with $\tilde{E}_p = 77.2 J/g$ is simulated with the NASA breakup model.

Figure 3.15 shows the evolution of the fragments density over time. The debris distribution tends to spread over the entire domain and to be attracted by the closest gravity well (L2). Moreover, it is important to notice that the selected initial condition prevents fragments from being captured from equilibrium point L1, generating a debris-free orbital region. This behaviour can be explained by observing Figure 2.4. At fragmentation epoch, debris share the same longitudinal position (equal to λ_0), meaning that librating fragments will be constrained to move around the gravitational well closest to the fragmentation location. This implies that derelict objects cannot be captured by the other gravitational well and, thus, that the phase space region close to this equilibrium point ($E < 0$) will be characterised by null fragment density.

(a) Fragments distribution at $T_b/4$.

(b) Fragments distribution after 6 months.

(c) Fragments distribution after 1 year.

54 **3| Cloud propagation**

(d) Fragments distribution after 18 months.

(e) Fragments distribution after 2 years.

Figure 3.15: Application of analytical cloud propagation.

By analysing the cloud evolution in the entire domain, however, a huge limit of the backward propagation has also arisen: a very dense regular grid is required to grant an accurate picture of the debris distribution. Indeed, as demonstrated by Figure 3.16, the adoption of few sampling points (in this case corresponding to 18000 cells) will lead to an ambiguous estimation of the fragment density. To overcome this issue, future works will aim to implement a method able to provide an approximation of the density around the characteristics [12].
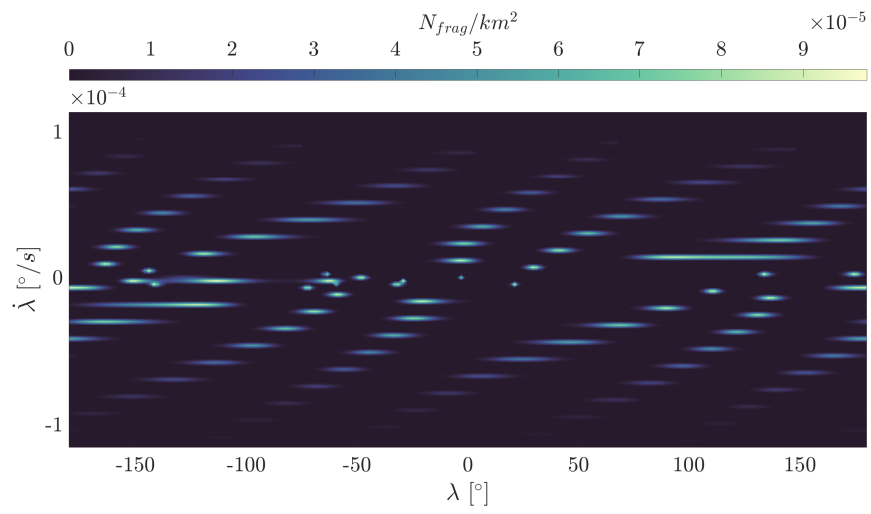
Figure 3.16: Cloud propagation with a coarse grid. Density distribution 2 years after fragmentation event.

4 | Validation process and collision probability

This chapter is devoted to the validation of the model developed in Chapter 3. The model is applied to study the probability of collision of a fictitious fragmentation in GEO.

This chapter is divided into two main parts. Section 4.1 is devoted to the description of the validation process. While, in Section 4.2, cloud propagation is exploited to compute the collision probability simulating a fragmentation in the geosynchronous region and applying the kinetic gas theory.

4.1. Validation process

In order to validate the backward propagation and, thus, the analytical cloud propagator, a procedure based on the forward piece-wise propagation of the debris is implemented. After simulating a fragmentation and fitting the debris dispersion with a bi-variate normal distribution, a random sampling of the initial fragment density is performed by exploiting the build-in MATLAB function *mvnrnd*. This process generates initial conditions of thousands of fictitious debris, which are propagated individually forward in time. Then, at each time of interest, a binning method is adopted to compute the density distribution. In the end, cloud propagation is validated by simulating several fragmentation events and performing a graphical comparison between results provided by the cloud propagator and ones derived with the sampling process.

As example, a catastrophic collision of a rocket body on a perfect geosynchronous orbit at $\lambda_0 = 60°$ with $\tilde{E}_p = 77.2 J/g$ is simulated and results obtained with the two aforementioned methods are plotted in Figure 4.1. Latter are retrieved by applying a regular grid with $\Delta\lambda = 0.36°$ and $\Delta\dot{\lambda} = 5.7 \cdot 10^{-7} °/s$ (corresponding to 400000 cells) and generating 20000 fictitious fragments. Note that the central part of each plot illustrates density distribution retrieved applying the cloud propagator, while side parts present the results of the sampling approach.
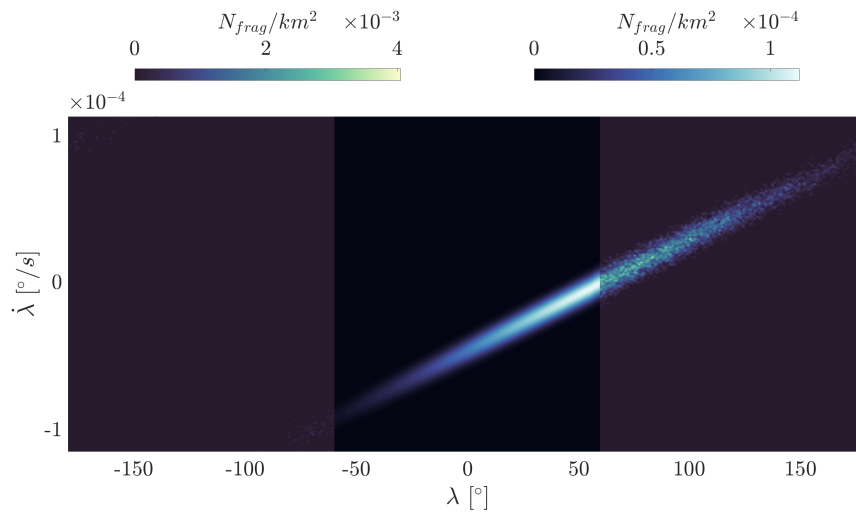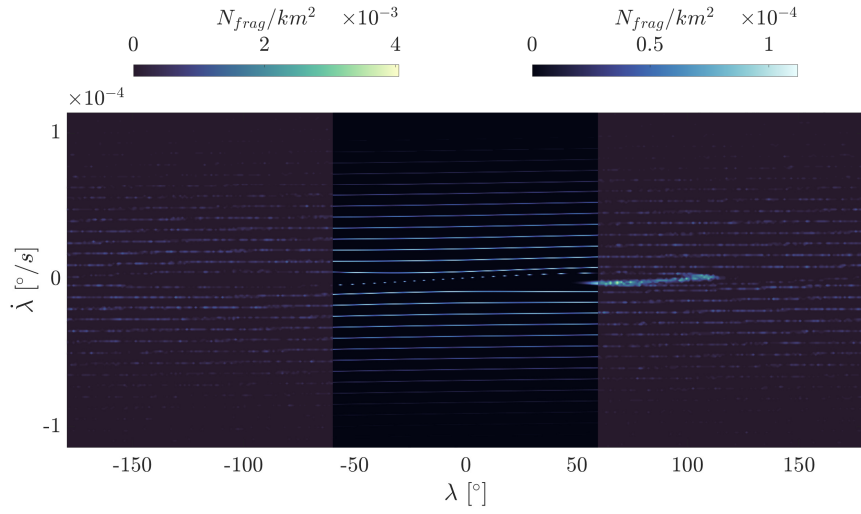
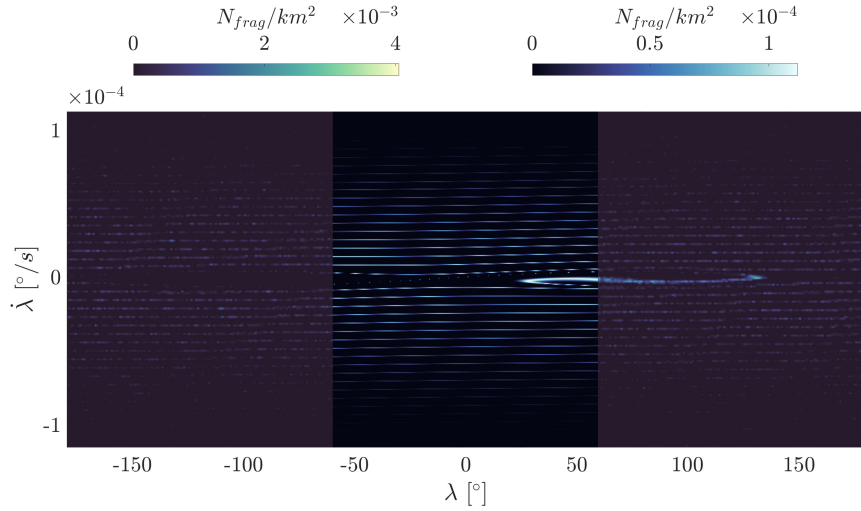(a) Fragments distribution at $T_b/2$.
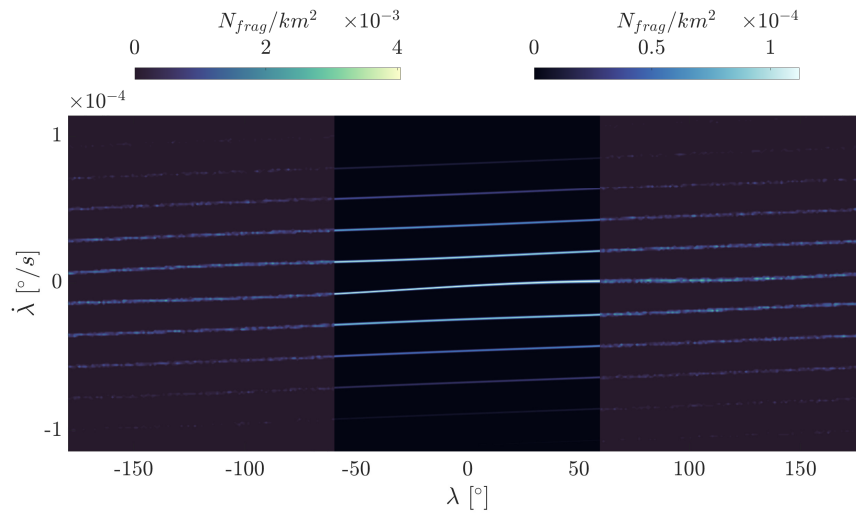
(b) Fragments distribution after 6 months.
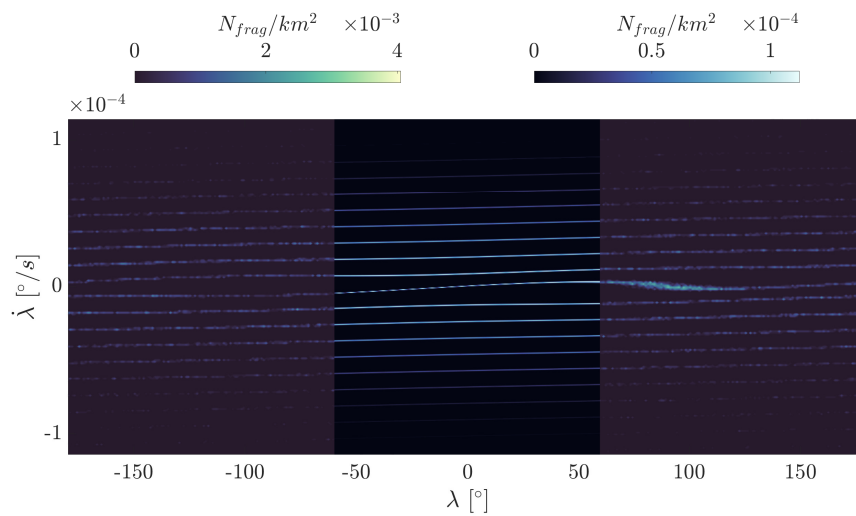
(c) Fragments distribution after 1 year.

(d) Fragments distribution after 18 months.

(e) Fragments distribution after 2 years.

Figure 4.1: Comparison between cloud propagation and sampling strategy.

Observing Figure 3.4 , it is possible to notice that both approaches predict the same behaviour of the cloud and forecast peaks of density in correspondence of the same region of the phase space. For example, Figure 4.1b shows that, simulating a breakup close on a perfect geosynchronous orbit, both methods predicts the shrink of the debris density with the rise of the distance from a_{GEO}. Moreover Figure 4.1d and Figure 4.1e illustrate that both methods forecast an accumulation of fragments close to L1 equilibrium point as a consequence of a breakup close to the gravitational well (L1). However, it is important to observe that absolute value of debris density differ significantly between methods. But, this fact is attributable to the number of sampled fictitious fragments and to the selection of the grid used for the binning method. Indeed, as seen in Section 3.4.1, the reduction

of bin dimensions can cause a wide increase in the local density estimation (Figure 3.4).

Therefore, the analytical cloud propagator results to be a fast and reliable tool for the prediction of debris density in geosynchronous region. In contrast to already available deterministic methods, it allows to include fragments of any size without strongly affecting the computational time and to provide debris density in any region of the phase space without requiring a binning method.

4.2.   Collision probability

The main advantage of the analytical cloud propagation consists in providing a more direct connection with the statistical nature of the problem, in particular for what concerns the computation of the collision probability for a spacecraft crossing a debris cloud. Following McKnight's approach [31], the collision probability P_c for a target crossing a debris cloud can be computed exploiting the analogy with the kinetic gas theory:

$$P_c = 1 - e^{-\rho \cdot v_{rel} \cdot A_c \cdot \hat{T}} \tag{4.1}$$

where ρ is the spatial density, v_{rel} the relative collision velocity, A_c the collision cross-sectional area and $\hat{T}$ the time at risk.

4.2.1.   Spatial density

In this work, spatial density is retrieved by simulating a fragmentation event and applying the analytical cloud propagation. Adopting this strategy, debris density can be computed only at discrete instants of time and, thus, selection of the time span used for the propagation will be crucial for the evaluation of the collision probability. Considering that fragments close to GEO protected region exhibit periods between 80 days and 2000 days, it is recommended to adopt a time step close to 5 days. On the one hand, higher time steps could lead to the undersampling of debris density, causing a misunderstanding of the fragment cloud evolution and, consequentially, a wrong estimation of the collision probability. On the other hand, lower time steps would require more density evaluations and, thus, would increase significantly the computational effort needed for the simulation.

To apply the kinetic theory of gases, the phase space density should be converted into a spatial one. Recalling that uncontrolled GEO objects tend naturally to arrange on orbits with inclination between $-15°$ and $15°$ [6], the latitudinal dispersion of the debris can be approximated as a uniform distribution:

$$p(\phi) = \begin{cases} \frac{6}{\pi} & \text{for } |\phi| \leq 15° \\ 0 & \text{for } |\phi| > 15° \end{cases} \tag{4.2}$$

and, therefore, spatial density can be computed as [11]:

$$\rho = \frac{n(\lambda, \dot{\lambda}, t) \cdot p(\phi) d\dot{\lambda} \, d\lambda \, d\phi}{\Delta V} = \frac{n(\lambda, \dot{\lambda}, t) p(\phi) d\dot{\lambda} \, d\lambda \, d\phi}{da \cdot a_c d\lambda \cdot a_c d\phi} = \frac{9\Omega_\oplus}{\pi a_c^3} n(\lambda, \dot{\lambda}, t) \tag{4.3}$$

4.2.2. Relative collision velocity

The average relative velocity used for the evaluation of the probability of collision is computed as function of the orbital velocity v_{GEO} of the operating GEO satellite and the mutual inclination Δi between the projectile and target mass[31]:

$$v_{rel} = \sqrt{2v_{GEO}^2(1 - \cos \Delta i)} \tag{4.4}$$

The operational satellite at risk is assumed on a perfect geostationary orbit and, thus, mutual inclination can be replaced by the average inclination of the derelict population. As suggested by McKnight [31], an average inclination of 10° can be assumed to avoid underestimating the collision probability, resulting in a relative velocity of about 536 m/s.

4.2.3. Collision cross-section and time at risk

The collision cross-section is a function of both impacting and target physical cross-sections:

$$A_c = \sqrt{A_p^2 + A_t^2} \tag{4.5}$$

In this thesis, a $100 \, m^2$ value is used as a nominal value for A_c since the largest few objects in GEO are around $30 - 50 \, m^2$.

In order to assess the annual probability of collision, the time at risk for a station-kept satellite is set equal to one year.

4.2.4. Collision probability calculation

After introducing the elements required for the computation of the collision probability, several simulations are performed to check the consistency between the obtained collision risk and the dynamics governing the geosynchronous region.

All simulations have been carried out applying a regular grid with $\Delta\lambda = 0.36°$ and $\Delta\dot{\lambda} = 5.7 \cdot 10^{-7} °/s$ (corresponding to 400000 cells), using a time step of 5 days and considering a catastrophic collision of a rocket body on a perfect geosynchronous orbit with $\tilde{E}_p = 77.2 J/g$.

First test simulates a fragmentation event at $\lambda_0 = -110°$. Figure 4.2 shows that a fragmentation close to (L2) gravitational well produces a peak in collision probability in proximity of the closest stable equilibrium point. Moreover, selected initial condition prevents fragments from being captured from equilibrium point (L1), generating a debris-free orbital region, corresponding to a null collision probability region. This behaviour can be justified by the fact that liberating objects are captured by the gravitational well closest to λ_0 and that drifting objects have a too high energy level to access the L1 librating region.

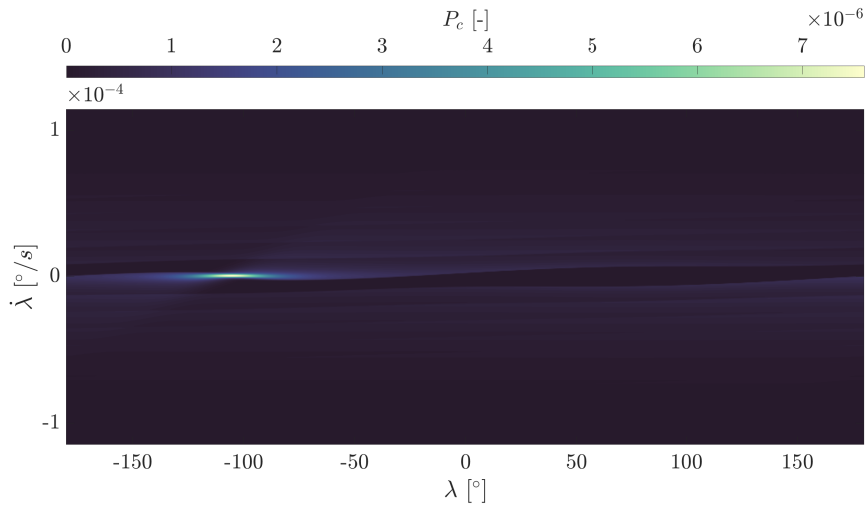
Figure 4.2: Annual collision probability in phase space $(\lambda, \dot{\lambda})$. Fragmentation simulated at $\lambda_0 = -110°$.

Regarding the second simulation, location of fragmentation is set equal to $\lambda_0 = 60°$. Figure 4.3 shows that librating objects are energetically bounded by (L1) gravitational well and, thus, produce a rise of the collision probability in correspondence of the afore-mentioned equilibrium point. Analogously to the previous case, the region close to L2 equilibrium point is characterised by a null fragment density, while drifting objects produce a lower debris density in the rest of the phase space.
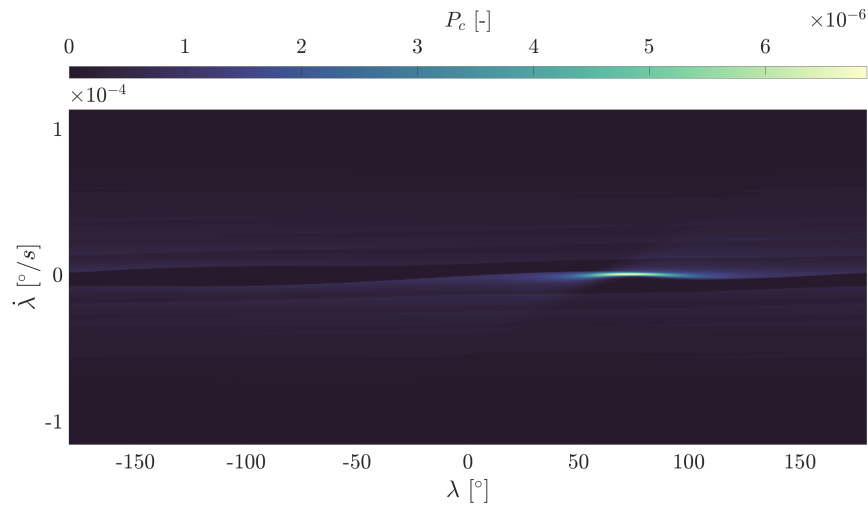
Figure 4.3: Annual collision probability in phase space $(\lambda, \dot{\lambda})$. Fragmentation simulated at $\lambda_0 = 60°$.

In the end, third simulation is carried out by selecting a fragmentation location in correspondence of the unstable equilibrium point (L3). Observing Figure 4.4, it is possible to notice that a fragmentation at $\lambda_0 = \lambda_{2,2}$ generates only drifting objects and, thus, that librating regions of the phase space will be characterise by a null collision risk.
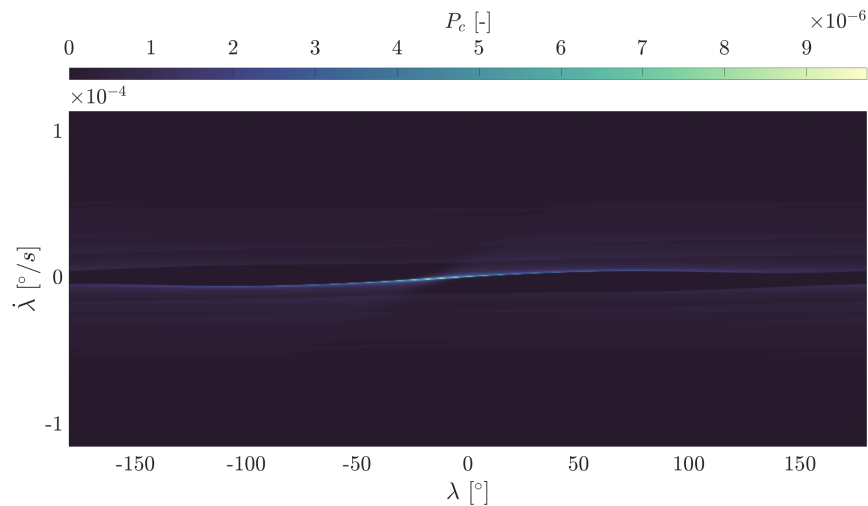
Figure 4.4: Annual collision probability in phase space $(\lambda, \dot{\lambda})$. Fragmentation simulated at $\lambda_0 = -15°$.

It is possible to conclude that, thanks to its accuracy and its limited computational time, the proposed method can be applied to efficiently analyse the impact of different breakups on various target spacecrafts and, thus, to create influence matrixes. Moreover,

the developed approach results to be a fast and precise tool for the generation of collision probability maps that could be exploited for the definition of a space debris index for the geostationary region.

5 | Conclusions and future developments

This Chapter provides a short summary of the main findings of the thesis together with a discussion on its limitations and on possible future improvement of the model.

5.1. Summary of the thesis

Current studies on space debris evolution in the geosynchronous region are based on deterministic methods and usually refer only to the population of objects larger than 1 meter. Indeed, large objects are the most dangerous in case of collision: they are able to destroy completely a satellite and to create large debris clouds. However, also small debris fragments can represent a relevant hazard to operational satellites, but their contribution to the collision risk is often discarded due to the limited computational capabilities. Indeed, the number of small fragments is so large that the traditional propagation of all objects is not feasible. Therefore, this work proposes a probabilistic approach based on the continuity equation, enabling the inclusion of small fragments in debris modelling. In particular, the developed method considers debris population as a fluid with continuous properties, whose density changes under the effect of $J_{2,2}$ gravitational perturbation.

Once the information on the position of the fragments is converted into a continuous density function and, thus, the initial density profile is defined, time evolution of debris density close to the GEO protected region is obtained by solving analytically the continuity equation with the assumption of quasi-equatorial and quasi-circular orbits. The explicit expression for the density allows the method to provide a very fast estimation of longitude slots most susceptible to rising debris fluxes and of the resulting collision probability for an operative spacecraft in that region. Indeed, the main advantage of this approach consist in providing a more direct connection with the statistical nature of the problem, in particular for what concerns the computation of the collision probability for a spacecraft crossing the cloud.

Model formulation: The proposed method is essentially based on the following building blocks:

- a break up model that simulate collisions and explosions, given the energy of the fragmentation event;

- an analytical model to propagate fragments piece-wise until the cloud propagation becomes applicable;

- a fitting method to convert orbital parameters of each single fragment into a continuous density function;

- a fully analytical cloud propagator to analyse time evolution of space debris cloud.

Model validation: The proposed method has been extensively validated comparing results provided by cloud propagator with the one obtained applying a numerical/analytical piece-wise propagator. The results have been compared in terms of the resulting spatial density as it will be used to evaluate the collision probability within the cloud. The proposed method has been tested under different conditions by changing the breakup energy, the kind of breakup event, longitude of the fragmentation event and semi-major axis of the parent orbit.

Method applications: Given the positive outcome of the validation process, the method has been applied to many different scenarios to compute the collision probability for a spacecraft crossing a debris cloud. Analogy with the kinetic theory of gases was used to convert a fragment spatial density into a collision risk. Three possible applications of the method were identified:

- the study of real breakups and the resulting collision probability for a set of GEO satellites falling inside the debris population;

- the study of the influence among two different targets, assessing how a fragmentation of one object is able to affect the collision probability of another one;

- the study of collision maps, evaluating their exposure to fragmentations considering different values of longitude and semi-major axis.

In all three cases the analytical method offers an important reduction in the computational time and gives an interesting insight on the contribution of small fragments to the collision risk.

Main findings: The main results of the work can be summarised in the following list:

- an analytical method for the description of the evolution of space debris clouds

generated by breakups has been developed; the method is based on the continuity equation and allows to obtain a fully analytical propagation of a debris cloud under the $J_{2,2}$ effect;

- the method has been extended to assess also the collision probability for a spacecraft crossing the fragment cloud;

- the method has been applied to model many different scenarios of collisions proving the flexibility of the new approach and its ability of enabling new analyses on the collision risk due to small fragments.

5.2. Limitations of this work

The research here presented has clearly shown the two main advantages of the proposed method. Firstly, the analysis in terms of debris spatial density offers not only a reduction in the computational effort, but especially a strong connection with the statistical nature of the problem providing a simple tool for the computation of the resulting collision probability. Secondly, the application of the continuity equation allows to provide an analytical solution to the problem enhancing the degree of flexibility on the modelling. Nevertheless, also some limitations of the method have been identified and are here discussed.

Position fitting: The proposed method implies the need of propagating individually fragments until the cloud propagation becomes applicable. This procedure is performed through the analytical propagator, however, in case of large debris clouds, this step could be computationally expensive.

Perturbation modelling: The current version of the method includes only the $J_{2,2}$ effect to allow the derivation of a fully analytical approach. As shown previously, this simplified dynamical model limits the applicability of the method to objects orbiting on quasi-circular and quasi-equatorial orbits with $|a - a_{GEO}| < 500$km.

Method of characteristics: Actually, performance of the developed approach is limited by the method of characteristics adopted to solve the continuity equation. Indeed, fragment density cannot be estimated outside the characteristic curves and, thus, many backward propagations are required to evaluate density evolution over wide regions of the $(\lambda, \dot{\lambda})$ phase space.

Single events versus background population: The study of the collision probability was developed considering only the effect of the new fragments produced by a specific fragmentation event without considering the background population. This means that all

the results involving the collision probability should be read in a relative way with respect to a baseline scenario without the studied breakup.

5.3.   Future works

The analysis of the limitations of the model has suggested some possible elements for the development of the work. Firstly, future works could focus on the removal of the piece-wise propagation for definition of initial density. Secondly, a huge improvement of the model could be achieved with the implementation of a method able to provide an approximation of the density around the characteristics. Thirdly, a careful evaluation of the possibility of including additional perturbations in the model could be performed. Fourthly, an analytical estimation of the relative velocity between the spacecraft and the cloud could be developed. In the end, this method could be used as foundation for the definition of a geostationary debris index.

Bibliography

[1] P. V. Anderson and H. Schaub. Local orbital debris flux study in the geostationary ring. *Advances in Space Research*, 51:2195–2206, 2013.

[2] P. V. Anderson and H. Schaub. Local debris congestion in the geosynchronous environment with population augmentation. *Acta Astronautica*, 94:619–628, 2014.

[3] P. V. Anderson and H. Schaub. Longitude-dependent effects of fragmentation events in the geosynchronous orbit regime. *Acta Astronautica*, 105:285–297, 2014.

[4] P. V. Anderson and H. Schaub. *Characterising Longitude-Dependent Orbital Debris Congestion in the Geosynchronous Orbit Regime*. PhD thesis, University of Colorado at Boulder, https://ui.adsabs.harvard.edu/abs/2015PhDT........48A, Jan. 2015.

[5] P. V. Anderson and H. Schaub. Methodology for characterizing high-risk orbital debris in the geosynchronous orbit regime. *Advances in Space Research*, 57:604–619, 2016.

[6] P. V. Anderson, H. Schaub, D. S. McKnight, and F. Di Pentino. Merging analytic and empirical geo debris synchronization dynamics. *Advances in Space Research*, 58: 914–923, 2016.

[7] L. Anselmo and C. Pardini. Ranking upper stages in low earth orbit for active removal. *Acta Astronautica*, 122:19–27, 2016. ISSN 0094-5765. doi: https://doi.org/10.1016/j.actaastro.2016.01.019. URL https://www.sciencedirect.com/science/article/pii/S0094576516000291.

[8] J. Ashenberg. Formulas for the phase characteristics in the problem of low-earth-orbital debris. *Journal of Spacecraft and Rockets*, 31(6):1044–1049, 1994. doi: 10.2514/3.26556. URL https://doi.org/10.2514/3.26556.

[9] D. Casanova, A. Petit, and A. Lemaitre. Long-term evolution of space debris under the j_2 effect, the solar radiation pressure and the solar and lunar perturbations. *Celestial Mechanics and Dynamical Astronomy*, 123:223–238, 2015. ISSN 1572-9478.

doi: https://doi.org/10.1007/s10569-015-9644-1. URL `https://link.springer.com/article/10.1007/s10569-015-9644-1`.

[10] H. D. Curtis. *Orbital Mechanics for Engineering Students*. Elsevier, 3 edition, 2013. ISBN 9780080977485.

[11] T. Flohrer and F. Schmitz, editors. *Algorithms For The Computation Of Debris Risk*, volume 7, 2017. ESA Space Debris Office.

[12] S. Frey. *Evolution and hazard analysis of orbital fragmentation continua*. PhD thesis, Politecnico di Milano, http://hdl.handle.net/10589/165144, July 2020.

[13] R. Frick and T. Garber. Perturbations of a synchronous satellite due to triaxiality of the earth. *Journal of the Aerospace Sciences*, 29(9):1105–1111, 1962. doi: 10.2514/8.9705. URL `https://doi.org/10.2514/8.9705`.

[14] S. Howard, J. Murray-Krezan, P. Dao, and D. Surka. GEO Collisional Risk Assessment Based on Analysis of NASA-WISE Data and Modeling. In *Advanced Maui Optical and Space Surveillance Technologies Conference*, page 35, Jan. 2015.

[15] IADC, editor. *Space debris. Assessment Report for 2011*, 2013. European Space Agency.

[16] C. Kebschull, P. Scheidemann, S. Hesselbach, J. Radtke, V. Braun, H. Krag, and E. Stoll. Simulation of the space debris environment in leo using a simplified approach. *Advances in Space Research*, 59(1):166–180, 2017. ISSN 0273-1177. doi: https://doi.org/10.1016/j.asr.2016.08.005. URL `https://www.sciencedirect.com/science/article/pii/S0273117716304380`.

[17] Kessler, J. Donald, and B. G. Cour-Palais. Collision frequency of artificial satellites: The creation of a debris belt. *Journal of Geophysical Research: Space Physics*, 83 (A6):2637–2646, 1978. doi: https://doi.org/10.1029/JA083iA06p02637. URL `https://agupubs.onlinelibrary.wiley.com/doi/abs/10.1029/JA083iA06p02637`.

[18] H. Klinkrad. *Space Debris: Models and Risk Analysis*. Springer Praxis Books. Springer Berlin Heidelberg, 2006. ISBN 9783540376743. URL `https://books.google.it/books?id=LMezvrqV3fUC`.

[19] P. Krisko, S. Flegel, M. Matney, D. Jarkey, and V. Braun. Ordem 3.0 and master-2009 modeled debris population comparison. *Acta Astronautica*, 113:204–211, 2015. ISSN 0094-5765. doi: https://doi.org/10.1016/j.actaastro.2015.03.024. URL `https://www.sciencedirect.com/science/article/pii/S0094576515001241`.

[20] F. Letizia and C. Colombo. Space debris cloud evolution in low earth orbit. In *64th International Astronautical Congress*, Beijing, China, 2013. International Astronautical Federation. URL `https://eprints.soton.ac.uk/367222/`.

[21] F. Letizia and C. Colombo. *Space debris cloud evolution in Low Earth Orbit*. PhD thesis, University of Southampton, http://eprints.soton.ac.uk/id/eprint/387121, Nov. 2015.

[22] F. Letizia, C. Colombo, and H. Lewis. Continuity equation approach for the analysis of the collision risk due to space debris clouds generated by a fragmentation event. In *65th International Astronautical Congress*, Toronto, Canada, 2014. International Astronautical Federation.

[23] F. Letizia, C. Colombo, and H. Lewis. 2d continuity equation method for space debris cloud collision analysis. In *25th AAS/AIAA Space Flight Mechanics Meeting*, pages 1473–1492, Williamsburg, VA, USA, 2015. ISBN 978-0-87703-623-4.

[24] F. Letizia, C. Colombo, and H. Lewis. Analytical model for the propagation of small-debris-object clouds after fragmentations. *Journal of Guidance, Control, and Dynamics*, 38(8):1478–1491, 2015. doi: 10.2514/1.G000695. URL `https://doi.org/10.2514/1.G000695`.

[25] F. Letizia, C. Colombo, and H. Lewis. Multidimensional extension of the continuity equation method for debris clouds evolution. *Advances in Space Research*, 57(8):1624–1640, 2016. ISSN 0273-1177. doi: https://doi.org/10.1016/j.asr.2015.11.035. URL `https://www.sciencedirect.com/science/article/pii/S0273117715008327`. Advances in Asteroid and Space Debris Science and Technology - Part 2.

[26] F. Letizia, C. Colombo, H. G. Lewis, and H. Krag. Assessment of breakup severity on operational satellites. *Advances in Space Research*, 58(7):1255–1274, 2016. ISSN 0273-1177. doi: https://doi.org/10.1016/j.asr.2016.05.036. URL `https://www.sciencedirect.com/science/article/pii/S0273117716302393`.

[27] H. Li. *Geostationary Satellites Collocation*. Springer, 2014. ISBN 9783642407987.

[28] J.-C. Liou. Collision activities in the future orbital debris environment. *Advances in Space Research*, 38(9):2102–2106, 2006. ISSN 0273-1177. doi: https://doi.org/10.1016/j.asr.2005.06.021. URL `https://www.sciencedirect.com/science/article/pii/S0273117705008057`. Small Bodies in the Solar System; Space Debris.

[29] C. R. McInnes. A continuum model for the orbit evolution of self-propelled 'smart dust' swarms. *Celestial Mechanics and Dynamical Astronomy*, 126:501–517, 2016. doi: https://doi.org/10.1007/s10569-016-9707-y.

[30] D. McKnight. A phased approach to collision hazard analysis. *Advances in Space Research*, 10(3):385–388, 1990. ISSN 0273-1177. doi: https://doi.org/10.1016/0273-1177(90)90374-9. URL https://www.sciencedirect.com/science/article/pii/0273117790903749.

[31] D. S. McKnight and F. R. Di Pentino. New insights on the orbital debris collision hazard at geo. *Acta Astronautica*, 85:73–82, 2013. ISSN 0094-5765. doi: https://doi.org/10.1016/j.actaastro.2012.12.006. URL https://www.sciencedirect.com/science/article/pii/S0094576512004869.

[32] A. Nazarenko. Prediction of the space debris spatial distribution on the basis of the evolution equations. *Acta Astronautica*, 100:47–56, 2014. ISSN 0094-5765. doi: https://doi.org/10.1016/j.actaastro.2014.02.023. URL https://www.sciencedirect.com/science/article/pii/S0094576514000800.

[33] K. Ochs. A comprehensive analytical solution of the nonlinear pendulum. *European Journal of Physics*, 32(2):479–490, feb 2011. doi: 10.1088/0143-0807/32/2/019. URL https://doi.org/10.1088/0143-0807/32/2/019.

[34] E. S. D. Office, editor. *ESA'S ANNUAL SPACE ENVIRONMENT REPORT*, 2021. European Space Agency. URL https://www.sdo.esoc.esa.int/environment_report/Space_Environment_Report_latest.pdf.

[35] A. Rossi, H. Lewis, A. White, L. Anselmo, C. Pardini, H. Krag, and B. Bastida Virgili. Analysis of the consequences of fragmentations in low and geostationary orbits. *Advances in Space Research*, 57(8):1652–1663, 2016. ISSN 0273-1177. doi: https://doi.org/10.1016/j.asr.2015.05.035. URL https://www.sciencedirect.com/science/article/pii/S0273117715003750. Advances in Asteroid and Space Debris Science and Technology - Part 2.

[36] T. Soong. *Fundamentals of probability and statistics for engineers*. John Wiley & Sons Inc, 01 2004. ISBN 9780470868157.

[37] S. Valk, A. Lemaître, and L. Anselmo. Analytical and semi-analytical investigations of geosynchronous space debris with high area-to-mass ratios. *Advances in Space Research*, 41(7):1077–1090, 2008. ISSN 0273-1177. doi: https://doi.org/10.1016/j.asr.2007.10.025. URL https://www.sciencedirect.com/science/article/pii/S0273117707010435.

[38] S. Valk, A. Lemaitre, and F. Deleflie. Semi-analytical theory of mean orbital motion for geosynchronous space debris under gravitational influence. *Advances in Space Research*, 43:1070–1082, 2009.

[39] D. A. Vallado. *Fundamentals of Astrodynamics and Applications*. Microcosm, 4 edition, 2013. ISBN 1881883191.

[40] C.-H. Zee. *Theory Of Geostationary Satellites*. Springer, 1 edition, 1989. ISBN 9789401076623.